Stability and Uncertainty of Ice-Sheet Crystal Fabrics

Michael John Hay

A dissertation
submitted in partial fulfillment of the
requirements for the degree of

Doctor of Philosophy

University of Washington

2017

Reading Committee:

Edwin Waddington, Chair

Howard Conway

Gerard Roe

Randall J. LeVeque

Program Authorized to Offer Degree:
Department of Earth and Space Sciences

University of Washington

Abstract

Stability and Uncertainty of Ice-Sheet Crystal Fabrics

Michael John Hay

Chair of the Supervisory Committee:
Professor Edwin Waddington
Department of Earth and Space Sciences

Ice crystal orientation fabric has a large effect on polycrystalline ice flow. In this thesis, I explore uncertainty of ice fabric measurements, and the related question of stability of ice crystal fabrics and anisotropic ice flow in ice sheets. I develop new estimates of uncertainty of fabric parameter estimates from thin-section data, and connect this to uncertainty in ice flow characteristics. To reduce this sampling error, I develop a new inverse method to infer fabric parameters from sonic velocity measurements and thin-section samples. I show a number of results concerning the stability of ice crystal fabrics in ice sheets. First, I show that small velocity gradient perturbations can induce large changes in ice fabric, which in turn affects anisotropic ice viscosity significantly. Next, I analyze the development of incipient fabric perturbations in coupled flow. I develop an analytical coupled model of anisotropic ice flow and fabric evolution, and show that the coupled system is unstable in many circumstances under ice-sheet flank flow and divide flow.

TABLE OF CONTENTS

LIST OF FIGURES

DEDICATION

This thesis is dedicated to my dog Eli.

Outside of a dog, a book is a man's best friend. Inside of a dog, it's too dark to read.

- Groucho Marx

ACKNOWLEDGMENTS

This thesis, and my Ph.D. studies have only been possible due to the amazing help and support I have had from people around me. First and foremost, Ed Waddington has been the best advisor any grad student could hope for. His support and insight have been integral to my success.

Thanks also to the rest of my committee. Twit Conway has been a great co-advisor. The work on Beardmore glacier is a highlight of my Ph.D. Gerard Roe has greatly improved this thesis with his critical eye on my work. Also, thanks to Randy LeVeque for serving as my GSR.

My fellow grad students, and my officemates in particular, have been a great source of support, scientific and otherwise. Thanks to Dan Kluskiewicz, Rob Sheerer, Trevor Thomas, Adam Campbell, Max Stevens, Elena Amador, John Christian, Taryn Black, and everyone else.

Thanks also to faculty and postdocs T.J. Fudge, Michelle Koutnik, Al Rasmussen, Clement Miege.

A big thanks to ESS staff. Thanks to Ed Mulligan for computer support, and Noell Bernard for her help advising me.

Lastly, thanks to my partner Nick, my parents, and my brother Tom. You don't choose your family, but I couldn't have chosen a better one.

GLOSSARY

ICE CRYSTAL: A region of ice where the crystallographic structure is sufficiently uniformly oriented.

GRAIN: Synonym for ice crystal.

BASAL PLANE: Crystallographic plane in ice with easy shear.

C-AXIS: Direction orthogonal to the basal plane.

POLYCRYSTAL: A multicrystalline aggregate.

ORIENTATION DISTRIBUTION FUNCTION: Probability distribution of c-axis orientations of a polycrystal.

SECOND-ORDER ORIENTATION TENSOR: Second moment $A_{ij} =< c_i c_j >$ of an ODF.

FABRIC EIGENVALUE: An eigenvalue of A_{ij}.

HOMOGENIZATION SCHEME: A method of reconciling bulk stress and strain of a polycrystal to stress and strain of individual grains.

POLYGONIZATION: Splitting of ice grains due to progressive rotation of subgrains.

DYNAMIC RECRYSTALLIZATION: The nucleation and growth of new grains.

ICE DIVIDE: A point where ice flows from in different directions, similarly to hydrographic divides.

FLANK FLOW: Flow of ice on ice-sheet flanks, away from ice divides. Surface slope provides the driving stress. Movement is mainly due to simple shear, concentrated in the lower layers.

DIVIDE FLOW: Flow of ice near ice divides. Dominated by longitudinal extension.

GAUSSIAN PROCESS: A random function where finite samples of the function follow a multivariate Gaussian distribution.

Chapter 1

INTRODUCTION

1.1 Introduction

Individual ice crystals have an unusual amount of plastic anisotropy, with deformation by shear along the basal plane being around 100 times easier than strain in other orientations (e.g. Duval et al. [28]). Due to this, the aggregate orientations of crystals (the crystal fabric) has a large effect on bulk ice flow in ice sheets. If the orientations are anisotropic, the ice has a bulk anisotropic response to stress. Conversely, ice flow drives development of crystal orientation fabric in ice sheets.

Aside from understanding ice rheology, ice fabric may be useful itself for paleoclimate interpretation. Kennedy et al. [49] found that initial differences in fabric at snow deposition can persist deep into ice sheets. In the NEEM core in Greenland, there is an abrupt change in fabric corresponding to the Holocene transition [60].

Anisotropic ice flow due to anisotropic crystal fabric can itself hinder paleoclimate interpretation by causing stratigraphic disruption, where isochronous layers can become folded or removed. Alley et al. [7] found recumbent z-folds in the GISP2 core associated with "stripes" of anomalously oriented grains. Fudge et al. [32] found evidence of small-scale boudinage about 750m above the bed in the WAIS divide core. These features may be due to anisotropic flow.

This thesis is not primarily focused on the detailed microstructural physics of ice, nor is it directly focused on empirical observations of ice crystal orientation fabrics. Instead, it is focused on answering the question of *what we do not know* about ice fabric and anisotropic ice flow. I explore uncertainties in fabric measurement methods, and also how these uncertainties may be reduced. I examine the effects of velocity-gradient perturbations on ice fabric. In addition, I study perturbations to fabric as part of a coupled system, and show that stratigraphic disturbances could occur due to initial fabric perturbations in coupled ice flow and fabric development.

1.2 Background

In this section, I will give a brief overview of the background material related to this thesis. I first discuss small-scale ice physics. I review homogenization methods to derive continuum approximations to polycrystalline ice, as well as fabric evolution.

1.2.1 Ice crystal deformation, rotation, and growth

A cartoon of an individual ice crystal is shown in Fig. 1.1, with the crystallographic c-axis labeled. An individual ice crystal deforms primarily by dislocation creep in glacial settings [81]. A dislocation is a defect in the crystal lattice. Since the regular atomic structure of the crystal is distorted by the dislocation, there is an associated strain and stress field. For edge dislocations, this takes the form of a dipole, with one pole being compressive and the other tensile. If an external stress is applied to the crystal, this produces a net driving force on the dislocation, which can induce the dislocation to move if sufficient stress is realized. When a dislocation reaches a grain boundary, the crystal is sheared. Dislocations are generated during strain. As grains become highly strained, dislocations begin to interfere, causing deformation to become more difficult. This is known as work-hardening, in common with the metallurgical definition. Dislocations may be removed through the process of recovery, where dislocations move to minimize their free energy. This occurs partly through the annihilation of dislocations of opposite sign, and arrangement of dislocations into subgrain boundaries or to the grain boundaries themselves. The combined effects of dislocation generation, recovery, and work hardening produces a steady-state density of dislocations at higher strains, and a steady-state strain rate for constant stress. This steady state is known as secondary creep [81].

The direction of movement of a dislocation is the Burgers vector, denoted by b_i. We will denote the normal to the slip plane by m_i. A slip system is the same Burgers vector and slip plane normal, repeated over the crystal structure. Slip systems are defined by the Schmid tensor, $E_{ij} = b_i m_j$. The resolved shear stress on each slip system is given by,

$$\tau_s = E_{ij} S_{ij} \tag{1.1}$$

where S_{ij} is the deviatoric stress experienced by the crystal. The rate of shearing γ on the slip system is given by the following relation,

$$\gamma = B|\tau_s^{n-1}|\tau_s \exp\left(-\frac{Q}{RT}\right) \tag{1.2}$$

Here, B is a constant, Q is the activation energy of the slip system, R is the universal gas constant, and T is the temperature. The exponent n is roughly 3 for steady-state dislocation creep in ice [81], which is the regime glacial ice is usually in.

In ice, easy slip only occurs on the basal plane, where the normal to the plane m_i is given by the c-axis c_i. Slip in either prismatic or pyramidal planes is on the order of 100 times harder [28]. This is the mechanism behind the extreme level of plastic anisotropy of ice compared to most other materials.

Other deformation mechanisms besides basal dislocation slip are usually active in deforming ice. Dislocation glide on the basal plane provides two independent slip systems (corresponding to the two degrees of freedom of the plane). However, a minimum of five independent slip systems is needed to accomodate arbitrary deformations [80]. During deformation, grains well-oriented towards basal slip will begin to deform, but are blocked by hard-oriented grains. The resulting stress may be relieved through several mechanisms. Grain boundary sliding can occur to maintain compatibility between adjacent grains. Non-uniform deformation involving bending of the lattice may occur within grains. This can result in the formation of subgrain boundaries [65]. In addition, slip along prismatic planes may occur in some circumstances [65].

The most commonly used constitutive relation for isotropic ice is Glen's flow law [39], which is closely related to Eq. (1.2):

$$D_{ij} = BS_{ij}\tau_e^{n-1}\exp\left(-\frac{Q}{RT}\right), \tag{1.3}$$

where τ_e is the effective stress, and D_{ij} is the strain-rate tensor. The exponent n is usually set to 3, in common with the exponent for steady-state dislocation creep.

To maintain compatibility with other grains (and the externally applied strain), lattice rotation occurs during dislocation creep. This induces c-axes to rotate towards directions of principal compression. For example, in vertical compression prominent near ice divides, c-axes rotate towards vertical. This makes the ice harder under applied vertical compression, since there is is a smaller component of shear stress along the basal plane. In the extreme case where a grain pointed exactly vertically is subjected to vertical compression, there is no resolved shear stress on the basal plane. Thus, the crystal does not deform through basal glide at all.

In the case where deformation occurs solely due to slip on the basal plane, the rate of c-axis rotation due to lattice rotation is given by a modified Jeffery's equation [58],

$$\dot{c_i} = V_{ij}c_j - D^g_{ij}c_j + c_i c_j c_k D^g_{jk}. \tag{1.4}$$

Here V_{ij} is the bulk vorticity tensor, corresponding to externally applied spin. The quantity D^g_{ij} is a component of the strain-rate tensor experienced by the grain (rather than the global strain rate). The last term of Equation (1.4) ensures that the rotation of the c-axis is tangent to the sphere, to maintain unit length. This can be seen by noting that the $V_{ij}c_j$ term does not affect the magnitude of c_i, leaving only the $D_{ij}c_j$ term. Assume that at time $t = 0$, the c-axis is given by $\mathbf{c}_0$. After a short length of time δt, the magnitude of the new c-axis $\mathbf{c}_{\delta t}$ is (without the final term in Equation 1.4),

$$\begin{aligned} ||\mathbf{c}_{\delta t}|| &= ||\mathbf{c}_0 - \delta t \boldsymbol{D}\mathbf{c}|| && (1.5)\\ &\approx ||\mathbf{c}_0|| - \mathbf{c}_0^T \boldsymbol{D}\mathbf{c}_0 \delta t && (1.6)\\ &= 1 - \mathbf{c}_0^T \boldsymbol{D}\mathbf{c}_0 \delta t, && (1.7) \end{aligned}$$

to first order in δt. Thus, for the c-axis to maintain unit length, we must add the quantity $\mathbf{c}^T \boldsymbol{D}\mathbf{c}\delta t$ projected onto $\mathbf{c}$, by multiplying by $\mathbf{c}$. This then gives the last term of Equation (1.4).

While deformation-induced grain rotation is the most important process governing fabric development in ice sheets, other processes play a role in both fabric development and ice rheology. There is evidence that grain size plays a significant role in ice deformation. Cuffey et al. [18] used observations from the Meserve Glacier in Antarctica to argue that grain-size variations explain a significant amount of enhanced shear in ice-age ice in Greenland.

Grain growth, in which some grains grow at the expense of others, occurs throughout ice sheets. Normal grain growth is most prominent in upper layers of ice sheets, where grains are not yet highly strained. Here, large grains grow at the expense of small grains due to differences of curvature. Grain boundaries with high curvatures have more unmade bonds per unit area; these unmade bonds possess free energy. Smaller grains have higher positive curvature over more of their boundary than large grains, making it energetically favorable for large grains to consume small ones [59].

As grains become more highly strained, the process of polygonization (also known as rotation recrystallization) works against normal grain growth. As noted previously, bending of the crystal lattice induces the formation of subgrain boundaries, because dislocations lying in different basal planes can minimize their strain energy fields by lining up. As this process continues, and the subgrain misorientation increases, the subgrains become distinct grains. This process also reduces the work-hardening of grains, since dislocations are moved from grain interiors to the new grain boundaries. Polygonization causes changes in grain orientation of no more than a few degrees [6]. It does not significantly change the resolved shear stress of the resulting child grains.

In contrast to polygonization, dynamic recrystallization (also known as migration recrystallization or discontinuous recrystallization) can greatly change grain orientations. Highly strained grains have a high dislocation density, which carries a great amount of strain energy. Newly nucleated grains with low dislocation densities can then easily grow, with the reduction in dislocation density providing the main driving force. These grains are typically well oriented for basal glide. Dynamic recrystallization typically occurs in waves, as new grains rapidly grow and consume the older, more strained grains (e.g. Montagnat and Duval [59]). This produces an interlocking texture of irregular, very large (up to several cm^3) grains. This provides an important mechanism to control the strength of ice fabrics deep in ice cores. In particular, near ice divides, it limits the tendency of c-axes to line up to vertical under the applied vertical compression. This limits the hardness of the ice under the applied stress. Dynamic recrystallization is usually active only above about $-10°$C, which occurs in deeper layers in most ice-sheet locations. Although, dynamic recrystallization is evident in layers as shallow as 200m at Siple Dome at temperatures of around $-20°$C [21].

1.2.2 Homogenization

A key difficulty of any continuum treatment of anisotropic ice is stress and strain homogenization: Stress and strain of individual grains must be consistent with the global stress and strain of the entire polycrystal. The homogenization scheme must also be tractable. There are two possible end-members. First, the Taylor-Bishop-Hill model [74] assumes homogeneous strain among grains, while allowing stress between grains to vary so as to produce the required global strain. This method is well-suited to materials with several active slip systems. It also has the advantage of avoiding overlap between grains: because every grain has the same strain, compatibility is guaranteed. An alternative approach is the Sachs model [69], which assumes homogeneous stress among grains. The strain of each grain is such that the global stress is maintained. This model does not produce strain compatibility, which can produce nonphysical overlaps between grains. Nonetheless, it produces better bulk strain and stress predictions for ice than the homogeneous strain model, because ice typically has only two active slip systems.

In the middle between these two are visco-plastic self-consistent (VPSC) schemes [52]. Here, each individual grain is treated as an ellipsoidal inclusion in an infinite, homogeneous matrix with the average properties of the polycrystal (the homogeneous equivalent medium).

Figure 1.1: Cartoon of an individual ice crystal with the basal plane and c-axis shown.

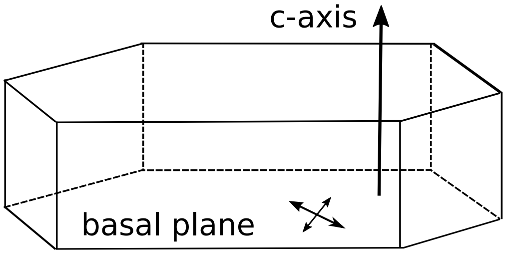

This allows for stress and strain to be dependent on grain orientation, which is more realistic than the homogeneous stress or homogeneous strain assumptions. However, it requires iterative solutions: the deformation of each grain is dependent on the properties of the homogenenous equivalent medium, which is in turn dependent on the properties of every other grain. This makes the VPSC scheme difficult to directly apply in many applications, such as ice flow models or continuum fabric evolution models. However, Gillet-Chaulet et al. [38] sidestepped this problem by instead fitting a parameterized constitutive relation to the results of a VPSC model over a grid of fabric parameters.

1.2.3 Orientation distribution functions (ODFs)

The distribution of ice-crystal c-axes may be described by an orientation distribution function, or ODF. These are also known as crystal orientation distribution functions (COFs). ODFs are probability distributions of c-axes defined on the unit sphere. Despite the name, ODFs are not necessarily true fuctions, as is the case with the discrete ODF given by the crystals of a thin-section sample. Since a c-axis $\mathbf{c}$ cannot be distinguished from $-\mathbf{c}$ due to ice crystals having reflectional symmetry about the basal plane, ODFs are antipodally symmetric. Due to this antipodal symmetry, ODFs are commonly restricted to the upper hemisphere. Throughout most of this thesis, we instead treat the ODF as being defined on the entire sphere for mathematical convenience.

Orientation tensors

Orientation distribution functions are often summarized using symmetric orientation (or, moment) tensors [2]. These tensors are used throughout this thesis. The element with index $i_1, ..., i_n$ of the n^{th} order orientation tensor $T_{i_1,..,i_n}$ is given by the outer product of of the c-axis with itself, n times, averaged over the ODF,

$$T_{i_1,..,i_n} =< \prod_{j=1}^{n} c_{i_j} > . \tag{1.8}$$

Since ODFs are antipodally symmetric, odd-order tensors are zero. Usually the fabric is described with only the second-order orientation tensor $A_{ij} =< c_i c_j >$. This is a symmetric, 3×3 tensor. The second-order orientation tensor is also the covariance tensor of the ODF if it is viewed as a distribution in Cartesian space with support confined to the sphere. The definition of covariance of a distribution is the second moment about the mean, given by,

$$\text{Cov}(c_i, c_j) =< (c_i - < c_i >)(c_j - < c_j >) > \tag{1.9}$$

Since the mean (or first-order orientation tensor) $< c_i >$ is zero due to antipodal symmetry, this reduces to $A_{ij} =< c_i c_j >$.

Because it is symmetric, there exists a reference frame where A_{ij} is diagonal with eigenvalues $\lambda_1 \leq \lambda_2 \leq \lambda_3$ which sum to unity. They sum to unity by construction because all c-axes lie on the unit sphere. The corresponding eigenvectors are also known as fabric principal directions. The eigenvalues correspond to concentrations of fabric in each principal direction. The principal direction associated with the largest eigenvalue λ_3 has the highest concentration of c-axes, and the principal direction association with λ_1 has the lowest concentration. The eigenvalue λ_2 is associated with the direction orthogonal to the other two.

If $\lambda_3 \approx \lambda_2 \approx \lambda_1$, then the fabric is isotropic, with c-axes distributed nearly uniformly across the sphere. If instead $\lambda_3 \gg \lambda_2 \approx \lambda_1$, then the fabric is known as a single-maximum, or pole fabric. In the case where $\lambda_3 \approx \lambda_2 \gg \lambda_1$, then the fabric is a girdle fabric, with a

Figure 1.2: Schmid plots of thin sections taken from the WAIS divide ice core. Each dot represents the c-axis orientation of a single grain. An azimuthal equal-area projection is used, such that a grain in the center of the circle is vertical, and a grain on the edge has a horizontal c-axis. **A** is an approximately isotropic fabric ($\lambda_3 \approx \lambda_2 \approx \lambda_1$); **B** is a girdle fabric ($\lambda_3 \approx \lambda_2 \gg \lambda_1$); **C** is a single-maximum fabric ($\lambda_3 \gg \lambda_2 \approx \lambda_1$).

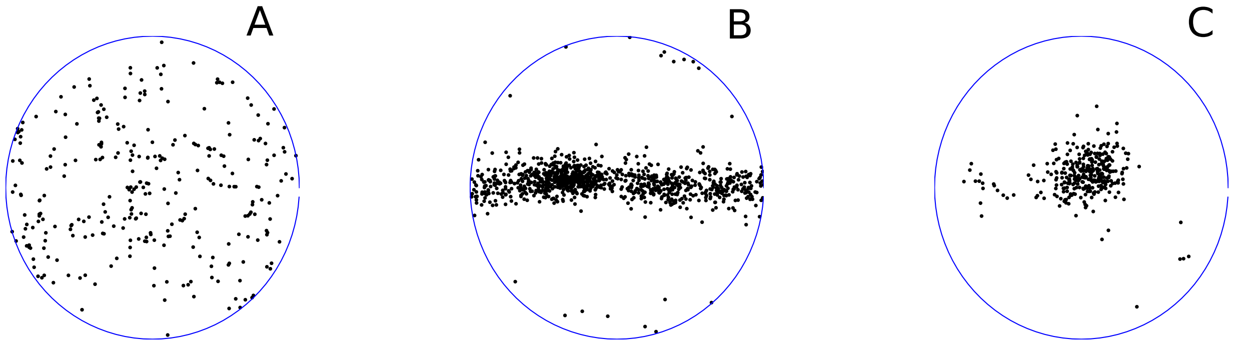

concentration of c-axes lying near the great circle orthogonal to λ_1. Examples of each of these fabric types from the West Antarctic Ice Sheet (WAIS) divide ice-core [30] are shown in Figure 1.2.

The fourth-order orientation tensor $\mathbb{A}_{ijkl} =< c_i c_j c_k c_l >$ is also necessary for many flow and fabric evolution calculations. While it is not typically used to describe ice fabrics, it can account for more complex fabric types, such as fabrics with multiple maxima. In practice, this is usually estimated from the second-order orientation tensor through closure approximations (see next section).

Zheng and Zou [84] showed that an ODF may be expressed as as an expansion of orthogonal traceless basis-functions, with coefficients derived from orientation tensors. The first two terms of this expansion are given by,

$$\psi(\mathbf{c}) = \frac{1}{4\pi} + \frac{15}{2}\left(A_{ij} - \frac{1}{3}\delta_{ij}c_i c_j\right) + ... \tag{1.10}$$

If we are working in the reference frame defined by the fabric principal directions, such that the second-order orientation tensor is diagonal, the link between fabric eigenvalues and ODF density can be readily seen. Unfortunately, this series expansion approach is not usually useful to describe most fabrics. If the expansion is truncated at the second-order, as above, the second-order orientation tensor of the truncated distribution is not necessarily the same A_{ij} it is parameterized by (i.e., A_ij on the right-hand side of Eq. 1.10). In particular, the second and fourth-order trunctions cannot represent very strong single-maximum fabrics. Basis functions and coefficients beyond the fourth order have unfeasibly many terms.

1.2.4 Continuum fabric evolution models

Eq. (1.4) gives the rotation rate of a single grain. When modeling bulk fabric, it is not practical to treat each grain individually. Instead, we may derive an evolution equation for the second-order orientation tensor A_{ij}. This has only six unique components, reducing an expensive computational problem to a small ODE system. Suppose that we have an ODF $\psi(\mathbf{c})$ giving the density of c-axes at $\mathbf{c}$.

$$\frac{dA_{ij}}{dt} = < \dot{c}_i c_j > + < c_i \dot{c}_j > . \tag{1.11}$$

Replacing $\dot{c}$ in the above equation with Eq. (1.4), we arrive at the following evolution equation for the material derivative of A_{ij}:

$$\frac{dA_{ij}}{dt} = V_{ik}A_{kj} - A_{ik}V_{kj} - D_{ik}A_{kj} - A_{ik}D_{kj} + 2\mathbb{A}_{ijkl}D_{kl}. \tag{1.12}$$

The last term involves the fourth-order orientation tensor $\mathbb{A}_{ijkl}$, which introduces the closure problem: to determine the evolution of the second-order orientation tensor, we need the fourth-order orientation tensor. We could similarly use an evolution equation for the fourth-order orientation tensor, but the sixth-order orientation tensor would appear in that equation, and so on. Thus, we need some way to approximate the fourth-order tensor $\mathbb{A}_{ijkl}$ in terms of A_{ij}. In the fiber literature, a vast array of closure approximations have been proposed to solve this problem. I will discuss a few here.

Perhaps the simplest is the quadratic closure, where $\mathbb{A}_{ijkl} = A_{ij}A_{kl}$. This is exact in the case of perfectly concentrated fabrics, where $\lambda_3 = 1$. It is quite accurate whenever

$\lambda_3 > 0.8$, and produces reasonably accurate predictions for the c-axis rotation rate even for diffuse fabrics. The quadratic closure is still the most common closure used for industrial fiber-orientation models due to its simplicity and reasonable accuracy.

Another simple closure is the linear closure,

$$\begin{aligned}\mathbb{A}_{ijkl} = -\frac{1}{35}(\delta_{ij}\delta_{ij} + \delta_{ij}\delta_{ij} + \delta_{ij}\delta_{ij}) \\ + \frac{1}{7}(A_{ij}\delta_{kl} + A_{ik}\delta_{jl} + A_{il}\delta_{jk} + A_{kl}\delta_{ij} + A_{jl}\delta_{ik} + A_{jk}\delta_{il}).\end{aligned} \quad (1.13)$$

The linear closure is exact for isotropic fabrics, but produces invalid predictions for strong single-maximum fabrics. Therefore, it is not a good choice itself as a closure approximation in ice, because strong single-maximum fabrics are common in deeper layers of ice sheets. The hybrid closure [3] instead takes a weighted average of the linear and quadratic closures, where the weighting is usually dependent on the largest eigenvalue λ_3. This can exactly represent both isotropic fabrics and perfect single-maximum fabrics.

Other, more sophisticated closures exist. Chung and Kwon [16] proposed the invariant-based orthotropic fitted (IBOF) closure. This closure writes $\mathbb{A}_{ijkl}$ using polynomial functions of the invariants of A_{ij}. The coefficients of the polynomial functions are fitted to a particular assumption of the form of the ODF, or to empirical data. This closure approximation was used by Gillet-Chaulet et al. [38] by fitting to an analytical distribution.

Lastly, I examine the fast exact closure [63]. If a fabric is initially isotropic, and evolves only due to lattice rotation from basal slip, then the ODF has the following form:

$$\phi(\mathbf{c}) = \frac{1}{4\pi(\mathbf{c}^T\mathbf{B}\mathbf{c})^{3/2}} \quad (1.14)$$

where $\mathbf{B} = \mathbf{C}^T\mathbf{C}$ has a determinant of unity and $\mathbf{C}$ follows the equation,

$$\frac{d\mathbf{C}}{dt} = -\mathbf{C}(\mathbf{D} + \mathbf{W}) \quad (1.15)$$

Rather than solving the Jeffery's equation (1.12) directly, only the previous ODE (1.15) must be integrated. This sidesteps the closure problem entirely. The orientation tensors A_{ij} and $\mathbb{A}_{ijkl}$ can be easily recovered using Carlson symmetric integrals. However, it is not necessary to compute $\mathbb{A}_{ijkl}$ in order to integrate the evolution of the fabric through time. This closure is not exact in the case of ice fabrics, since they typically are not initially isotropic, and do not follow the distribution given by Eq. (1.14) exactly. However, I have found that this distribution does an excellent job of approximately fitting thin-section data. This suggests that this closure approximation would be accurate in practice for predicting ice fabric development. The IBOF closure used by Gillet-Chaulet et al. [38] is in fact a polynomial approximation to this closure. Compared to the IBOF closure, the fast exact closure has a simpler implementation and better theoretical motivation. In addition, it is also more computationally efficient if A_{ij} and $\mathbb{A}_{ijkl}$ do not need to be computed at every timestep.

1.3 Outline

This thesis is divided into four main chapters, corresponding to four manuscripts. In the second chapter, I examine statistics and sampling error in ice-core thin sections. I derive novel estimates of sampling error in fabric, and apply these estimates to thin-section data from the WAIS divide ice-core [30]. I show that thin-section sampling error can be large under area-weighted thin sections. I also introduce a new parameterized ODF to glaciology, and compare the fits of this and other distributions in the WAIS and Siple Dome ice cores.

The last two main chapters examine the sensitivity of anisotropic flow to perturbations of flow and fabric. In the fourth chapter, I examine the sensitivity of ice fabrics to velocity gradient perturbations. I show that small velocity-gradient perturbations can induce tilted-cone fabrics in simple shear and pure shear, where the direction of greatest c-axis concentration is not vertical. These fabrics can induce vertical motion in horizontal simple shear.

The fifth chapter is an expansion on the third: given that small velocity perturbations can cause significant fabric perturbations, can the dynamics of coupled ice flow and fabric evolution cause these perturbations to grow further? I examine this by developing an analytical first-order model of coupled anisotropic ice flow and fabric perturbations. I show that under pure shear and simple shear, fabric perturbations in single-maximum fabrics can be unstable.

The contributions of this thesis are significant in several ways. I provide a thorough examination of methods of measuring crystal orientation fabrics in boreholes. The rigorous estimates of thin-section sampling error I developed are generally larger, and more realistic than previous estimates. Accurate estimates of uncertainties will aid usage of fabric data for paleoclimate interpretation. In addition, my uncertainty estimates may also be useful to inform thin-section sampling done in future ice cores. Finding the best number and the best locations of thin-section samples for an ice core is a trade-off between consumption of limited core ice, labor, accuracy, and spatial coverage. By providing accurate estimates of uncertainty based on grain-size distributions and fabric eigenvalues, these decisions can be better justified.

Inference of fabric using sonic velocities and thin-section measurements is a promising technique to combat sampling error or bias in sonic measurements, and sampling error in thin sections. Borehole sonic logging has received increased interest over the past several years. Given that thin-section measurements usually taken from ice cores anyway, this technique can improve accuracy with little cost. My statistical approach to fabric inversion also makes fewer assumptions on the form of the ODF compared to previous work. It is also an innovative use of the Google Tensorflow machine learning library for a geophysical inversion problem. This has the potential to be a convenient tool to use in other, similar problems.

The last two chapters of this thesis provide the most comprehensive examination of stability of ice-crystal fabrics to date. Stratigraphic disruption due to anisotropy has received little attention, despite being the most plausible cause of smaller-scale stratigraphic disturbances seen off the bed. In addition, anisotropy probably plays a strong role in large-scale folding and stratigraphic disruption in basal ice, due to its ability to create very large differences in viscosity. The work in this thesis is a start to understanding this complicated topic.

Chapter 2

STATISTICAL ASPECTS OF ICE-CRYSTAL ORIENTATION FABRICS

This chapter is in review at the Journal of Glaciology, with Ed Waddington as co-author. I developed the statistical results and wrote this manuscript. Ed Waddington helped edit the manuscript and contributed useful discussions.

Abstract: Ice crystal orientation fabric has a large effect on polycrystalline ice flow due to the strong plastic anisotropy of individual grains. The crystal orientation fabric can be described as an orientation distribution function (ODF), which is a probability distribution defined on the sphere for the direction of crystal c-axes. From this viewpoint, we present several statistical results for ODFs. We introduce a parameterized ODF (PODF), the Bingham distribution, to glaciology. We compare the performance of this and other PODFs against measurements from the West Antarctic Ice Sheet (WAIS) and Siple Dome ice cores. We also examine the sampling error introduced by attempting to infer the larger-scale bulk ODF from a thin-section sample. We introduce new analytical expressions for sampling error, and examine the use of bootstrapping for estimation of sampling error. We show that sampling error of fabric parameters can be substantial. Finally, we examine sampling error from inferring enhancement factor in Glen's flow law from thin sections. We show that rheological properties of ice are very poorly constrained by thin-section measurements, due to the power-law constitutive relation of ice in the dislocation-creep regime.

2.1 Introduction

An individual ice crystal has an anisotropic creep response, deforming most easily in shear parallel to the crystal basal-plane, orthogonal to the crystallographic c-axis. Plastic deformation of an ice polycrystal depends on the orientations of its constituent grains (e.g. Azuma [8]), which is described by the c-axis orientation distribution function (ODF). The ODF is a probability distribution of c-axis density often defined on the upper hemisphere (because a c-axis vector $\mathbf{c}$ is indistinguishable from $-\mathbf{c}$). In this paper, we will instead treat the ODF as being an even function defined on the entire sphere for mathematical convenience. A polycrystal with an isotropic ODF will have a bulk isotropic response to applied stress. However, polycrystals develop an anisotropic ODF in response to applied strain.

The development of a preferred orientation is guided primarily by intracrystalline slip. Due to interference among grains, there is a tendency for the c-axes to rotate away from the directions of principal extensional strain [10]. ODFs are often summarized using orientation (or, moment) tensors (e.g. Svendsem and Hutter [73]). We will make extensive use of index notation in this paper, due to the use of higher-order tensors. However, at times we will not follow the summation convention for notational convenience (this is noted when it occurs). In addition, throughout this paper, indices 1, 2, and 3 are associated with the x, y, and z directions, respectively. The second-order orientation tensor A_{ij} is the expectation $< c_i c_j >$, where $i, j = 1, 2, 3$. The mean of the ODF, $< c_i >$, is always zero because of antipodal symmetry. Therefore, A_{ij} is also the covariance matrix of the distribution, by definition of covariance as $\mathrm{Cov}(c_i, c_j) =< (c_i - < c_i >)(c_j - < c_j >) >$. The diagonal elements A_{11}, A_{22}, and A_{33} give a measure of the c-axis concentration on the x, y, and z axes, respectively. Similar to the second-order orientation tensor, the fourth-order tensor is the expected value $\mathbb{A}_{ijkl} =< c_i c_j c_k c_l >$. Since ODFs over the sphere are antipodally symmetric, odd-order tensors are zero. The symmetric second-order orientation tensor may be decomposed into non-negative eigenvalues and three orthogonal eigenvectors. The eigenvalues of $\mathbf{A}$ sum to unity by construction. The eigenvectors, or fabric principal directions, denote the directions of greatest density (corresponding to the largest eigenvalue), smallest density (the smallest eigenvalue), and a direction orthogonal to the other two. An isotropic fabric has three equal eigenvalues. A girdle fabric (in which there is a band of high concentration along a great circle) has two nearly equal eigenvalues, and one small eigenvalue. A single-maximum fabric

Table 2.1: List of symbols

Symbol	**Definition**
q_i	Component of a tensor in index notation
$\mathbf{q}$	Same tensor in vector notation
$\tilde{x}$	Sample estimate of a quantity x
c_i	ice-crystal c-axis for $i = 1, 2, 3$ in x, y, z directions
$\psi(\mathbf{c})$	Ice-crystal orientation dist. func.
$< q_i >$	Expected value of q_i under ψ
a_{ij}	Grain structure-tensor $c_i c_j$
A_{ij}	Comp. of the 2^{th} order orient. tensor $< a_{ij} >$
$\mathbb{A}_{ijkl}$	Comp. of the 4^{th} order orient. tensor $< a_{ij} a_{kl} >$
λ_i	Fabric eigenvalue of $\mathbf{A}$
$\mathbf{V}$	Matrix of eigenvectors of $\mathbf{A}$
ϕ	Zenith angle
θ	Azimuth angle
δ_{ij}	Kronecker delta symbol
S_2	Unit sphere
σ	A standard deviation
S_{ij}	Stress tensor
$\mathcal{B}$	Bingham distribution (Equation 2.3)
$\mathbf{L}$	Diagonal concentration matrix of $\mathcal{B}$
$\mathcal{D}$	Dinh-Armstrong distribution (Equation 2.4)
$\mathbf{R}$	Parameter matrix of $\mathcal{D}$
$\mathcal{F}$	Lliboutry's Fisherian distribution (Equation 2.1)
$\mathcal{W}$	Watson distribution (Equation 2.2)
κ	Scalar concentration parameter for $\mathcal{F}$
η	Scalar concentration parameter for $\mathcal{W}$

has one large eigenvalue, and two small ones. Small-girdle fabrics can also occur during active recrystallization, where a small ring of high density exists around the axis-preferred orientation of the applied strain and vorticity (typically centered around vertical).

It is common to approximate the unknown, true ODF with a parametric ODF (PODF), which can normally be fit to observed fabric data. This reduces the number of parameters. Among other uses, it is usually necessary to assume a specific PODF to numerically model fabric evolution. Numerous PODFs have been proposed. The majority have an axis of rotational symmetry, which is valid for single-maximum fabrics and symmetric girdle fabrics. Several PODFs have been developed that are motivated by analytical solutions to c-axis evolution valid in specific flow regimes (e.g. Staroszczyk and Gagliardini [72], Svendsem and Hutter [73], Gagliardini and Meyssonnier [33], Gödert and Hutter [41]). However, Gagliardini et al. [36] noted that these are special cases of the Dinh-Armstrong distribution [20]. This is a very flexible distribution that does not assume axial symmetry. Any initially isotropic fabric which evolves due only to deformation-induced grain rotation has this ODF. Other distributions have been proposed based on heuristic considerations (e.g. Thorsteinsson [75], Lliboutry [54]). More recently, Kennedy et al. [49] proposed the axially symmetric Watson distribution for use as PODF. For a complete overview of this topic, see Gagliardini et al. [36]. In this paper, we propose the Bingham distribution as an ODF, motivated primarily by statistical considerations. The Bingham distribution is a generalization of the Watson distribution.

Sampling error can be significant when inferring bulk properties of ice from a small thin-section sample. By “bulk properties” we mean those averaged out over large ice volumes. What constitutes a “larger volume” is somewhat arbitrary, but is at least as large as to render sampling error insignificant over the length scales of the larger volume. Sampling error is the error from approximating something (here, the bulk properties of ice) from a limited sample size. Therefore it is important to take sampling error into account when interpreting ice-sheet thin sections in order to properly interpret thin-section data. In addition, this sampling error can also be viewed as variability in the underlying ODF on the scale of thin sections. This can cause variability of anisotropic viscosity on the scale of thin sections.

Thorsteinsson [75] found that around 5000 grains are needed to effectively eliminate sampling error in a fabric model. Later on, Durand et al. [24] fit a quadratic estimate of the sampling error of $\mathbf{A}$ by generating an array of fabrics of 10,000 grains each, and resampling from these fabrics. Unfortunately, this method is not directly applicable to per-pixel measurements, such as with electron backscatter diffraction or automatic fabric analyzers, since it does not take into account the correlation of nearby measurements.. Here, we introduce an analytical estimate for the sampling distribution of fabric eigenvalues and eigenvectors based on data taken from a discrete thin-section sample, with either equal weighting of grains, or weighting by area. Generally, area weighting should be preferred, as it more accurately reflects the true fabric by giving a larger weight to larger grains [35].

When fabric eigenvectors and eigenvalues are derived using area weighting of crystals in thin sections, we show that sampling error can be greatly increased. We also numerically derive an estimate of the sampling distribution of enhancement factor [53] under simple shear from thin sections. This random variability for regions of several hundred grains can also affect small-scale flow. This may be a source of incipient layer folds, which can then be overturned by anisotropically-enhanced shearing deep in ice sheets [76].

2.2 Parameterized orientation-density functions (PODFs)

We now examine the use of PODFs. We discuss several previously used PODFs which we consider to be especially statistically and physically plausible. We introduce the Bingham distribution as a PODF. We then compare the log-likelihoods of the distributions fitted to thin-section data at the West Antarctic Ice Sheet (WAIS) Divide ice core and the Siple Dome ice core, to assess their performance.

2.2.1 Fisher and Watson distributions

Lliboutry [54] first suggested the use of an axially-symmetric Von Mises-Fisher type distribution. Expressed in a reference frame where the vertical axis is aligned with the symmetry axis, this is,

$$\mathcal{F}(\phi) = \frac{\kappa \exp(-\kappa \cos(\phi))}{e^{\kappa} - 1}, \tag{2.1}$$

where ϕ is the zenith angle, and κ is a scalar concentration parameter. Gagliardini et al. [36] found that this distribution provided the best fit for fabric in a thin section from the Dome C core. As a modification to the Lliboutry's Fisherian distribution, Kennedy et al. [49] introduced the Watson distribution for use as a PODF:

$$\mathcal{W}(\phi) = a \exp(-\eta \cos^2(\phi)), \tag{2.2}$$

where η is a concentration parameter, ϕ is the zenith angle, and a is a normalization constant. Note that by the double-angle formula, if the concentration parameters η (for the Watson distribution) and κ (for the Fisher distribution) are equal, then $\mathcal{F}(2\phi) \propto \mathcal{W}(\phi)$. Both of these distributions can represent single-maximum fabrics with positive concentration parameters, and the axis of symmetry parallel to the eigenvector associated with the largest eigenvalue. Likewise, girdle fabrics can be represented with negative concentration parameters, with the axis of symmetry parallel to the eigenvector associated with the smallest eigenvalue. The Watson distribution has the important advantage of being antipodally symmetric. Because individual ice-crystal orientations cannot be distinguished between $\mathbf{c}$ and $-\mathbf{c}$, any ice ODF defined on the sphere should also be antipodally symmetric. It is common practice to define ODFs only on the upper hemisphere. Any ODF defined on the upper hemisphere can trivially be extended to the whole sphere. However, this does not, in general, preserve smoothness (which is usually desirable). For the Von Mises-Fisher distribution of Lliboutry, the derivative of density with respect to ϕ does not vanish at the equator. If we extend this ODF to the whole sphere, the derivative is discontinuous at the equator. The discontinuity does not have a physical basis. This same difficulty appears when extending any distribution on the half to the full sphere whose density gradient does not vanish at the equator.

2.2.2 The Bingham Distribution

We now introduce the Bingham distribution [13] as a generalization of the Watson distribution. The density, in Cartesian coordinates, is

$$\mathcal{B}(\mathbf{c}) = \gamma(\mathbf{L}) \exp(-\mathbf{c}^{\mathbf{T}}\mathbf{V}\mathbf{L}\mathbf{V}^{\mathbf{T}}\mathbf{c}), \tag{2.3}$$

where $\mathbf{V}$ is the matrix of eigenvectors of the second-order orientation tensor $\mathbf{A}$, and γ is a normalization constant. Also, $\mathbf{L}$ is a diagonal matrix containing three concentration parameters ι_i such that $\iota_1 < \iota_2, \iota_3$. This distribution is invariant for changes in the sum of concentration parameters, because any change in the sum of concentration parameters is negated by a change in the normalizing constant $\gamma(\mathbf{L})$. Because of this, we may set $\iota_1 = 0$, since if the parameters are ι_i, with $\iota_1 \neq 0$, the distribution with concentration parameters $\iota_i - \iota_1$ is identical. This reduces the number of free parameters from three to two. If we set $\iota_2 = 0$ as well, the Watson distribution (Equation 2.2) is recovered. This distribution has a number of desirable properties. It is able to represent single-maximum fabric and girdle fabrics, but is also able to capture fabrics with three distinct eigenvalues, such as oblong maxima, or girdles that are concentrated in one direction.

In addition, the Bingham distribution is parsimonious. If we seek a PODF with a given $\mathbf{A}$, then the Bingham distribution avoids introducing spurious structures that are unnecessary to satisfy the assumption of a particular value of $\mathbf{A}$. Specifically, the Bingham distribution is the maximum-entropy distribution for any spherical distribution with a given second-order orientation tensor (or, covariance matrix) [55].

Distributional entropy is defined very similarly to thermodynamic entropy (the latter can be seen as a special case of the former). The entropy of a probability distribution q is the expectation $< -\log q >$. Distributions that have high entropy contain less information. Higher-entropy distributions are therefore more parsimonious (due to having less information). Thus, when selecting a parametric distribution, the distribution with the highest entropy that adequately fits the given data is the most parsimonious explanation of the observations. Such a distribution fits the data well, but without assuming extraneous information. In this sense, the Bingham distribution is similar to the multivariate normal distribution, which has maximum entropy of any distribution over n-dimensional Euclidean space possessing a given covariance matrix, or the exponential distribution, which has the maximum entropy of any distribution on the line with a given mean. The Bingham distribution is in fact the multivariate normal distribution with zero mean conditioned to lie on the unit sphere.

The Bingham distribution has found use in paleomagnetics [64] and other fields. However, its wider adoption has been hampered by a lack of closed-form analytical expressions for the normalization constant and the maximum-likelihood estimator of ι_i given the data, necessitating a greater use of slower numerical methods than many other distributions. However, this is not as great of a challenge as it once was. In addition, since the distribution is determined by two parameters, it is amenable to methods based on lookup tables.

In fitting a Bingham distribution to an observed fabric, only the second moment of the observed fabric, $\mathbf{A}$, is needed. Higher moments are neglected, which means the Bingham distribution cannot fit complex fabric distributions, such as those with multiple maxima. It is possible to derive distributions fitting higher moments. However, this would quickly become unwieldy. In addition, if the goal is to estimate a bulk fabric distribution from a limited thin-section sample, more complex distributions would tend to overfit the data.

2.2.3 The Dinh-Armstrong distribution

We now examine another distribution, which we will refer to as the Dinh-Armstrong distribution [20]. This is given by,

$$\mathcal{D}(\mathbf{c}) = \frac{1}{4\pi\left(\mathbf{c}^{\mathbf{T}}\mathbf{R}\mathbf{c}\right)^{\frac{3}{2}}}, \tag{2.4}$$

where $\mathbf{R}$ is a symmetric second-order tensor with a determinant of unity. Gillet-Chaulet et al. [38] introduced this distribution to glaciology for fabric evolution. If $\mathbf{c}$ rotates due only to slip on the basal plane, and if the ODF was at one time isotropic, then the ODF has this distribution with $\mathbf{R} = \mathbf{F}\mathbf{F}^{\mathbf{T}}$, where $\mathbf{F}$ the bulk deformation gradient. In the reference frame defined by the fabric principal-directions, $\mathbf{R}$ is a diagonal matrix, with diagonal entries b_i. The three elements b_i possess only two degrees of freedom, due to the constraint that the determinant is unity.

2.2.4 Comparison of PODFs

We now compare the Dinh-Armstrong distribution (Equation 2.4), the Fisherian distribution (Equation 2.1), and the Bingham distribution (Equation 2.3) using thin-section data from the WAIS Divide ice core [30] and the Siple Dome ice core [82]. We found a maximum-likelihood fit of each of these three distributions for each thin section. The data likelihood of a parameter value ω of a parameterized distribution f_ω is the probability of those observed data arising under the distribution f_ω (with the parameter value ω). The maximum-likelihood value of ω is the value of ω that maximizes this likelihood. That is, the maximum-likelihood estimator maximizes $\Pr(\mathbf{d}|\omega)$, where $\mathbf{d}$ is the observed data. In practice, the log-likelihood is maximized instead of directly maximizing the likelihood. Maximum-likelihood estimation is a standard way to fit distributions to data for many statistical tasks. It provides a coherent measure of the fitness of a distribution to data. Thus, comparing log-likelihoods of data for the maximum likelihood fits of these distributions is a fair way of comparing their performance.

For the Bingham distribution (Equation 2.3), we computed the maximum-likelihood density estimates of $\mathbf{L}$ numerically, given the observed grain orientations from the WAIS and Siple Dome ice-cores. For the Dinh-Armstrong distribution (Equation 2.4), we numerically found the maximum-likelihood estimates for the parameter $\mathbf{R}$. For Lliboutry's Fisherian distribution with a single-maximum fabric, we first rotated the reference frame into the fabric principal reference frame such that the eigenvector corresponding to the largest eigenvalue points vertical. For Lliboutry's Fisherian distribution with a girdle fabric, we rotated the reference frame such that the eigenvector associated with the smallest eigenvalue is vertical. We then numerically found the maximum-likelihood estimates for the concentration parameter κ. The results for all three PODFs, for both WAIS and Siple Dome, are plotted in Figure 2.1.

We consider the normalized log-likelihoods of thin-sections (normalized by either thin-section area or number of grains), rather than the likelihood of observing all grains in each thin section. Normalized log-likelihood gives the average likelihood of observing a grain from a thin section. This is necessary because the thin sections differ in the number of grains, so the likelihoods of each thin section (with all grains taken together) are not directly comparable. Everything else being equal, a sample with more grains will have lower likelihood than a sample with few grains. Note that we are plotting the *log-likelihood* of each distribution, for the maximum-likelihood values of the parameters $\mathbf{L}$, κ, and $\mathbf{R}$. We are not plotting the values of these parameters themselves, since they are not comparable between distributions, and they themselves give no information on the goodness of fit. The Fisherian distribution has the lowest log-likelihood for nearly all thin sections. The Bingham and Dinh-Armstrong distributions perform similarly, with the Bingham distribution slightly outperforming the Dinh-Armstrong distribution overall. For these data as a whole, this indicates that the Bingham distribution is the best choice due to its maximum-entropy property. However, the Dinh-Armstrong distribution does not have a normalization constant that must be found numerically, as the Bingham distribution does. Therefore, it may be a better choice for many applications. Different physical situations are not likely to be fit by a single ODF. However, both the Dinh-Armstrong (Equation 2.4) and Bingham (Equation 2.3) distributions have physical motivation, and may serve as good default PODFs.

All three PODFs are capable of exactly representing isotropic fabrics, and in the limit, perfect single maximum fabrics. Thus, they perform similarly in the less-anisotropic fabric near the top of the WAIS divide ice core. Log-likelihoods are usually lower for diffuse fabrics than for concentrated fabrics. In concentrated fabrics, most of the grains lie in orientation which have high ODF density, resulting in high likelihoods. In the limit of grains taken from a perfect single-maximum fabric, the likelihood of each grain is positive infinite. On the other hand, in the limit of an isotropic fabric, the unnormalized log-likelihood of every grain is always $-\log(4\pi)$. This is because the area of the surface of the sphere is 4π.

Figure 2.1: Log-likelihood of maximum-likelihood fits of the Dinh-Armstrong (Equation 2.4), Bingham (Equation 2.3), and Fisherian (Equation 2.1) distributions to WAIS and Siple Dome thin-sections. Higher log-likelihood indicates a better fit. The likelihoods are normalized by grain area for WAIS. For Siple Dome, they are normalized by the number of grains. The Dinh-Armstrong and Bingham distributions perform similarly, with the Lliboutry's Fisherian distribution having lower likelihood for almost all thin sections.

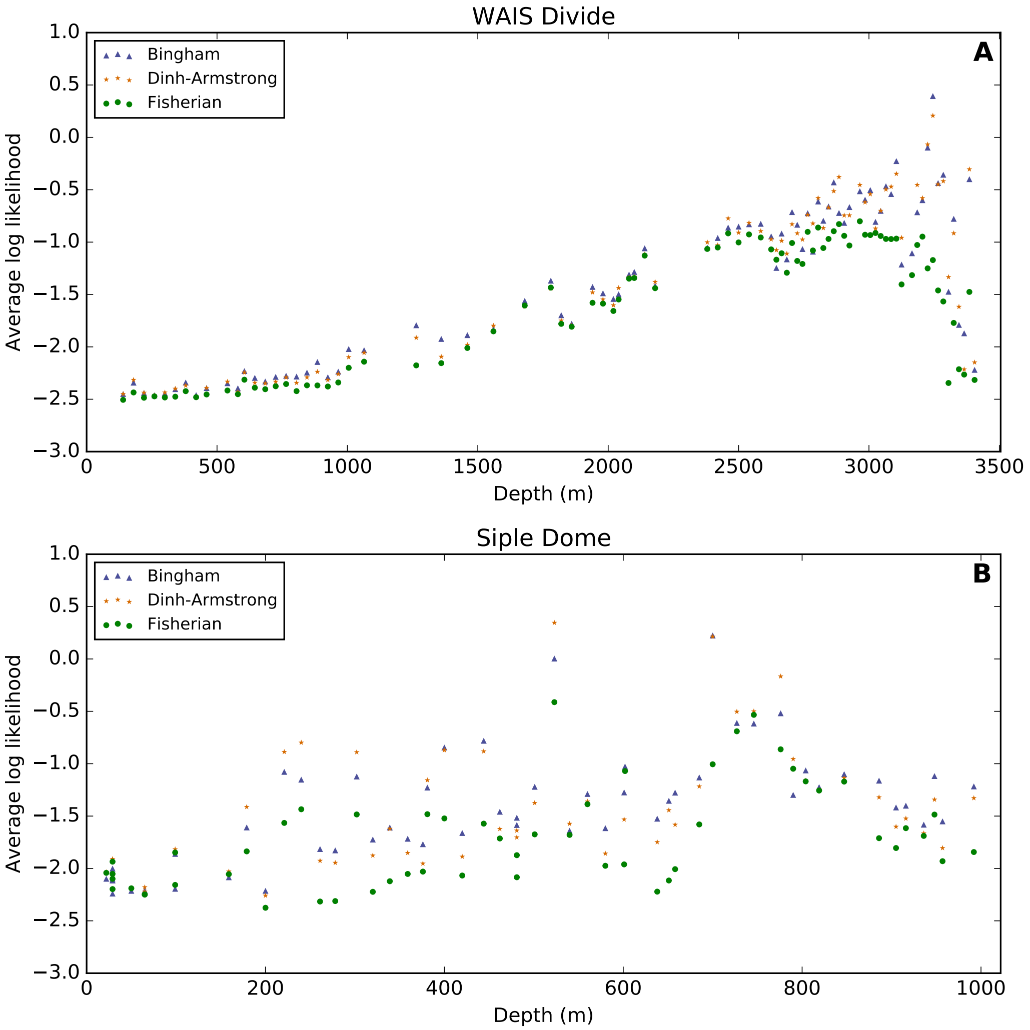

2.3 Sampling error in thin sections

C-axis measurements from ice-sheet thin-section samples provide a way of directly sampling c-axes from ice sheets. Sampled crystal c-axes can be assumed to be taken from some orientation distribution function. Thin-section samples are small in area, typically with a few hundred grains. Therefore, inferring the bulk fabric of the surrounding ice from thin-section samples is subject to sampling error. This introduces uncertainty in the inferred bulk ODF. However, this same error also reflects the variability of fabric properties on on the scale of thin sections (hundreds of grains), without assuming that grains from different regions are drawn from different distributions. Therefore, one may expect deformation to randomly vary over the same small length scales, even if the ODF is stationary across space. The true distribution of grain orientations may also be non-stationary in space, due to differences in material properties. This can result in inaccuracies, as a sample from a thin section may not be drawn from the same distribution as the bulk fabric. Therefore, due to sampling error and possible spatial non-stationarity, thin-section samples do not perfectly capture the larger-scale bulk-fabric ODF.

Several different methods have been developed to measure c-axes in thin sections. The Rigsby Stage technique [51] was the first method for c-axis determination in thin sections, using extinction angles of polarized light. This is a manual technique which gives per-grain measurements of c-axes. In recent years, automatic fabric analysers [83] and electron-backscatter diffraction (EBSD) [46] have become popular. These techniques yield high-resolution images of grain orientations, with c-axes measured per-pixel, rather than per-grain. Typically, there are many more pixels than grains. It may initially seem that the sampling error would be nearly eliminated, due to the very large number of pixels. However, in Appendix A1 we show this is not the case, because nearby pixels are usually highly correlated. We will also show that intragrain variability of c-axis orientations may be neglected when estimating sampling error from thin sections. From these two results, we show that sampling error of per-pixel measurements is similar to that of per-grain.

In this section, we assume that all grains from a thin section are drawn from the same underlying bulk distribution. This is distinct from the situation where there are actual differences in distribution across the thin section, for example if a thin section crosses a summer-winter boundary, or if vertical thin section includes a thin layer of high impurity content. By examining how much sampling error can be expected from thin sections, it is possible to infer whether variability among thin sections is real, or just an artifact of small sample size.

We are treating a collection of measurements from a thin section as a realization of a spatially-correlated sample from the underlying ODF. The empirical ODF of each thin section sample itself is completely deterministic, except for measurement error. However, here we are interested in the bulk ODF of the surrounding ice, not the crystal orientations of a particular slice of ice. Thus, it makes sense, for example, to consider correlations of c-axis measurements by looking at how they would be related under repeated thin-section samples taken from the same ODF. To get an intuitive idea of how spatial correlation works, suppose that we have a perfectly isotropic fabric. We choose a single point in this fabric, and look at its orientation. We previously had the least information possible about the orientation of this point, because it is an isotropic fabric. Once we select a sample of a single point, we know the orientation of that point perfectly. Now suppose we select a second point within the same grain. The c-axis orientation of this second point will be very close to the first. Therefore, we can predict the orientation of the second point very accurately. Thus, while they are both take from the same isotropic ODF, they are *dependent* on each other, because they are not independent samples from the ODF.

In Appendix A, we derive estimates of the sampling error of the estimate $\tilde{\mathbf{A}}$ of the bulk second order orientation tensor $\mathbf{A}$, appropriate for both per-pixel and per-grain c-axis measurments. From Equation (7), the variance of this sampling error can be estimated by,

$$\operatorname{Var}(\tilde{A}_{ij}) \approx (\mathbb{A}_{ijij} - A_{ij}A_{ij})\, s_n^2, \tag{2.5}$$

with no sum in i or j. Here, s_n^2 is the sum of squared grain areas, when the area of a thin section is normalized to unity. It reaches a minimum when all grains have equal sizes, and reaches a maximum when a single grain has a a normalized area approaching unity. It tends to be smaller for thin sections with more grains, reflecting the fact that having more data reduces uncertainty. This estimate applies whether the data are collected per-grain, as with manual fabric measurements, or per-pixel. We show in the appendix that intragranular misorientations can be ignored when estimating sampling error; thus per-pixel measurements can be averaged out for each grain. When per-pixel measurements are averaged within each grain, it is the same as if the data were collected on a per-grain basis in the first place. In Appendix A1, we also derive error estimates for fabric eigenvalues and eigenvectors from Equation (7) under the assumption that formulas for first-order eigenvalue and eigenvector perturbations are approximately valid.

2.3.1 Bootstrap estimates of sampling error

We now explore the use of bootstrap resampling for estimating fabric sampling error. Bootstrapping [29] is based on the idea that the empirical distribution of the observed data can be used as an approximation to the unknown true distribution. This requires that the data are approximately independent and are drawn from the same distribution. We can approximate the distribution of a statistic of interest that depends on the data (such as $\tilde{A}_{ij}$) by first resampling the empirical distribution many times, with replacement. The statistic is calculated for each resample, thus approximating the distribution of the statistic. In the case of per-grain c-axis measurements, this is straightforward, assuming that orientations of different grains are approximately independent.

Bootstrapping is not valid for resampling per-pixel measurements (with many pixels per grain) because of the high correlation of the orientations of nearby points within the same grain. The general idea of bootstrapping is that it is supposed to approximate repeated draws from the underlying distribution by resampling from the original sample. However, this does not work when the data are dependent, as is the case with per-pixel c-axis measurements. The data depend on one another, in that if we observe a pixel with a particular orientation, many other nearby pixels are likely to have the same orientation, conditioned on the first pixel. They are not sampled independently from the ODF. Simply resampling all data from a thin section ignores spatial correlation of the data, leading to a large underestimate of variance.

Instead, we suggest a technique known as block bootstrapping [43]. Block bootstrapping resamples blocks of data at a time, rather than individual datums. The goal is that the larger blocks are approximately uncorrelated. There is a tradeoff involved in choosing block sizes: larger blocks have less correlation with each other, which helps avoid underestimating variance. However, using blocks that are too large causes overestimation of the variance by making the effective sample size too small. Ideally, the variance within each block should be as small as possible, while maintaining approximate independence between blocks. An obvious choice for thin sections is to take individual grains as blocks: Within-block variance is small, since c-axes within a grain are not misoriented by more than several degrees. Likewise, the orientations between different grains are approximately independent from each other. By taking individual grains as blocks, block bootstrapping per-pixel c-axis measurements is identical to ordinary bootstrapping of per-grain c-axis measurements.

2.3.2 Sampling-error estimates for WAIS Divide

We now derive error estimates for the WAIS Divide core using both the analytical method developed in the appendix, and bootstrapping. The c-axis measurements were collected on a per-grain basis [30]. We compare the derived sampling distribution of fabric eigenvalues from both approaches in Figure 2.3. To assess uncertainty in fabric principal directions, we also compare the sampling distributions of the fabric Euler angles in Figure 2.4. The two methods match very closely for both eigenvalue and Euler angle sampling distributions.

The 95% central intervals of the area-weighted bootstrapped sampling distributions of A_{ii} (no sum) are plotted in Figure 2.2. For the WAIS core, the observed variability of the fabric eigenvalues over short length scales in depth seems to be primarily explained by sampling error. For the most part, it is not necessary to assume actual differences in the bulk ODF to explain these differences. The exception to this is near the bed, where there exists layers of recrystallized and non-recrystallized fabric [30]. The sampling error in this core tends to be more sensitive to fabric distribution than it is to sample size. The variance $(\mathbb{A}_{ijij} - A_{ij}A_{ij})s_n^2$ (no sum) tends to zero as fabric strength increases, towards a maximum eigenvalue of unity. In this limiting case, $\mathbb{A}_{ijij} = A_{ij}A_{ij}$ (no sum), and the eigenvalue variance is zero. Thus, sampled fabric eigenvalues and fabric eigenvectors have smaller variances for strong fabrics compared to weaker fabrics. For example, the fabric eigenvalues of the thin-section with weak fabric at 180m has similar variance than those of the strong fabric at 3265m thin-section. This is despite the fact that the 180m thin-section has nearly three times as many sampled grains as the 3265m thin section.

2.3.3 Sampling error in enhancement factor

Sampling error in fabric can lead to large uncertainties in flow characteristics. The Schmid factor is a measure of the proportion of compressive stress resolved on a c-axis basal plane. It is given by $S_g = \cos\chi \sin\chi$, where χ is the angle between the c-axis and the stress axis. Azuma [9] found that the scalar enhancement factor for ice flow under uniaxial compression depends on the fourth power of the Schmid factor averaged among grains. This assumption is also used for the CAFFE flow model [67]. The dependence on the fourth power indicates that smaller variations in c-axis fabric can induce much larger changes in deformation rates. In Figure 2.5, we used bootstrap resampling to estimate the sample distribution of the enhancement factor under simple shear for each thin section in the WAIS core. This is given by the fourth power of the average Schmid factor, scaled by the average Schmid factor of an isotropic polycrystal, which is 1/3. The enhancement factor can vary by 100% or more. The power-law viscosity of ice will tend to make smaller differences in fabric correspond to much larger differences in strain rate.

Figure 2.2: Estimates of the diagonal elements A_{ii} (no sum) of the second-order orientation tensor A_{ij} from fabric thin sections from the WAIS Divide core. The error bars are the 95% bootstrap confidence intervals of the observed area-weighted thin section A_{ii}.

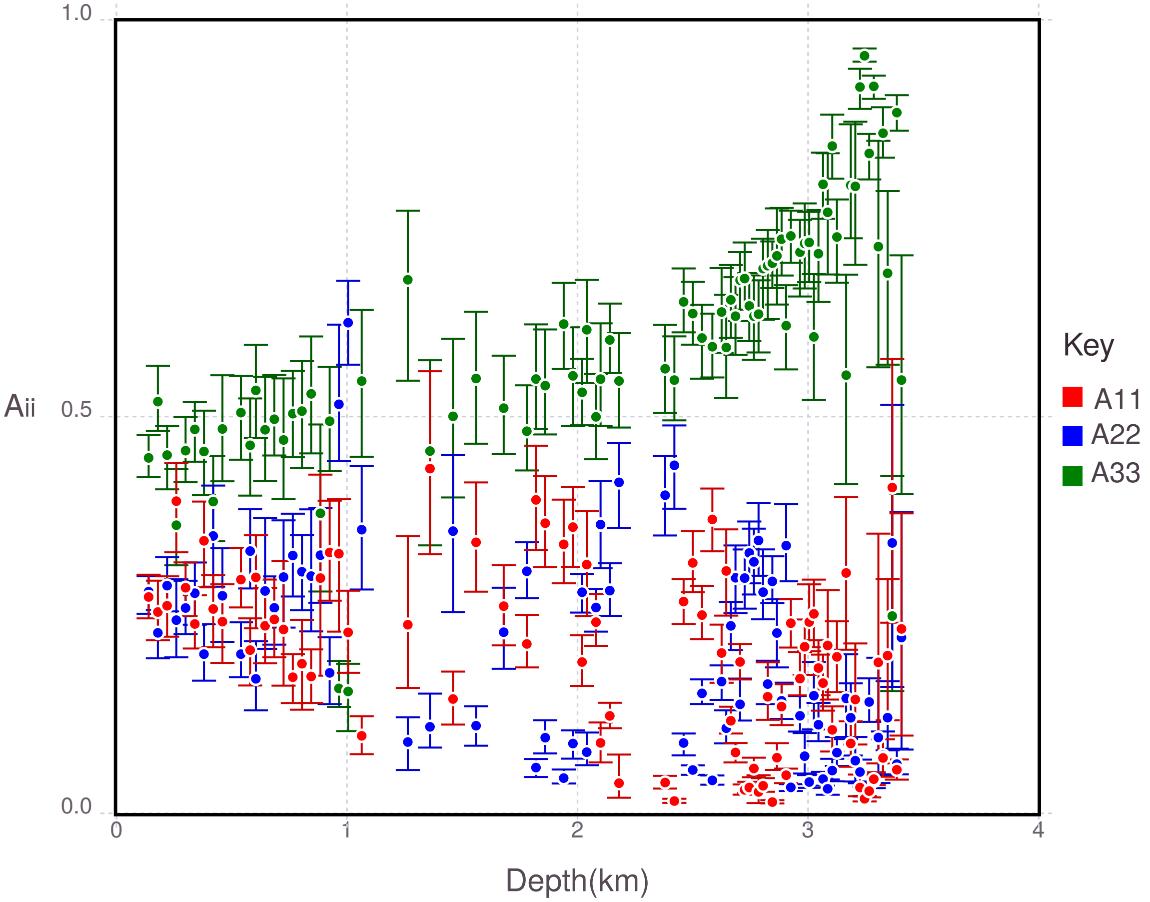

Figure 2.3: Bootstrap resampling and analytical estimates of the sample distributions of the eigenvalues of the thin section fabric at 140m. The analytical (dashed lines) and resampled bootstrap estimates (solid lines) match closely. Because the fabric is rather weak, there is still a moderate amount of uncertainty despite this sample having 1405 grains.

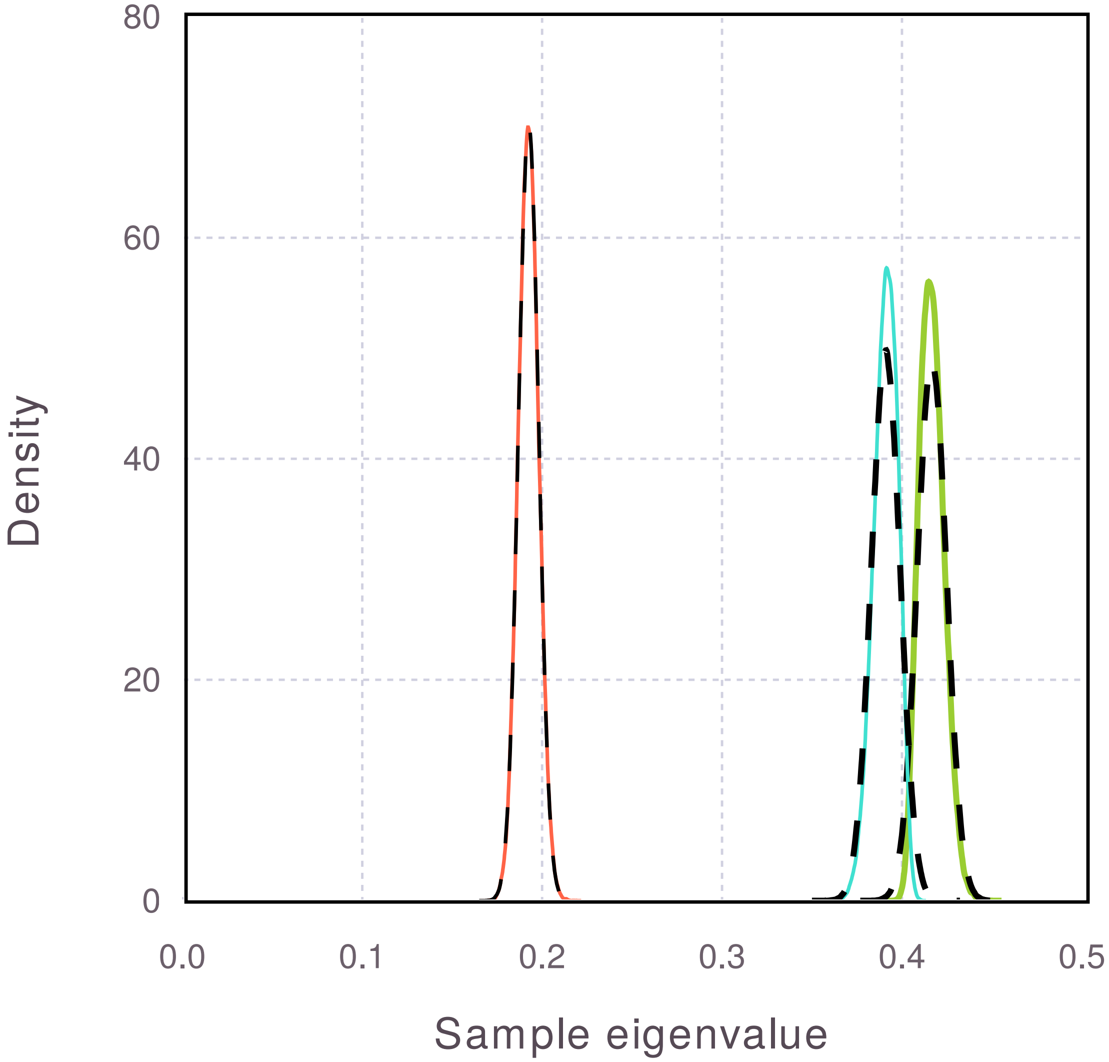

Figure 2.4: Bootstrap resampling and analytical estimates of the sample distributions of the error in fabric Euler angles of the thin section fabric at 140m. The analytical and resampled bootstrap estimates match closely. The smallest eigenvalue has a wide distribution in the associated Euler angle, because the other two eigenvalues are close.

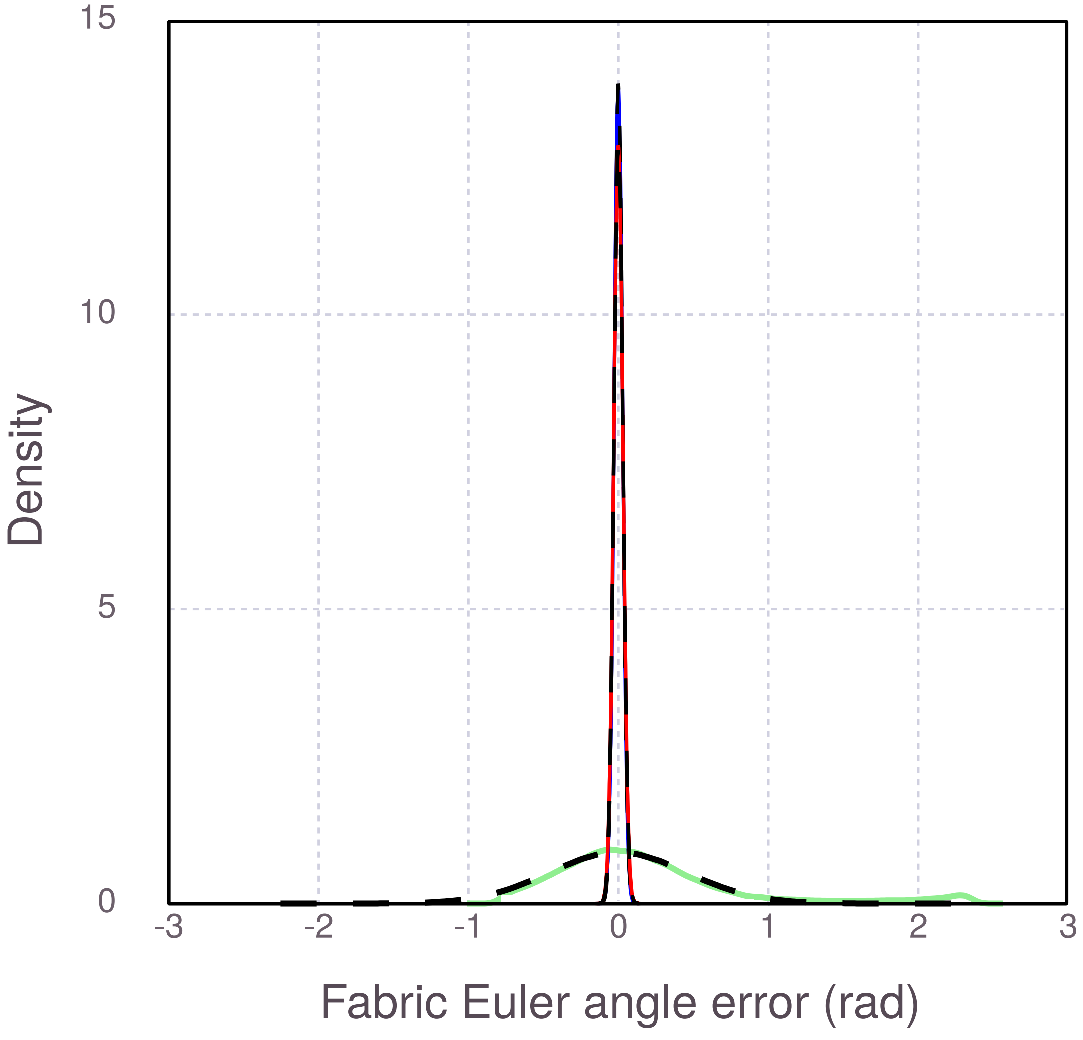

Figure 2.5: Bootstrap 95% confidence intervals for enhancement factor for the 83 WAIS thin sections. Due to the dependence on the fourth power of the average Schmid factor, the confidence intervals are wide.

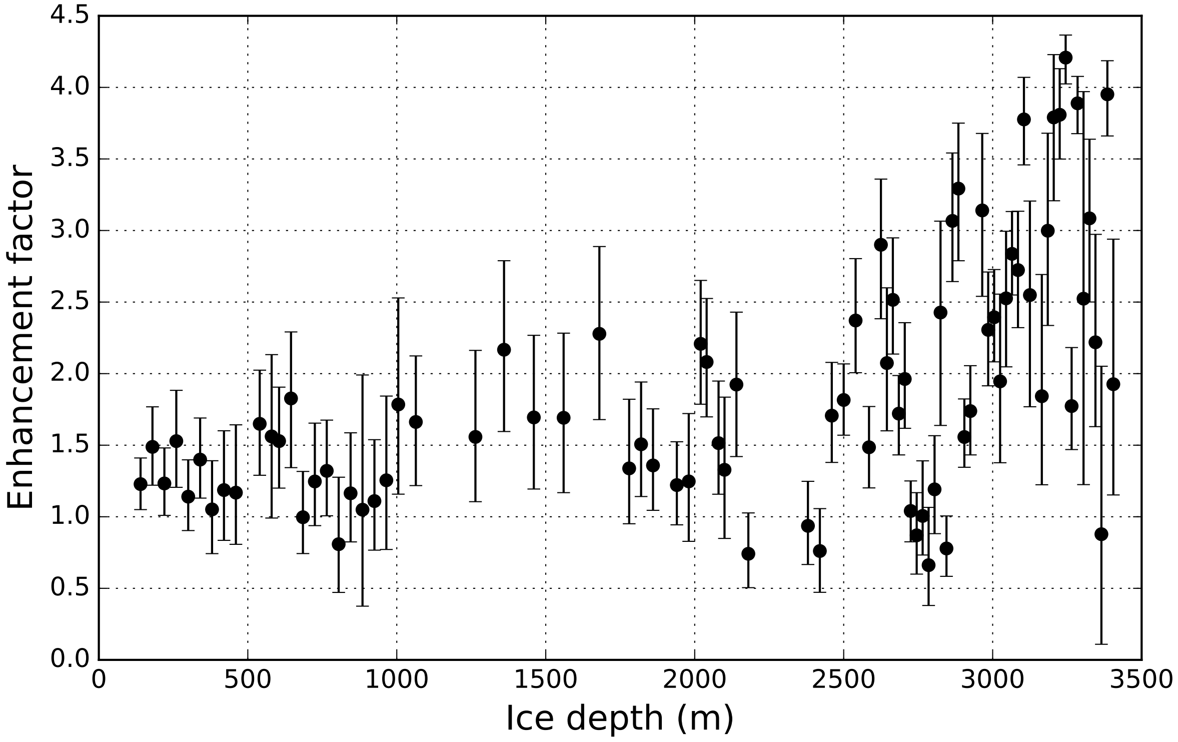

2.4 Conclusions

We compared PODFs with their log-likelihoods for different observed thin sections. This is a standard technique to fit probability distributions. The Bingham distribution (Equation 2.3) and the Dinh-Armstrong distribution (Equation 2.4) perform nearly equally for the WAIS and Siple Dome ice-core thin sections. Lliboutry's Fisherian distribution (Equation 2.1) did not fit the thin sections as well. This is chiefly because the Fisherian distribution assumes axial symmetry. Axial symmetry, which is an assumption used by many previously proposed PODFs, is not capable of accurately approximating ODFs with three distinct fabric eigenvalues. Ice fabric in most realistic situations has three distinct eigenvalues. However, the ideal parameterized ODF may not be the same in all situations.

Inferring larger-scale bulk fabric from limited thin section samples is subject to sampling error. We showed analytical estimates of eigenvalue and eigenvector sampling error. Eigenvalue and eigenvector sampling error depends strongly on fabric strength, with single-maximum fabrics having smaller eigenvalue and eigenvector variances than diffuse fabrics, for the same sample size. Thus, to achieve the same certainty in fabric ODF, larger sample sizes are needed for diffuse fabrics. We also examined bootstrapping of per-pixel EBSD or automatic fabric analyzer measurements of thin section data. It is necessary to use block bootstrapping for per-pixel data, rather than ordinary bootstrapping. Ordinary bootstrapping neglects covariances between nearby pixels, which causes sampling error to be severely underestimated. Sampling error estimates are sensitive to the grain size distribution. Often, thin sections are dominated by a few large grains, with many smaller ones. This results in much larger sampling uncertainties than even grain-size distributions. The estimates of sampling error distributions for the WAIS core show that fabric eigenvalues are very poorly constrained for some thin sections. Sonic fabric measurements are a promising way of overcoming this inaccuracy (e.g., Diez and Eisen [19], Maurel et al. [57]).

These results indicate that fabric variability is likely important for small-scale flow. As ice experiences power-law creep, relatively small variations in fabric strength can have a large impact on flow. Volumes of several hundred to several thousand grains can be expected to display a fairly large amount of fabric variability, indicating that ice flow characteristics are unpredictable at those length scales. We may also expect regions of ice with larger grain-sizes to experience significant fabric variability from sampling effects over larger length scales than regions with small grain sizes, as a doubling of average grain radius will roughly double the length over which sampling variability is important. Sampling variability may provide an impetus for layer overturning or boudinage on small length scales.

Acknowledgements

We thank Joan Fitzpatrick and Don Voigt for the WAIS thin-section data. We also thank Maurine Montagnat and Ilka Weikusat for helpful discussions on thin-section uncertainty. This work was supported by the National Science Foundation grant 1246045.

Chapter 3

ICE FABRIC INFERENCE WITH THIN-SECTION MEASUREMENTS AND SONIC VELOCITIES WITH APPLICATION TO THE NEEM ICE CORE

This manuscript will be submitted to The Cryosphere Discussions soon, with co-authors Erin Pettit, Ed Waddington, Dan Kluskiewicz, and Maurine Montagnat. Dan Kluskiewicz, Erin Pettit, and others collected the sonic-velocity data. Maurine Montagnat gave us the fabric eigenvalues. I developed the model and wrote this manuscript.

Abstract: We explore methods of inferring crystal orientation fabric using sound waves in ice-core boreholes, in tandem with velocity data from ice-core thin sections. We pay particular attention to sonic-velocity data collected from the NEEM ice core. Thin-section fabric measurements have been the predominant way of inferring crystal fabric from boreholes. However, thin-section measurements suffer from sampling error, and do not provide a spatially continuous record of fabric. Sonic-velocity measurements in boreholes allow for spatially-continuous measurements of fabric, and largely eliminate sampling error. Unfortunately, fabric inference from sonic-velocity measurements suffer from error associated with the use of an imperfect sonic-velocity model (model error). In addition, the sonic tool used at NEEM suffered from error due to poor tool centering in the borehole. It also collected only P-wave velocities, which are sensitive only to the largest fabric eigenvalue. To address these difficulties, we introduce a method to combine sonic-velocity measurements with fabric measurements. We show that this new method suffers from significantly less sampling error than thin-section measurements alone, while greatly reducing model error and the effects of poor tool centering. In addition, this method provides a spatially-continuous record of all three fabric eigenvalues, even if only P-wave data are available. We apply this method to

fabric thin-section data and sonic-velocity data collected at NEEM, to produce a spatially continuous and accurate record of fabric.

3.1 Introduction

Ice is a highly viscoplastically anisotropic material, deforming most easily in shear parallel to the basal plane, orthogonal to the crystallographic c-axis. The distribution of c-axis orientations in a polycrystal is known as the orientation distribution function (ODF). The bulk strain rate of a polycrystal can vary by an order of magnitude, depending on the ODF [76]. The ODF is an antipodally-symmetric probability distribution on the sphere, giving the density of c-axes by orientation across the sphere. Commonly, ODFs are summarized by the second-order orientation tensor, which is the second moment $\mathbf{A}$ of the ODF. That is, it is the average of the outer product of the c-axis with itself, $\mathbf{c}\otimes\mathbf{c}$, taken over the ODF. Equivalently, the second-order orientation tensor is the covariance matrix of c-axis directions. An estimate $\tilde{\mathbf{A}}$ of the second-order orientation tensor can be found from a thin-section sample as,

$$\tilde{\mathbf{A}} = \sum_i \zeta_i \mathbf{c}_i \otimes \mathbf{c}_i, \tag{3.1}$$

where there are N grains $\mathbf{c}_i$ in the sample, with $i = 1, .., N$. Also, ζ_i is the area of grain i, where the areas are normalized such that the total area of the thin section is unity.

The eigenvalues λ_i of this tensor provide a measure of fabric concentration in each of the three corresponding eigenvectors, or fabric principal-directions. The largest eigenvalue, λ_3, is associated with the direction of the greatest c-axis concentration. The smallest, λ_1, is associated with the direction of least concentration. The middle eigenvalue, λ_2, is associated with the direction orthogonal to the other two. The eigenvalues sum to unity by construction. If $\lambda_3 \approx \lambda_2 \approx \lambda_1$, the fabric is isotropic. If $\lambda_3 \gg \lambda_2 \approx \lambda_1$, the ODF exhibits a single-maximum fabric, with a large concentration in one direction. If $\lambda_3 \approx \lambda_2 \gg \lambda_1$, then the concentration lies along a great circle orthogonal to the direction associated with λ_1. This is known as a girdle fabric.

If c-axis directions of a polycrystal are distributed uniformly across the sphere, the polycrystal has bulk isotropic viscosity. However, ice undergoing deformation develops a non-uniform ODF. C-axes tend to rotate towards the directions of principal compression due to lattice rotation during deformation [5]. This induces bulk anisotropic flow.

In ice sheets, ice crystals are usually somewhat randomly oriented at deposition, although preferred orientations have been observed in the firn column close to the surface (Placidi et al. [67], Durand et al. [27]). Vertical compression causes c-axes to rotate towards the vertical direction. Likewise, shear on horizontal planes develops vertical-maximum fabrics due to the combined pure shear and rotation. Near divides, horizontal extension in one direction, and compression along the other two axes often causes vertical girdle fabrics to develop [5].

In addition to strongly affecting ice flow, the ODF seems to be sensitive to climate at the time of deposition. Initial perturbations in fabric due to climate can persist into deep layers [49]. In thin sections from the NEEM core [61], there is an abrupt change in fabric corresponding to the Holocene boundary.

Orientation distribution functions are commonly estimated from ice thin sections taken from ice cores, typically consisting of several hundred grains. This provides a direct sample of the ODF from the section of ice, but suffers from sampling error. This sampling error can be especially severe due to the typically highly non-uniform distribution of grain sizes. Polycrystal properties are best weighted by area in the thin section [34]; if several large grains cover much of the thin-section area, the effective sample size can be much smaller than the number of sampled grains.

In addition to sampling error, thin-section samples have very limited spatial coverage, usually on the order of 100 cm^2. Thin-section samples are labor intensive and consume core ice. Due to this, thin-section samples are typically taken only on the order of every tens of meters. Therefore, thin-section samples cannot capture fabric variability at shorter length scales. In addition, if one is interested in fabric characteristics averaged over several cubic meters, rather than a single thin section, short length-scale fabric variability (on the scale of decimeters) introduces another source of error.

Bentley [12] first proposed sonic logging as a method of fabric measurement to ameliorate some of the difficulties of thin-section fabric measurements. In addition to being viscously anisotropic, ice is elastically anisotropic. Therefore, sonic velocities of individual ice crystals are dependent on grain orientation. The stiffness tensor of a polycrystal is dependent on the orientation of the constituent grains. Sonic velocity measurements holds several advantages over thin-section fabric measurements. Sonic logging tools can sample on the order of 3m^3 of ice [50], which nearly eliminates sampling error, and can reduce the influence of small-scale variability in fabric.

Unfortunately, inference of fabric from sonic velocities is not straightforward. Model error can be an issue. First, sonic velocity in ice is affected by pressure and temperature. P-wave velocity in ice changes by around $2.5\text{m s}^{-1}\text{K}^{-1}$ to $2.8\text{m s}^{-1}\text{K}^{-1}$, which is a significant issue in polythermal ice (e.g. Helgerud et al. [44], Vogt et al. [79]). This can cause differences in velocity on the order of 100m s^{-1} in ice sheets [42]. Effects of temperature and pressure can be corrected, but significant uncertainties may still remain.

Recently, Maurel et al. [57] developed analytical expressions for the elasticity tensors and sonic velocities of ice for several ODF types. These included single-maximum fabrics with c-axis density distributed uniformly within a given zenith angle from vertical. In addition, they found solutions for idealized thick girdle and partial girdle fabrics. These relations have since been applied by Smith et al. [71] to infer crystal fabric in the Rutford ice stream using shear-wave splitting of seismic signals.

In this paper we outline a statistical model to infer fabric from sonic velocities using the Google Tensorflow automatic differentiation library [1]. In contrast to Maurel et al. [57], we model sonic velocities numerically using a flexible discrete ODF. This trades analyticity for greater accuracy in ODF approximation.

We apply this technique to combine pseudo P-wave and thin-section measurements taken from the NEEM ice core to find spatially continuous and more accurate fabric estimates. Unfortunately, the data collected from the NEEM core suffers from large velocity drift due to poor tool centering in the borehole. In addition, model error may be significant. To correct these errors, we incorporate thin-section measurements. While thin-section measurements lack spatial coverage, and have significant sampling error, they are unbiased (although correlated) samples of the actual crystal fabric. If the systematic velocity error (due to bias or model error) varies on length scales significantly larger than the spacing of the thin-section measurements, then the thin-section measurements can be used to estimate this error. In this way, we can combine the relative strengths of thin-section measurements (unbiasedness) and sonic-velocity measurements (spatial coverage, little sampling error), while reducing their weaknesses. We also test this technique on synthetic fabric data and sonic measurements, and show that it can effectively correct velocity drift and model error.

3.2 Velocity model for sound waves in ice

We now outline the forward velocity model used to estimate sonic velocity from ice fabric. Ice crystals exhibit anisotropic stiffness, dependent on c-axis direction. Bulk stiffness of ice anisotropic polycrystals is therefore anisotropic, dependent on the orientation of individual grains.

The bulk stiffness can be estimated using a volume-weighted average of the stiffness tensor across the polycrystal,

$$\bar{C}_{ijkl} = \int_{S_2} \psi(\mathbf{c}) C_{ijkl}(\mathbf{c}), \tag{3.2}$$

where ψ is the ODF giving the density of c-axes at orientation $\mathbf{c}$, and $C_{ijkl}(\mathbf{c})$ is the stiffness tensor of an individual ice grain, with c-axis aligned to $\mathbf{c}$ in the bulk coordinate system. Estimating bulk stiffness through volume-weighted stiffness assumes uniform strain throughout the polycrystal. The other end-member instead takes the harmonic mean of the stiffness tensor, which corresponds to a homogeneous-stress assumption. The truth is somewhere in between these two [45], although both produce similar predictions. Here, we assume uniform strain throughout the polycrystal, because it avoids numerical difficulties that occur with small elements of the stiffness tensor under the harmonic mean.

Sonic velocities can be derived from plane-wave solutions to the elastodynamic wave equation with zero forcing,

$$\left(\delta_{ij}\frac{d^2}{dt^2} - \rho^{-1}\bar{C}_{iklj}\frac{d^2}{dx_k dx_l}\right)u_j = 0, \tag{3.3}$$

where u_i is the material velocity of the polycrystal induced by the waves. Plane waves are waves of the form $u_i = f(k_i x_i - \omega t)\hat{u}_i$, where k_i is the propagation direction, $\hat{u}_i$ is the polarization direction, and ω is the phase velocity. The function f is a scalar function of one scalar argument. It may be a sine or cosine function, for example. Plugging the expression for a plane wave into the above equation, the function f cancels out, and it can be seen that admissible plane wave solutions are those where $\hat{u}_i$ and ω^2 are eigenvalue/eigenvector pairs of the Christoffel matrix [4], whose components are given by,

$$M_{ij} = \rho^{-1}C_{kijl}k_k k_l. \tag{3.4}$$

The Christoffel matrix is symmetric, because the stiffness tensor posesses symmetries such that $C_{kijl} = C_{jlki} = C_{ljik}$. The square roots of the three eigenvalues give the pseudo P-wave velocity v_p (the fastest), and the two pseudo-shear wave velocities, v_{sh} (the slowest) and v_{sv} (intermediate speed). Unlike waves in isotropic media, the pseudo P-wave polarization is not necessarily aligned with the propagation direction, and the shear waves are not necessarily polarized orthogonal to the propagation direction. However, the polarizations are orthogonal to one another because the Christoffel matrix is symmetric. Most observed fabrics in ice sheets have a principal direction associated with the highest c-axis concentration which is approximately vertical. Therefore, the pseudo P-wave velocity is typically polarized nearly vertical.

As an alternative to stiffness averaging and solving the resulting Christoffel equations, many authors have averaged the harmonic mean of sonic velocities (or the mean of the slowness) across the ODF, instead of the stiffness tensor. While simple and intuitive, this approach ignores mode conversion between P and S waves at grain boundaries [56].

We implemented this velocity model numerically by assuming that ice fabrics follow a discrete ODF, where the support (the domain where probability density is nonzero) of the distribution is confined to 900 “minimum energy” points $\mathbf{c}_i^{mep}$ [70], which are approximately uniformly distributed over the sphere. Since the ODF is antipodally symmetric, we consider only the points on the upper hemisphere. The distribution is parameterized by unconstrained weights for each point, w_i. In order for the distribution to add up to unity, the probability measure at each point is given by,

$$\psi(\mathbf{c}_i^{mep}) = \frac{\exp(w_i)}{\sum_j \exp(w_j)} \tag{3.5}$$

This is known as softmax normalization (e.g. Bouchard [14]). This distribution, which in this paper we will refer to as the discrete approximating distribution, has many more parameters than a typical PODF. However, over-fitting can be avoided by introducing a quadratic regularization penalty, similar to Tikhonov regularization. This is a very convenient distribution to fit fabric eigenvalues and sonic velocities. The vast majority of PODFs do not have analytical solutions for sonic velocities or eigenvalues in terms of their parameters. Thus, these quantities usually need to be calculated by quadrature on the sphere. With this distribution, we are “cutting out the middleman” by assuming beforehand that the distribution is supported only on the quadrature points.

To find the bulk stiffness, we rotate the stiffness tensor (Equation 3.2) such that the vertical axis of the transformed coordinate system is aligned with the c-axis of the quadrature point point $\mathbf{c}_i^{mep}$. This rotation is non-unique, since we assume that stiffness is invariant under rotations about the c-axis (in other words, we are not attempting to measure a-axes). We choose to rotate about the unique axis orthogonal to both $\mathbf{c}_i^{mep}$ and the vertical direction in the global reference frame. Then, the bulk stiffness tensor is constructed by taking the sum of the stiffness tensors for each point $\mathbf{c}_i^{mep}$, weighted by the discrete approximating distribution (Equation 3.5).

3.3 Fabric inference model

Fabric thin-sections provide a limited sample from the fabric ODF from where the sample was taken. As discussed above, inference of the larger-scale ODF can have substantial error from both sampling error and spatial nonstationarity of the ODF. Sonic measurements, on the other hand, sample a large volume of ice, leading to extremely small sampling error. In addition, the effects of sub-meter-scale spatial variability are significantly reduced. In the NEEM core, only P-wave velocities were collected, which are not sensitive to azimuthal fabric concentrations. In addition, the sonic data for the NEEM ice core have substantial error varying slowly over longer length-scales, which we will refer to as drift. This contrasts to the thin-section error, which is predominantly white noise stemming from sampling error or short length-scale variability in the ODF. The thin-section measurements have less total error when smoothing measurements over sufficiently long length-scales, but substantial error over short length scales.

In this section, we develop a model to combine thin-section and sonic-log estimates of fabric eigenvalues, while correcting for velocity drift and model error that varies smoothly with depth. We do this by fitting the discrete approximating distribution (Equation 3.5) at each depth, such that the modeled velocities derived from the discrete approximating fabric distribution fit the thin-section data and the observed velocities as closely as possible.

This procedure requires several steps, which can be summarized as follows: First, we use kriging [17] to fit the observed thin-section data. Next, at each depth, we fit the discrete approximating distribution (Equation 3.5) to the thin-section eigenvalues. Then, sonic velocities can be generated using the discrete approximating distribution, fitted to the thin-section eigenvalues. This yields modeled sonic velocities from the thin-section data alone. If significant velocity drift or smooth model error are present, there will be large, low-frequency mismatches between the modeled velocity and observed velocities. This mismatch is distinct from the higher-frequency mismatch due to thin-section sampling error or small-scale fabric variability. The smooth velocity mismatch is then regressed out using kriging to yield corrected velocities. Finally, the discrete approximating distribution is fitted to the corrected velocities and the thin-section eigenvalues simultaneously. This then yields eigenvalue estimates incorporating information from both sonic velocity and thin-section data.

To start with, we will use Gaussian-process regression [68], or kriging, to fit the observed thin-section data. A Gaussian process is a random function f whose values $\mathbf{y}_i = f(\mathbf{x}_i)$ at any finite number of points $\mathbf{x}_i$ follow a multivariate normal distribution. The covariance matrix between sets of points $\mathbf{X}$ and $\mathbf{X}^\star$ is $K(\mathbf{X}, \mathbf{X}^\star)$, where K is a positive-definite covariance function, or kernel, giving the covariance between two points as a function of their location. This induces a spatial structure in the Gaussian process. For example, a squared-exponential (or, Gaussian) kernel is often used. Here, K is set to, $K(\mathbf{X}, \mathbf{X}^\star) = k \exp(-b||\mathbf{X} - \mathbf{X}^\star||^2)$, where b is a constant giving the bandwidth of the Gaussian, and k is a scaling parameter. This favors smooth functions, because the correlation of nearby points is unity to first order. Gaussian white noise is also a Gaussian process, whose covariance function is $K(\mathbf{x}, \mathbf{x}^\star) = a$ if $\mathbf{x} = \mathbf{x}^\star$, and zero otherwise. This indicates that the values at different points are uncorrelated but the value at a given point follows a univariate normal distribution.

Rather than working with eigenvalues directly, we instead fit the η_i:

$$\eta_i = \operatorname{logit}(\lambda_i) = \log(\lambda_i) - \log(\lambda_3). \tag{3.6}$$

While the fabric eigenvalues are constrained to sum to unity, the logit eigenvalues η_i can take on any value. This makes the logits much easier to work with because the sum constraint is removed. The corresponding inverse softmax transformation squashes the logits back such that they sum to unity:

$$\lambda_i = \operatorname{softmax}(\eta_i) = \frac{\exp(\eta_i)}{\sum_j \exp(\eta_j)}. \tag{3.7}$$

We assume that each of the observed logit-transformed eigenvalues $\boldsymbol{\eta}_i$ are drawn from a realization of a Gaussian process, whose prior covariance is given by the sum of an exponential covariance function, $\exp(-a||\mathbf{x}_i - \mathbf{x}_j||)$, and a white noise covariance function. The exponential kernel allows for discontinuous functions, because the nearby points are not perfectly correlated to first order (as is the case with the squared-exponential kernel). This is a more realistic covariance function than the squared-exponential covariance function, since observed fabric eigenvalues do seem to change abruptly with depth. From this, the predictive mean of the logit eigenvalues at a depth d', conditioned on the observed logit eigenvalues $\boldsymbol{\eta}^{ts}$

at depths $\mathbf{d}^{ts}$, is given by,

$$\bar{\eta}_i(d') = \mathbf{K}(d', \mathbf{d}'^{ts})\mathbf{K}^{-1}(\mathbf{d}^{ts}, \mathbf{d}^{ts})\boldsymbol{\eta}_i^{ts}, \tag{3.8}$$

The predictive variance of the the estimated logit eigenvalue η_i at depth d' is,

$$\mathrm{Var}(d') = \mathbf{K}(d') - \mathbf{K}(d', \mathbf{d}^{ts})\mathbf{K}^{-1}(\mathbf{d}^{ts}, \mathbf{d}^{ts})\mathbf{K}(\mathbf{d}^{ts}, d') \tag{3.9}$$

This mean and variance defines a normal distribution for the logit eigenvalues η_i at each depth. From this, at each depth d' we can fit the discrete approximating distribution (Equation 3.5) to these eigenvalues. This is done by minimizing the squared error between the predicted mean of η_i at depth d', given by Equation (3.8), and the calculated fabric eigenvalues from the discrete approximating distribution (Equation 3.5). This is given by the eigenvalues of the estimated second-order orientation tensor $\hat{\mathbf{A}}$ of the discrete approximating distribution (Equation 3.5):

$$\hat{\mathbf{A}} = \sum_{\mathbf{c} \in M} \mathbf{c}\mathbf{c}^T \psi(\mathbf{c}), \tag{3.10}$$

where M is the set of minimum-energy points. If we assume that the fabric has a principal direction oriented nearly vertical, then the estimated eigenvalues λ_i are given by the diagonal elements $\hat{A}_{ii}$ (no sum) to first order.

From this, at each depth we have fitted the discrete approximating distribution to the observed thin-section data, but not the observed velocities. We then calculate modeled sonic velocities, given the thin-section data. The calculated sonic velocities do not suffer from the drift of the observed sonic velocities, and are approximately correct on longer length scales, unlike the observed sonic velocities. However, due to the usually low spatial coverage of thin sections, the calculated sonic velocities do not detect the meter-scale features of fabric that the sonic-velocity measurements can (since the velocity measurements are taken nearly continuously with depth). We approximately correct this mismatch by using Gaussian-process regression to estimate the mismatch under the assumption that it is smooth. This will not remove the non-smooth, higher-frequency components of the velocity mismatch, which can instead be expected to correspond to actual short length-scale fabric variability, which is not captured by thin-section measurements. For each velocity v_i (either v_{sh}, v_{sv}, or v_p) the mismatch at a depth d' is,

$$\epsilon_i(d') = v_i^{ts}(d') - v_i^{obs}(d'), \tag{3.11}$$

where $v_i^{obs}(d')$ is the observed velocity at depth d', and $v_i^{ts}(d')$ is the modeled velocity from the thin-section data. Here, we take the covariance function to be a sum of a squared-exponential covariance function, and white noise. This is given by,

$$\mathbf{K}_{\epsilon_i}(d, d') = k^{\epsilon_i} \exp(-a^{\epsilon_i}||d - d'||^2) + \sigma_{\epsilon_i}^2 I(d - d'), \tag{3.12}$$

where k^{ϵ_i} and $\sigma_{\epsilon_i}^2$ are scaling parameters, and a^{ϵ_i} is the bandwidth. I is a function where $I(0) = 1$, and $I(z) = 0$ for $z \neq 0$. This covariance produces smooth predictions, encoding a belief that the velocity drift is smooth. Similar to the Gaussian-process regression of the logit-transformed eigenvalues, the predicted mean of the the velocity mismatch is,

$$\bar{\epsilon}_i(d') = \mathbf{K}_{\epsilon_i}(d', \mathbf{d}^{ts})\mathbf{K}_{\epsilon_i}^{-1}(\mathbf{d}^{ts}, \mathbf{d}^{ts})\boldsymbol{\epsilon}_i^{ts}. \tag{3.13}$$

The modeled velocity is found from Equation (3.4). This then gives us the corrected velocities, with mean $\bar{v}_i^{corr} = v_i^{obs} + \bar{\epsilon}_i^{vel}$. Finally, at each depth d', we simultaneously fit the discrete approximating distribution to the corrected velocities (Equation 3.13) and the inferred thin-section logit-transformed eigenvalues $\bar{\eta}_i(d')$ (Equation 3.8). This is done by minimizing the following quantity with respect to the weights $\mathbf{w}$ of the discrete approximating distribution at each depth of interest,

$$\begin{aligned} J(\mathbf{w}) =& \sigma_{sh}^{-2}(\hat{v}_{sh}(\mathbf{w}) - v_{sh}^{corr})^2 + \sigma_{sv}^{-2}(\hat{v}_{sv}(\mathbf{w}) - v_{sv}^{corr})^2 + \\ & \sigma_p^{-2}(\hat{v}_p(\mathbf{w}) - v_p^{corr})^2 + \sigma_{\eta_1}^{-2}(\hat{\eta}_1(\mathbf{w}) - \bar{\eta}_1)^2 + \\ & \sigma_{\eta_2}^{-2}(\hat{\eta}_2(\mathbf{w}) - \bar{\eta}_2)^2 + \sigma_{\eta_3}^{-2}(\hat{\eta}_3(\mathbf{w}) - \bar{\eta}_3)^2 + \alpha||\mathbf{w}||^2. \end{aligned} \tag{3.14}$$

Here, σ_{sh}^2 is the variance of the velocity estimation, given by the sum of the variance of the velocity-correction term and the variance of the sonic-velocity measurements. The quantities σ_{sv} and σ_p are defined similarly. The quantity $\sigma_{\eta_i}^2$ is the variance of the posterior Gaussian process estimation of the logit-transformed fabric eigenvalue $\hat{\eta}_i$, given by Equation 3.9. The last term $\alpha||w||^2$ is a regularization term, equivalent to putting a zero-mean Gaussian prior on the weights $\mathbf{w}$. This regularization term serves only to ensure that a unique minimum exists for the objective function (3.14), rather than representing any kind of prior knowledge. The term is small enough that any fabric eigenvalues can be fit almost exactly. We minimized J with respect to $\mathbf{w}$ using Adagrad gradient descent [23], with the gradients derived using the Google Tensorflow automatic differentiation package [1].

Note that the objective function (3.14) is optimized independently at each depth of interest. We do not assume any kind of prior knowledge of smoothness with depth for this objective function. Sonic data collected from sonic tools are best averaged over a length-scale similar to the distance between the two sonic receivers. This accounts for short length-scale spatial correlations. There is no reason to assume a that fabric over longer length-scales is significantly correlated, since fabrics do indeed vary significantly over short length-scales. Assuming smoothness over longer length-scales would not allow for such short length-scale variability.

3.4 Eigenvalue inference on synthetic data

We now evaluate the statistical model developed in the previous section on synthetic fabric data. We generated "true" fabric eigenvalues for a 3000m deep borehole by assuming that the logit-transformed eigenvalues are sampled from a Gaussian process with an exponential covariance function, to yield eigenvalues that are discontinuous with depth. We then generate "true" v_p, v_{sh}, and v_{sv} velocities from these eigenvalues. We then add a smooth velocity corruption to these velocities (corresponding to model error and velocity drift), to yield synthetic corrupted velocities. The velocity corruption is the same absolute value for v_{sh}, v_{sv} and v_p. However, we do not use this knowledge in fitting the model. Instead we fit a separate correction for each velocity. Synthetic thin-section samples were generated every 30m by adding noise averaging 0.2 to the logit-transformed eigenvalues at each depth, with 100 thin sections in total.

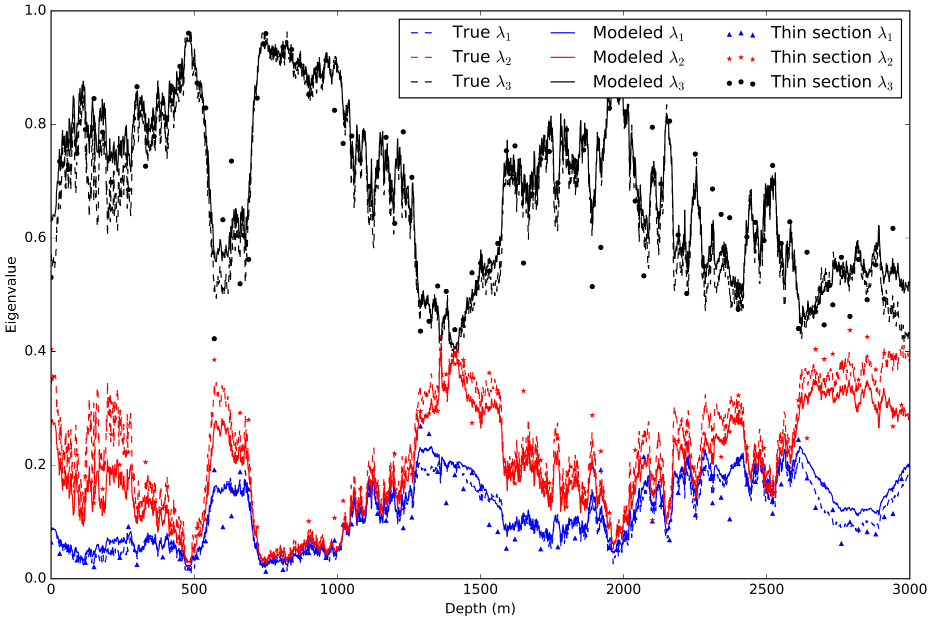

Figure 3.1: Application of the statistical model to synthetically generated fabric. Thin-section eigenvalues with 30m spacing are generated by adding noise to the true eigenvalues. The modeled eigenvalues are close to the true eigenvalues over the majority of the depth. Error is primarily due to error in the velocity-correction term.

The results are plotted in Figure 3.1. Over the majority of the core, the true fabric eigenvalues are approximated accurately. In a few spots, larger errors occur due to mis-estimation of the velocity corruption. The estimated velocity corrections and the true velocity corruption are plotted in Figure 3.2. Typical errors are on the order of 10ms^{-1}.

Note that we do not add white noise to the synthetic velocity data, which would correspond to sonic velocity measurement error uncorrelated with depth. We expect that uncertainties in arrival times are the primary cause of non depth-correlated velocity errors. With velocities averaged over several runs, and smoothed over a few meters, this error would typically be small in comparison to the depth-correlated errors of model error and velocity drift.

This is a challenging synthetic dataset, with large high-frequency spatial variability in eigenvalues. With only 100 noisy thin-section measurements, it can be difficult to separate the effects of the velocity corruption from actual variability in fabric eigenvalues. More thin sections, or less fabric variability can reduce this substantially.

3.5 Application to sonic measurements at NEEM

In this section, we apply the statistical model to P-wave velocity data and thin-section data collected at NEEM [61]. Unlike the case with synthetic data, only P-wave velocities were collected. The P-wave velocity constrains only the concentration of c-axes in the vertical direction (associated with the largest fabric eigenvalue λ_3). However, due to the sum constraint of eigenvalues, this still provides information on the sum of λ_1 and λ_2. The data were collected with a Mount Sopris CLP-4877 sonic-logging tool, modified to have a larger receiver spacing. The tool emits a monopole impulse source, which travels through the borehole fluid, through the ice, and back through the borehole fluid to two recievers, spaced at 90cm and 303.5cm from the source. Pulses are emitted every 2μs.

Three separate sonic logs were completed, with several sonic measurements taken every meter. Since the tool itself is roughly 3m long, spatial variability in sonic velocities shorter than 3m are difficult to interpret. Thus, in our analysis, we take 3m moving averages of the

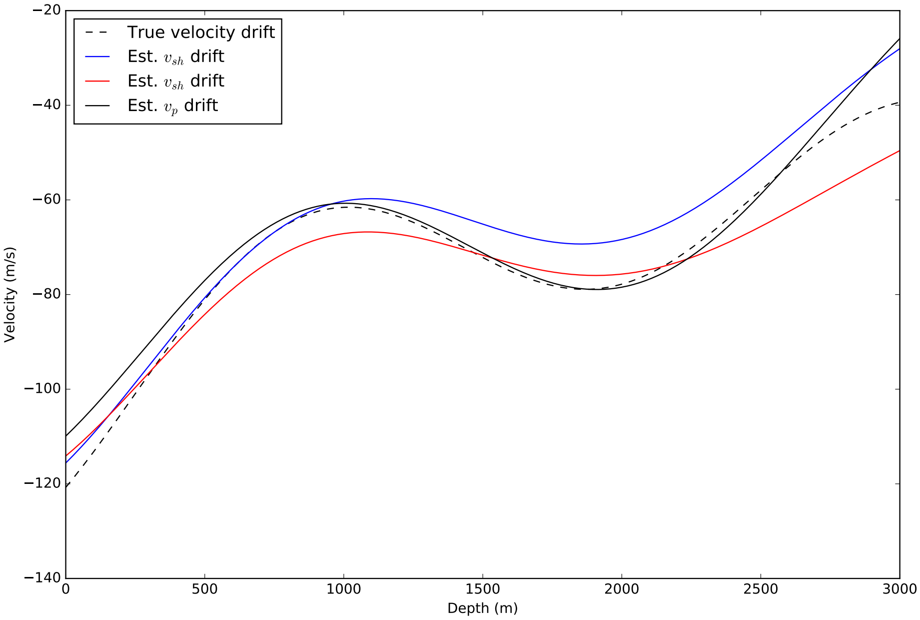

Figure 3.2: Velocity corruption (dashed) and estimated velocity corrections (solid lines) for v_p, v_{sh}, and v_{sv}. Estimation of the velocity corruption depends on the thin-section eigenvalues. Due to the large degree of spatial variability of the fabric, and the noise in the thin sections, inaccuracies on the order of 10m/s occur. More thin-section samples, and more accurate samples, can reduce this error substantially.

data. This also serves to significantly reduce uncorrelated measurement error, reducing error in measured v_p due to uncertainties in arrival times to the order of 1mi s^{-1} over multiple runs [50].

As discussed previously, large velocity drift occurs due to poor tool centralization in the borehole. This can differ between runs of the logging tool. However, short length-scale features are consistent between between runs.

We use the thin-section data from Montagnat et al. [61]. There are 271 thin sections, taken from 34m to 2461m. At some depths, multiple thin sections are taken. This gives a rough indicaton of the sampling error of the thin sections at those depths. We apply the model only below 250m. Above this depth, the velocity model becomes increasingly inaccurate. We expect this is due to a higher concentrations of air bubbles in the ice.

In Figure 3.3, we plot the modeled P-wave velocities from NEEM thin sections, and the collected P-wave velocities. There is a significant mismatch, with the collected P-wave data typically being on the order of 100m s^{-1} less than the modeled P-wave velocities. The lower-frequency part of this mismatch is due to some combination of model error and velocity drift. We expect both to be smooth, as the assumptions of the statistical model require. In addition to these smooth errors, the velocities derived from thin sections have significant uncertainties due to sampling error.

In Figure 3.4, we plot the eigenvalues derived from thin sections along with eigenvalues estimated using both thin-section data and the collected P-wave velocity. The largest eignvalue λ_3 increases almost linearly in the first 1300m of the core. Below about 2000m, the modeled eigenvalues begin to display large, high-frequency spikes. This may be due to differing amounts of recrystallization between layers. Layers experiencing greater amounts of recrystallization tend to have weaker fabrics. These fabric contrasts may also help initiate flow disturbances near the bed.

Applied to the NEEM ice-core data, we believe this model produces very accurate predictions of the largest eigenvalue, λ_3. Other eigenvalues are not informed by the P-wave velocity, except due to the eigenvalue sum constraint. While the P-wave data provide information on

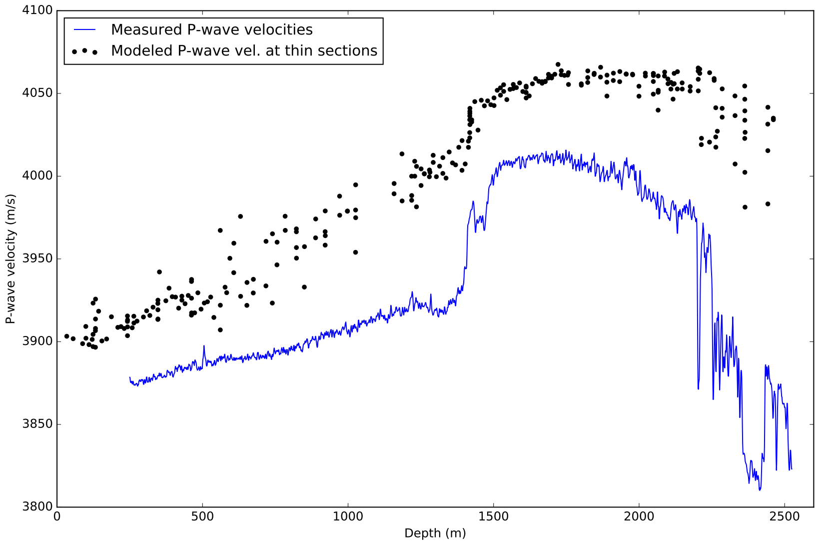

Figure 3.3: P-wave velocities modeled from thin sections (dots) and observed P-wave velocities (line). The observed P-wave velocities are smoothed over 3m and are averaged over multiple runs. Due to a combination of model error and velocity drift, the observed velocities are on the order of 100m s^{-1} less than the modeled velocities.

the sum of λ_1 and λ_2, it does not inform the difference between the two.

There are more thin sections, and much less large spatial variability in the NEEM core compared to the test on synthetic fabric. Thus, we expect the estimation of the velocity-correction term in the model to be more accurate, resulting in more accurate predictions of the largest eigenvalue λ_3 compared to the results for the synthetic data. Error in thin sections in estimating the eigenvalues of the bulk fabric (in volumes sampled by the sonic tool) is on the order of 0.1 over most of the core, increasing in the recrystallized deep layers. These errors correspond to larger uncertainties in ice viscosity, due to the power-law rheology of ice.

3.6 Conclusions

We showed P-wave velocity data collected from the NEEM ice core with a borehole sonic-logging tool. The collected P-wave velocities provide a high-quality continuous record of

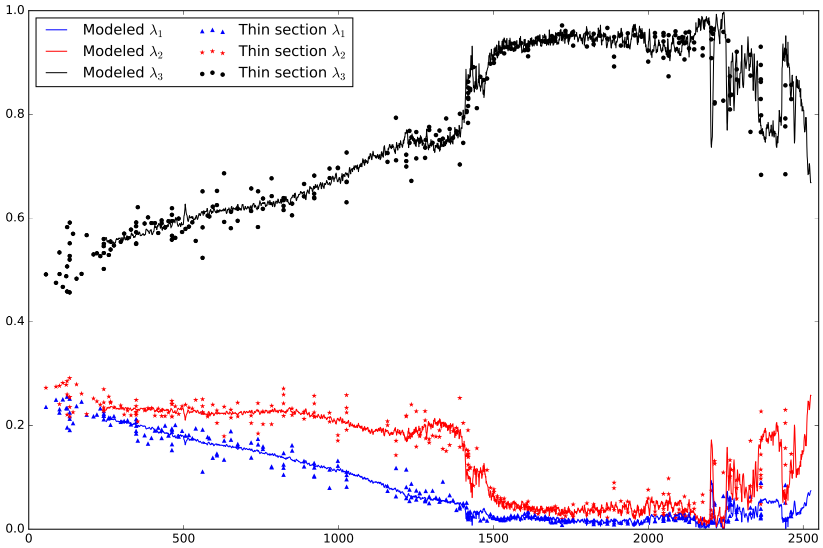

Figure 3.4: Eigenvalues derived from thin sections at NEEM (dots) [61], together with spatially-continuous estimates from the assimilation procedure. The variability of eigenvalues over shorter length scales in the upper core appears to be due to sampling error. The large variations seen in the thin sections in the deep ice are confirmed by the sonic velocity data.

fabric over depth at scales longer than 2m. However, they are subject to smoothly-varying errors.

We derived a method of incorporating thin-section data and sonic-velocity data in order to gain a more accurate, and spatially continuous picture of the ODF. This is especially important for understanding stratigraphic disruption that occurs near the bed of NEEM and other cores. The inferred fabric from the NEEM core shows variability in fabric on the order of several meters. This may trigger or enhance stratigraphic disruption. Fabric variability on these length scales is impossible to observe with thin sections taken only every several meters, with large sampling error.

This work demonstrates the utility of combining different methods of ODF measurements. Future work measuring S-wave velocities will greatly enhance the capabilities of sonic-velocity measurements in ODF determination. Improved sonic tools could reduce velocity measurement error and bias. However, we still expect that thin-section measurements are a useful adjunct to provide a mostly unbiased ground-truth for ice-sheet fabric to correct velocity-model error.

Chapter 4

THE RESPONSE OF ICE-CRYSTAL ORIENTATION FABRIC TO VELOCITY-GRADIENT PERTURBATIONS

This chapter is under review at the Journal of Glaciology. Ed Waddington is a co-author. I developed the analytical and numerical models, and wrote this manuscript.

Abstract: The distribution of crystal orientations of ice grains (the crystal fabric) of a polycrystal has a strong influence on the flow of polycrystalline ice, due to the plastic anisotropy of the individual grains. The fabric is in turn affected by ice flow. Flow on ice-sheet flanks is dominated by shear on horizontal planes, and divide flow is dominated by longitudinal extension. However, other velocity gradient components may also exist due to bed topography, variability in fabric or grain size, or other factors. This can in turn result in a fabric that differs from the fabric that would occur without any such flow disturbances. Indeed, disturbed stratigraphy is commonly observed near the bed of ice sheets. In this paper, we treat these flow disturbances as random but correlated in time, and determine their effects on crystal fabric. These small deviations in velocity gradient from pure shear or simple shear can induce the development of single-maximum fabrics with off-vertical directions of maximum c-axis concentration. In turn, this has the potential to induce stratigraphic distortion.

4.1 Introduction

An individual ice crystal deforms most easily in shear parallel to the crystal basal plane, orthogonal to the crystallographic c-axis. Deformation on planes in other orientations is on the order of 10 to 100 times harder. Plastic deformation of an ice polycrystal depends on the orientations of its constituent grains (e.g. Azuma [8]), which is described by the c-axis

Table 4.1: List of symbols

Symbol	**Definition**
q_i	Component of a tensor in index notation
$\boldsymbol{q}$	Same tensor in vector notation
$\boldsymbol{c}$	Ice-crystal c-axis vector
$\psi(\boldsymbol{c})$	Ice-crystal orientation dist. func.
$< q_i >$	Expected value of q_i under ψ
a_{ij}	Component of the structure-tensor $c_i c_j$
A_{ij}	Comp. of the 2^{th} order orient. tensor $< a_{ij} >$
$\mathbb{A}_{ijkl}$	Comp. of the 4^{th} order orient. tensor $< a_{ij} a_{kl} >$
λ_k	A fabric eigenvalue of $\boldsymbol{A}$
$\boldsymbol{\Xi}$	Matrix of eigenvectors of $\boldsymbol{A}$
$\boldsymbol{V}$	Vorticity, or spin, tensor
$\boldsymbol{D}$	Strain-rate tensor
δ_{ij}	Kronecker delta symbol
$\boldsymbol{S}$	Stress tensor
ϵ	A small parameter
$\lvert\lvert\boldsymbol{v}\rvert\rvert$	Vector magnitude of $\boldsymbol{v}$, $\sqrt{\boldsymbol{v}^T \boldsymbol{v}}$

orientation distribution function (ODF). The ODF is a probability distribution of c-axis density often defined on the upper hemisphere (because a c-axis vector $\mathbf{c}$ is indistinguishable from $-\mathbf{c}$). In this paper, we will instead treat the ODF as an even function defined on the entire sphere for mathematical convenience. A polycrystal with an isotropic ODF will have a bulk isotropic response to applied stress. However, polycrystals develop an anisotropic ODF in response to applied strain.

The development of a preferred orientation is guided primarily by intracrystalline slip. There is a tendency for the c-axes to rotate away from the directions of principal extensional strain due to lattice rotation [10]. ODFs are often summarized using orientation (or, moment) tensors (e.g. Svendsem and Hutter [73]), where the n$^{\text{th}}$ order moment tensor is the n$^{\text{th}}$ order moment of the ODF. Throughout this paper, the indices 1, 2, and 3 will be associated with the x-, y-, and z-directions, respectively. Fabric is usually described using only the second-order orientation tensor $\boldsymbol{A}$. The component of the second-order orientation tensor A_{ij} is the expectation $< c_i c_j >$, where $i, j = 1, 2, 3$. The mean of the ODF (or the first-order orientation tensor in this terminology), $< c_i >$, is always zero because of antipodal symmetry (and likewise for any odd-order tensor). Therefore, A_{ij} is also a component of the covariance tensor of the distribution:

$$\begin{aligned} \mathrm{Cov}(c_i, c_j) &=< (c_i- < c_i >)(c_j- < c_j >) > \\ &=< (c_i - 0)(c_j - 0) > \\ &= A_{ij} \end{aligned} \tag{4.1}$$

The diagonal elements A_{11}, A_{22}, and A_{33} give a measure of the c-axis concentration on the x, y, and z axes, respectively. Similar to the second-order orientation tensor, the fourth-order tensor is the expected value $\mathbb{A}_{ijkl} =< c_i c_j c_k c_l >$. Since the second-order orientation tensor is symmetric, it is diagonal in the coordinate system defined by its eigenvectors, or fabric principal directions. The diagonal elements are the fabric eigenvalues λ_i. The eigenvalues sum to unity by construction. The three fabric principal directions denote the directions of greatest density (corresponding to the largest eigenvalue), smallest density (the smallest eigenvalue), and a direction orthogonal to the other two. An isotropic fabric has three equal eigenvalues. A girdle fabric (in which there is a band of high concentration along a great circle) has two nearly equal eigenvalues, and one small eigenvalue. A single-maximum fabric has one large eigenvalue, and two small eigenvalues.

If the evolution of the ODF is given by a partial differential equation (PDE) over the sphere, it is possible to derive an ordinary differential equation (ODE) for the evolution of A_{ij}. This is much easier than solving the PDE, whose solution at any given time is a function defined on the sphere, rather than just the six unique elements of the second-order orientation tensor. This substantially reduces computational difficulties. With this approach, Gillet-Chaulet et al. [38] used a Jefferys-type equation for A_{ij}, valid when the c-axes move by basal slip only. Their model works for arbitrary vorticity tensors and velocity gradients. Gödert [40] developed a similar model incorporating rotary diffusion into the evolution equation for A_{ij}. In this paper, we take a similar approach to Gillet-Chaulet et al. [38].

Fabric development during ice flow is likely a physically deterministic process. However, at any given site, there are uncertainties in strain history, impurity content, initial conditions at deposition, and other factors. We examine how these uncertainties may affect uncertainties in ice flow. Flow inhomogenities can result from numerous sources. On small scales, random variations in fabric strength can in turn induce spatial differences in flow. Near the bottom of the West Antarctic Ice Sheet (WAIS) divide core, some layers have experienced recrystallization, and have a weaker fabric compared to others that have not recrystallized [30]. Durand et al. [25] found an abrupt transition in the ice fabric at EPICA Dome C corresponding to Termination II, suggesting that climate at the time of initial deposition can play a prominent role in in the subsequent development ice fabric. Alley et al. [7] found evidence of "striping" in the GISP2 core, in which elongated areas of grains possessed off-vertical c-axes. In horizontal extension under divide flow, these stripes localize shear within them, and offset layers in the hard surrounding ice. This induces flow disturbances around stripes, as well as overturning stratigraphic layers. Jansen et al. [47] produced bands similar to observed stripes in strong single-maximum fabrics using the two-dimensional ELLE microstructure model. Regions where the fabric was tilted away from the bulk lattice-preferred orientation toward the direction of shear seeded the formation of the bands. On larger scales, flow disturbances can arise due to basal topography and transient flow, basal-ice accretion [11], or various other sources.

Thorsteinsson and Waddington [76] examined the development of low-angle wrinkles in stratigraphic layers in ice sheets. Under simple shear, low-angle wrinkles will steepen,

Figure 4.1: The six unique components of $\boldsymbol{A}$ for 3000 realizations of the Jeffery's-type equation (5.7) forced with pure shear and a strain perturbation whose components average 2% of the background pure shear, and $\gamma = 1$. The central 95% of realizations are shaded. Significant deviations of A_{13} and A_{23} occur. These correspond to tilted cone fabrics whose direction of greatest concentration differs on the order of 5° from vertical.

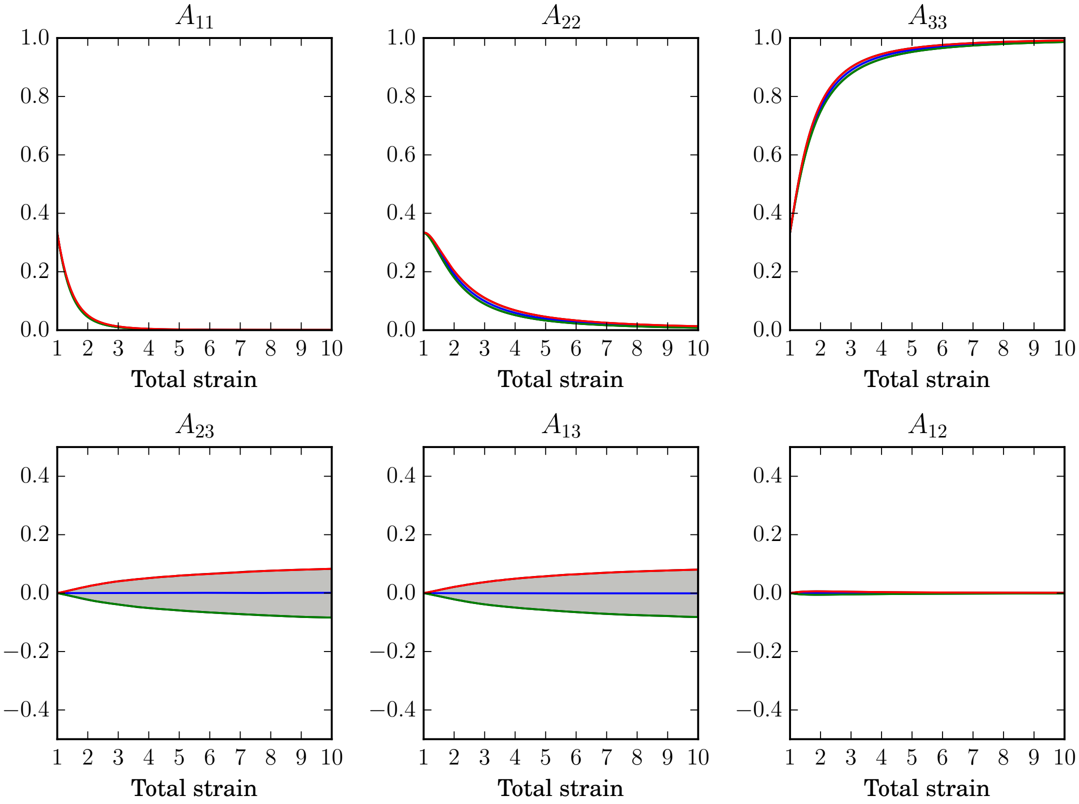

eventually producing overturned folds. Pure shear or vertical uniaxial compression produce the opposite effect, flattening out wrinkles. Near ice divides, simple shear is less prominent compared to pure shear. However, vertical single-maximum fabrics develop under both vertical compression and simple shear. These fabrics make the ice harder under vertical compression, and soft under horizontal simple shear. This may greatly aid the development of stratigraphic disruption in simple shear, because steepening of incipient folds is enhanced, while flattening is reduced.

In this paper, we analyze how small amounts of variability in the velocity gradient can affect crystal fabric. By "variability," we mean small components of the velocity gradient distinct from the dominant background flow (e.g., simple shear in flank flow). The goal is to see whether it is possible to develop large excursions in the ODF in response to small velocity-gradient perturbations. If, as a result of small excursions in the velocity gradient, large, spatially non-homogeneous differences in fabric can develop, they may seed further velocity gradient disturbances and stratigraphic disruption. We do not examine sources of such flow disturbances. Instead, we make the approximation that they are random, but correlated in time. That is, the perturbation at a certain time will be highly correlated to perturbations at sufficiently nearby times.

This paper is split into two main parts. In the first section, we develop a first-order approximation of the effects of a velocity-gradient perturbation on concentrated vertical single-maximum fabrics in flank flow (horizontal simple shear) and divide flow (pure shear). We show that in both cases, small perturbations of the velocity gradient can cause the fabric principal directions to rotate significantly, generating a fabric that would induce a vertical velocity perturbation in both flow situations. In the second section, we expand on the analytical result by numerically solving the Jeffery's-type equation for the evolution of A_{ij} (see next section) perturbed by a small random velocity gradient. We generate confidence intervals of the six unique components of A_{ij} by computing several thousand realizations. The results numerically confirm the analytical observations in the first section.

4.1.1 Fabric evolution

The most important process governing the development of crystal fabrics is deformation-induced grain rotation. If grain deformation is due solely to basal glide, the rate of change of the c-axis orientation is the sum of bulk rotation and viscoplastic spin. From Meyssonnier and Philip [58], the evolution of c-axis orientation in response to strain can be described by a modified Jeffery's equation [48]:

$$\dot{c}_i = V_{ij}c_j - D^g_{ij}c_j + c_ic_jc_kD^g_{jk}, \tag{4.2}$$

where c_i is the unit vector in the direction of the c-axis. The quantities V_{ij} and D^g_{ij} are components of the rotation-rate tensor, and local strain-rate tensor of the grain, respectively. The first term gives the rotation rate due to the bulk rotation of the polycrystal, while the second term gives the rotation rate due to viscoplastic spin. Thus, for example, the c-axis of a grain experiencing uniaxial compression will rotate towards the compressive direction. The last term of Jeffery's equation (5.2) ensures that the motion of grain orientation is tangent to the unit sphere at $\mathbf{c}$, which is necessary due to the convention that the c-axis vector is of unit length. This can be seen by noting that the $V_{ij}c_j$ term does not affect the magnitude of c_i, leaving only the $D_{ij}c_j$ term. Assume that at time $t = 0$, the c-axis is given by $\mathbf{c}_0$. After a short length of time δt, the magnitude of the new c-axis $\mathbf{c}_{\delta t}$ is (without the final term in Equation 5.2),

$$\begin{aligned} ||\mathbf{c}_{\delta t}|| &= ||\mathbf{c}_0 - \delta t\boldsymbol{D}\mathbf{c}|| & (4.3)\\ &\approx ||\mathbf{c}_0|| - \mathbf{c}_0^T\boldsymbol{D}\mathbf{c}_0\delta t & (4.4)\\ &= 1 - \mathbf{c}_0^T\boldsymbol{D}\mathbf{c}_0\delta t, & (4.5) \end{aligned}$$

to first order in δt. Thus, for the c-axis to maintain unit length, we must add the quantity $\mathbf{c}^T\boldsymbol{D}\mathbf{c}\delta t$ projected onto $\mathbf{c}$, by multiplying by $\mathbf{c}$. This then gives the last term of Equation (5.2). Rather than compute the rotation rate for each grain individually, we instead seek an evolution equation for the second-order orientation tensor whose components are given by

$A_{ij} =< c_i c_j >$. Differentiating with respect to time, we have,

$$\frac{dA_{ij}}{dt} =< \dot{c}_i c_j > + < c_i \dot{c}_j > . \tag{4.6}$$

This introduces the problem of homogenization. We must average out the quantity in the brackets over the entire ODF. However, $\dot{c}_i^k$, for some individual grain k, depends on the strain-rate tensor of that particular grain as can be seen in Equation (5.2). Thus, we need a tractable method for relating the bulk stress and strain to that of individual grains. The stress and strain of each individual grain should ideally be consistent with the bulk stress and strain rate. The two possible end-members are the Taylor-Bishop-Hill model [74], assuming homogeneous strain among grains, and the Sachs model [69], which assumes homogeneous stress among grains. Visco-plastic self-consistent (VPSC) homogenization methods [52] have been used for anisotropic ice-flow constitutive relations (e.g. Castelnau et al. [15], Gillet-Chaulet et al. [38]). VPSC schemes treat each individual grain as an ellipsoidal inclusion in a medium with the average properties of the polycrystal. This can provide a more accurate distribution of stress and strain within the polycrystal, with stress and strain both dependent on the orientation of a grain. Grain rotation due to lattice rotation can also be directly incorporated into VPSC schemes. However, VPSC schemes are typically computed iteratively over finite samples of grains, and are difficult to directly incorporate into Eq. (4.6).

As a compromise, Gillet-Chaulet et al. [37] took the strain on an individual grain as a weighted average between the homogeneous stress and homogeneous strain assumption. In this case, D_{ij}^g in Eq. 5.2 is,

$$D_{ij}^g = (1-\alpha)\bar{D}_{ij} + \alpha\frac{\varsigma \bar{S}_{ij}}{2}, \tag{4.7}$$

where $\bar{D}_{ij}$ is a component of the *bulk* strain-rate tensor, $\bar{S}_{ij}$ is a component of the bulk stress tensor, and ς is the fluidity for shear parallel to the basal plane. The weighting between homogeneous stress and homogeneous strain is given by the interaction parameter α. Setting $\alpha = 0$ gives the homogeneous strain rate assumption, while $\alpha = 1$ gives homogeneous stress. This parameter may be tuned to fit a VPSC model. In Gillet-Chaulet et al. [38] they used a value of $\alpha = 0.06$. Throughout this paper, we use the homogeneous strain assumption, with $\alpha = 0$. The homogeneous strain assumption for grain rotation produces fairly realistic predictions for fiber orientation, even though the homogeneous strain assumption produces rather poor predictions of ice flow. Given that Gillet-Chaulet et al. [38] found the best results with $\alpha = 0.06$, we are not too far off by setting $\alpha = 0$. Note that setting $\alpha \neq 0$ to yield a local grain strain rate equal to G_{ij} produces the same predictions as assuming homogeneous strain, and setting the bulk strain $\bar{D}_{ij} = G_{ij}$. For vertical single-maximum fabrics forced with simple shear or pure shear, as in this paper, D_{ij} and S_{ij} are proportional with dimensions of viscosity.

With this assumption, the derivative of the second-order orientation tensor $\boldsymbol{A}$ becomes,

$$\begin{aligned}\frac{dA_{ij}}{dt} =& V_{ik}A_{kj} - A_{ik}V_{kj} - D_{ik}A_{kj} - A_{ik}D_{kj} + \\ & 2\mathbb{A}_{ijkl}D_{kl}.\end{aligned} \tag{4.8}$$

The presence of the fourth-order orientation tensor $\mathbb{A}_{ijkl}$ in Eq. (5.7) introduces the closure problem. In general, $\mathbb{A}_{ijkl}$ cannot be found from $\boldsymbol{A}$. If we used an additional evolution equation for $\mathbb{A}_{ijkl}$, then the six-order orientation tensor would appear in that equation, and so on. Thus, we need some way of approximating $\mathbb{A}_{ijkl}$ in terms of $\boldsymbol{A}$. In this paper, we use the popular and simple quadratic closure, where $\mathbb{A}_{ijkl} = A_{ij}A_{kl}$ [3]. This closure is exact in the case of perfectly concentrated single-maximum fabrics, where $A_{ij} = \delta_{i3}\delta_{j3}$. It is quite accurate whenever $\lambda_3 > 0.8$ or so. In this paper, we are primarily intersted in the response of strong fabrics to velocity-gradient perturbations, so this is a good approximation for our purposes.

4.2 First-order perturbations to strong single-maximum fabrics

We now examine the analytic sensitivity of strong vertical-maximum fabrics to velocity-gradient perturbations. We show that fabrics are susceptible to developing “tilted cone” fabrics, in which the direction of greatest concentration is not vertical, in both horizontal pure shear and simple shear. Here we add a small perturbation $\epsilon\hat{A}_{ij}$ to the component of the second-order orientation tensor A_{ij}. The tensor $\hat{\boldsymbol{A}}$ has zero trace, and ϵ is small. Then,

Figure 4.2: The six unique components of $\boldsymbol{A}$ for 3000 realizations of the Jeffery's-type equation (5.7) forced with pure shear and a strain perturbation whose components average 5% of the background pure shear, with $\gamma = 1$. the central 95% of realizations are shaded. Larger deviations of A_{13} and A_{23} occur than under 2% average perturbations. These correspond to tilted cone fabrics tilted on the order of 10° from vertical. The background pure shear is very effective at restraining perturbations of other components of $\mathbf{A}$.

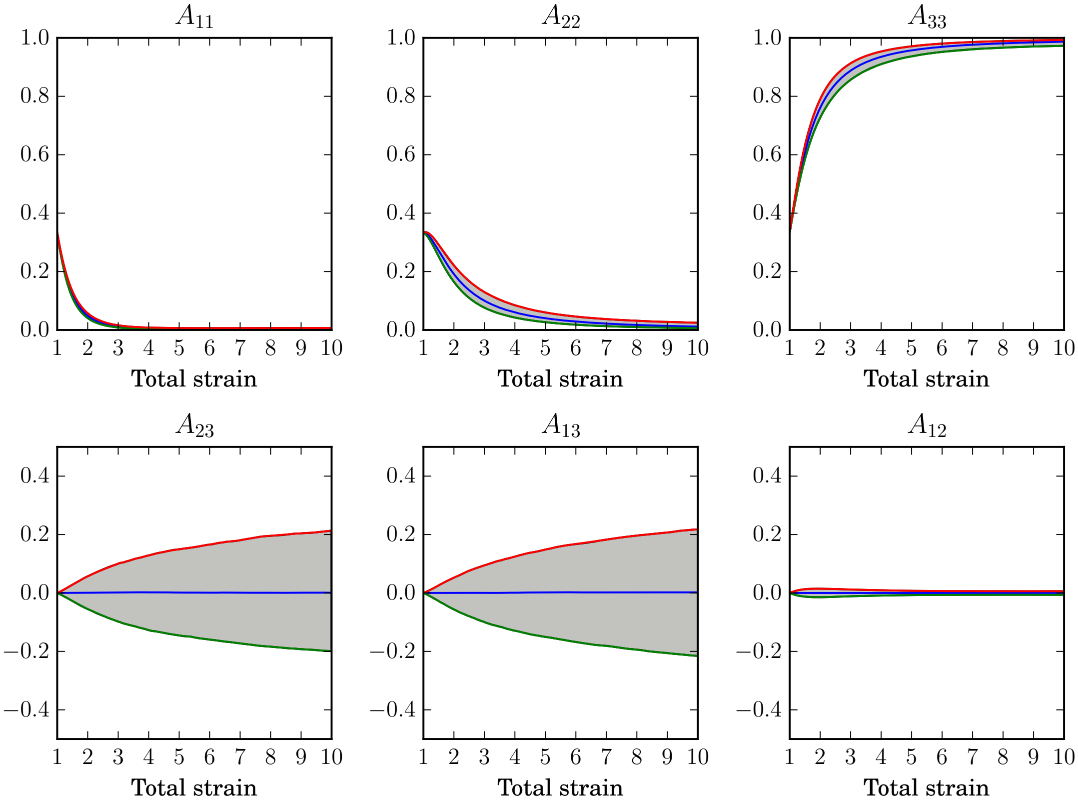

components of the perturbed second-order orientation tensor are given by $\tilde{A}_{ij} = A_{ij} + \epsilon \hat{A}_{ij}$.

Next, we also assume that the vorticity and strain rate are perturbed by small quantities $\epsilon\hat{\boldsymbol{V}}$ and $\epsilon\hat{\boldsymbol{D}}$, respectively. Then, we can substitute these quantities into Eq. (5.7), and discard quantities of $\mathcal{O}(\epsilon^2)$ and higher. This then gives us a first-order equation for the perturbed

As with the case of pure shear, the only components that are directly affected by velocity-gradient perturbations (to first order) are $\hat{A}_{13}$ and $\hat{A}_{23}$. The growth of the perturbation $\hat{A}_{13}$ to A_{13} is affected by $\hat{A}_{22}$. Depending on the signs of $\hat{D}_{13}$ and $\hat{V}_{13}$, it may be restrained or reinforced by $\hat{A}_{22}$. Similarly, other components depend on each other, to first order. For example, A_{11} depends negatively on A_{13}. However, we may expect that $\hat{A}_{13}$ and $\hat{A}_{23}$ will generally be the largest components of $\hat{\boldsymbol{A}}$ in magnitude. As long as their magnitudes are

Figure 4.3: The six unique components of $\boldsymbol{A}$ for 3000 realizations of the Jeffery's-type equation (5.7) forced with simple shear and a strain perturbation whose components average 2% of the background pure shear, with $\gamma = 1$. The central 95% of realizations are shaded. Smaller perturbations develop than with pure shear. However, they still may be enough to seed further fabric and flow disturbances.

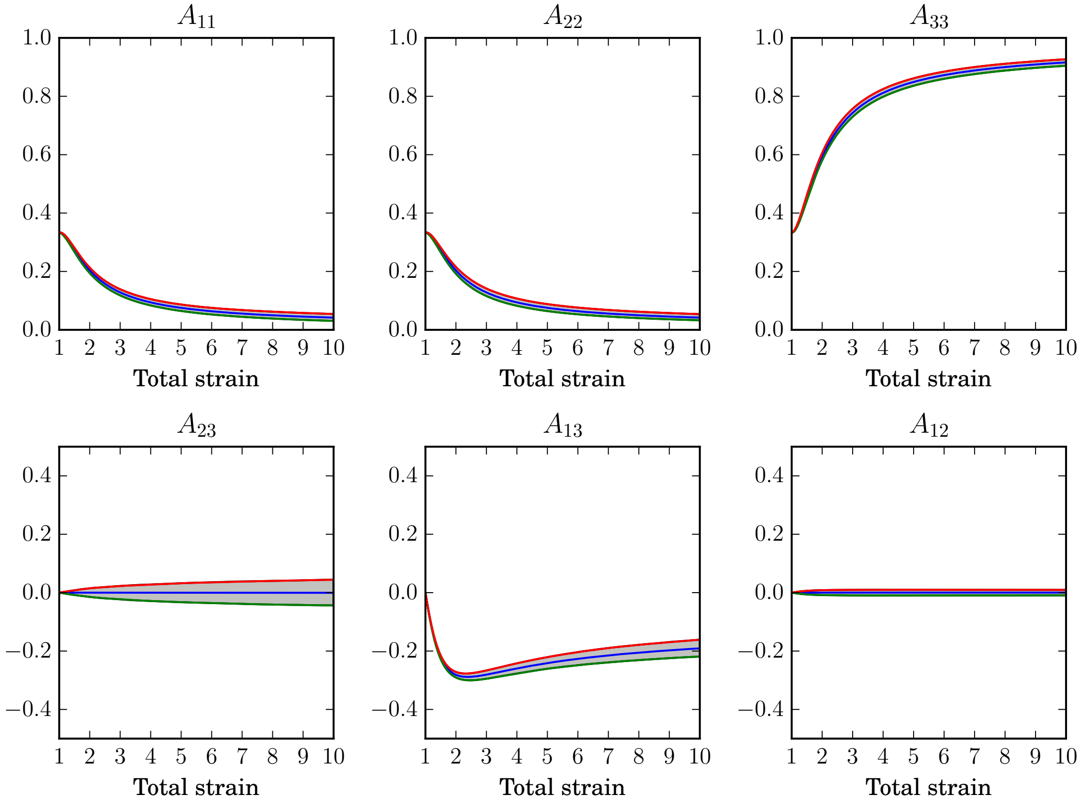

generally less than the applied velocity-gradient perturbations, perturbations to other components will grow more slowly. For example, if $|-2\hat{A}_{13}|$, the growth rate of the perturbation to A_{11}, is less than $|\hat{A}_{22} - D_{13} + W_{13}|$, the growth rate of $\hat{A}_{13}$, we can expect $\hat{A}_{13}$ to grow faster than $\hat{A}_{11}$. This intuition is confirmed numerically in the next section.

4.3 Monte-Carlo analysis of stress perturbations

We now expand on the sensitivity analysis of the previous section by considering numerical solutions to the Jeffery's equation (5.7) forced with background simple shear or pure shear in addition to a small random velocity gradient. This gives us an idea of the magnitude of fabric perturbations that we may expect in response to velocity-gradient perturbations. It also allows us to look at the effects of velocity-gradient perturbations away from equilibrium. In the previous section, we showed that background pure shear or simple shear is not effective at restraining perturbations of the A_{13} and A_{23} components of the second-order orientation tensor. Integrating the Jefferys equation (5.7) through time, we can expect the effects of velocity-gradient perturbations to be magnified, as integration acts as a low-pass filter.

First, we must have some way of generating velocity-gradient perturbations. It is reasonable to assume that a velocity-gradient perturbation at time t will be highly correlated to perturbations at $t + \epsilon$, if ϵ is small enough. To account for this, we construct the velocity-gradient perturbations using realizations of a Gaussian process. A Gaussian process is a random process (or function) $X(t)$ for which any finite sample $(X_{t_1}, X_{t_2}, ..., X_{t_k})$ from the process has a joint Gaussian distribution, determined by a covariance function $C(t_0, t_1)$ which gives the covariance $\text{Cov}(X_{t_0}, X_{t_1}) = C(t_0, t_1)$.

Let $\hat{U}^t_{ij}$ be a component of a realization of the perturbed velocity gradient at time t. To generate $\hat{U}^t_{ij}$, we first sample a realization $G^{t_k}_{ij}$ from the Gaussian process, for each discretized time t_k. Since the time is taken at a discrete number of points, this is just a sample from an ordinary multivariate normal distribution with a mean of zero whose covariance tensor has components given by $K_{ij} = C(t_i, t_j)$.

We assume that G^t_{ij} has a squared-exponential covariance function, $C(t, t') = \sigma^2 \exp(-\gamma(t-$

Figure 4.4: The six unique components of $\boldsymbol{A}$ for 3000 realizations of the Jeffery's-type equation (5.7) forced with simple shear and a strain perturbation whose components average 5% of the background pure shear, using $\gamma = 1$. The central 95% of realizations are shaded. Large deviations in A_{13} and A_{23} occur than with 2% average velocity-gradient perturbations, corresponding to tilted cone fabrics deviating on the order of 5° from vertical. Smaller deviations occur in other components.

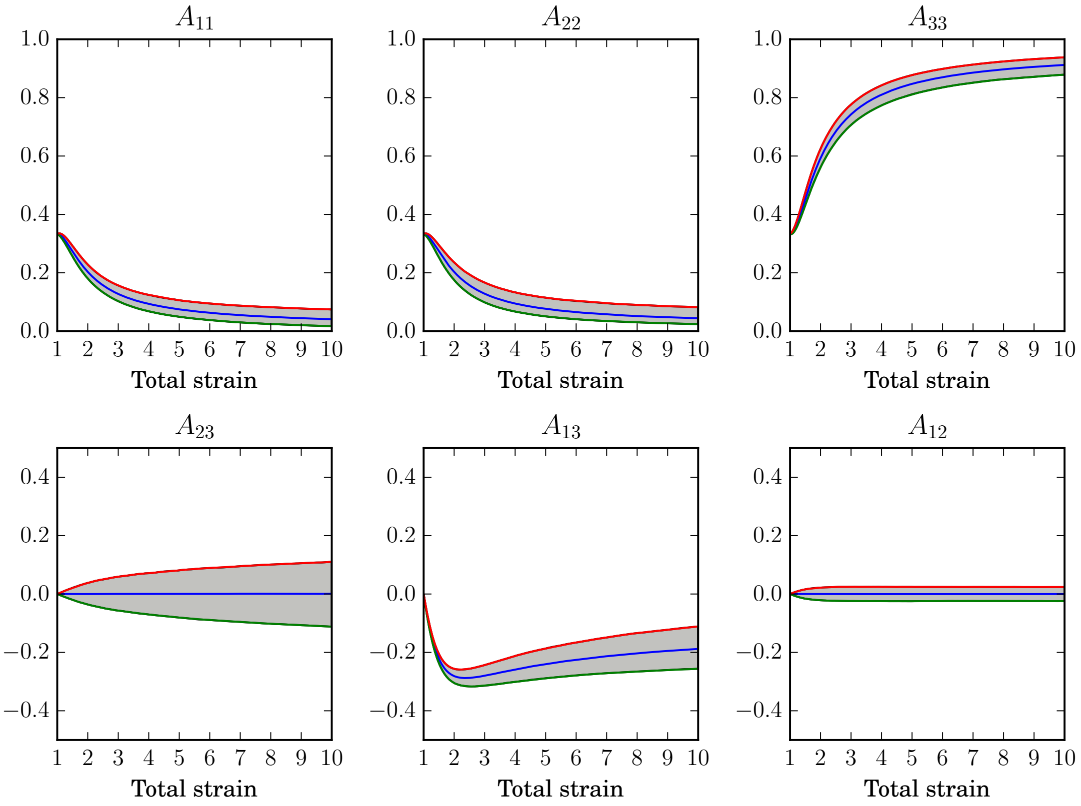

$t')^2)$. The parameter γ, where $\gamma \geq 0$, controls how closely nearby points are correlated. A small value of γ means that two different points are more highly correlated. Smaller values of γ will tend to promote larger fabric perturbations, since the higher degree of correlation over time will help prevent fabric perturbations from being cancelled out. The quantity σ^2 gives the variance of the perturbation at a single point. The tensor with components G^t_{ij} does not satisfy incompressibility. Incompressibility is recovered by subtracting one third of the trace from each component of the diagonal, yielding the velocity-gradient perturbation $\hat{U}^t_{ij}$.

We plot the central 95% interval of the six independent elements of the tensor $\boldsymbol{A}$ for 3000 realizations of velocity-gradient perturbations under pure shear for perturbations averaging 2% and 5% of background strain, in Figures 4.1 and 4.2, respectively. The model is run until reaching a total strain of 10, excluding the velocity-gradient perturbations. Time is nondimensionalized by the strain rate, such that the strain rate is unity. We set $\gamma = 1$, which means that velocity-gradient perturbations occuring at nondimensional times seperated by more than 2 are nearly uncorrelated. The initial fabric is taken to be isotropic, with $A_{11} = A_{22} = A_{33} = 1/3$. Consistent with the analytical results from the previous section, A_{13} and A_{23} have much greater differences between their 2.5% and 97.5% quantiles than other components. This corresponds to the development of a tilted cone fabric, with A_{13} being the Euler angle of rotation about the x-axis, to first order. Similarly, A_{23} is the Euler angle rotation of the fabric about the y-axis, to first order.

In Figures 4.3 and 4.4, we plot the same results for simple shear under 2% and 5% average velocity-gradient perturbations, respectively. Just like the case with pure shear, A_{13} and A_{23} have relatively large spreads between the 2.5% and 97.5% quantiles. Other components are perturbed to a lesser extent, but to a much greater degree than in the case of pure shear. This is most likely because the background simple shear does not restrain the growth of perturbations in any component, to first order.

4.4 Conclusions

Stratigraphic disruption in basal ice is a significant problem for the interpretation of ice-core records. The strong viscous anisotropy of ice may play a significant role in the development of stratigraphic disturbances (e.g. Azuma and Goto-Azuma [10], Thorsteinsson and Waddington [76]). We showed that ice-crystal orientation fabric is sensitive to velocity-gradient perturbations. In particular, even small velocity-gradient perturbations are capable of producing single-maximum fabrics whose axes of maximum c-axis concentration deviate significantly from vertical. Background pure shear or simple shear is not effective at restraining these perturbations. Such fabrics are capable of inducing layer overturning in response to pure shear (divide flow) or simple shear (flank flow).

There may be numerous sources for stratigraphic disruption in basal ice. The dynamics of basal ice can become very complicated in some settings due to basal freeze-on, recrystallization, and sliding. However, c-axis orientation fabric must always play a role, because any flow which can induce stratigraphic disruption will also affect fabric. We did not consider the coupling of flow and fabric evolution in this paper. Perturbations to fabric cause perturbations to flow, possibly inducing further fabric disturbances. Therefore, this analysis is only appropriate to help understand the onset of disturbances to crystal fabric in response to a velocity-gradient perturbation. More work is needed to understand the coupling of fabric development to ice flow, and other physical processes of basal ice.

Chapter 5

PERTURBATIONS OF FABRIC EVOLUTION AND FLOW OF ANISOTROPIC ICE

This chapter will be submitted to the Cryosphere Discussions soon. I wrote this manuscript and developed the model. Ed Waddington helped edit the manuscript.

Abstract: The distribution of crystal orientations of ice grains (the crystal fabric) of a polycrystal has a strong influence on polycrystalline ice-flow, due to the plastic anisotropy of the individual grains. In turn, crystal-orientation fabric evolution is guided primarily by deformation. This suggests that the coupled dynamics of flow and fabric may produce significantly different behavior than if they were uncoupled. We develop an analytical first-order perturbation model of coupled linear flow of anisotropic ice and fabric evolution. We analyze the development of several types of perturbations in different flow scenarios. The results show that fabric development coupled to flow of anisotropic ice is dynamically unstable in many flow scenarios. These instabilities may lead to the development of shear bands, boudinage, and other stratigraphic disturbances seen in ice sheets.

5.1 Introduction

An individual ice crystal has an anisotropic creep response, deforming most easily in shear parallel to the crystal basal-plane, orthogonal to the crystallographic c-axis. Plastic deformation of an ice polycrystal depends on the orientations of its constituent grains (e.g. Azuma [8]), which is described by the c-axis orientation distribution function (ODF). The ODF is a probability distribution of c-axis density often defined on the upper hemisphere (because a c-axis vector $\mathbf{c}$ is indistinguishable from $-\mathbf{c}$). In this paper, we will instead treat the ODF as being defined on the entire sphere for mathematical convenience. A polycrystal with an isotropic ODF will have a bulk isotropic response to applied stress. However, polycrystals develop an anisotropic ODF in response to applied strain. Grains tend to rotate towards the axes of principal compression. This produces a bulk anisotropic response to stress. In flank flow in ice sheets, c-axes typically cluster near vertical. This puts the basal plane in close alignment with applied shear stress, producing ice that can be several times softer under shear than isotropic ice. Vertical-maximum fabric also develops under vertical compression. Unlike with simple shear, however, the ice becomes harder to the applied vertical compression with stronger single-maximum fabrics.

Given that fabric has such a strong effect on flow, and vice-versa, it is therefore important to understand it as a coupled system rather than treating flow and fabric separately. Many, or perhaps most, complex coupled dynamical systems of physical interest exhibit instability. Examples include the gravitational n-body problem, which has unstable solutions, or Earth's weather.

There are indications that coupled flow of anisotropic ice has instabilities as well. Thorsteinsson and Waddington [76] studied the development of low-angle stratigraphic wrinkles near ice divides. They concluded that single-maximum fabrics typical near ice divides enhance the ability of low-angle incipient wrinkles to steepen, and eventually overturn. The single-maximum fabrics near ice divides promote horizontal shear, which steepens incipient wrinkles, and hinder vertical compression, which flattens them. Fudge et al. [32] found evidence of boudinage in electrical conductivity measurements in the West Antarctic Ice Sheet Divide core. Boudinage effectively removes layers from the record, and additionally could act as a source of incipient stratigraphic wrinkles in the surrounding layers.

Alley et al. [7] found "striping" in the GISP2 core. These stripes were composed of elongated regions of grains possessing aligned, off-vertical c-axes, in a medium of vertical single-maximum fabric. In horizontal extension under divide flow, these stripes localize shear within them, and displace layers in the hard surrounding ice. Jansen et al. [47] produced bands similar to observed stripes in strong single-maximum fabrics using microstructure modeling. These were identified as shear bands. Regions where the fabric was tilted away from the lattice preferred orientation towards the direction of shear seeded the formation of the bands. These small-scale disturbances, which have been found hundreds of meters off the bed, cannot be related to basal topography. They must arise from inhomogeneities in the ice itself.

Montgomery-Smith [62] developed a coupled perturbation model for the orientations of slender fibers immersed in Stokes flow. It was shown that instabilities of fiber orientations can develop, which would not occur in uncoupled flow. Coupled ice flow and fabric are mathematically related to the case of fibers immersed in Stokes flow. In this paper, we derive a full-Stokes, coupled anisotropic-flow and fabric-perturbation model to study the stability of the coupled flow and fabric system, similarly to Montgomery-Smith [62]. We show that dynamical instability of fabric coupled to ice flow can seed such disturbances.

5.1.1 Background

Preferred c-axis orientations in ice develop primarily due to intracrystalline slip. This causes c-axes to rotate away from the directions of principal extensional strain [10]. ODFs are often summarized using orientation (or, moment) tensors (e.g. Svendsem and Hutter [73]). The second-order orientation tensor A_{ij} is the expectation $< c_i c_j >$, where $i, j = 1, 2, 3$. The mean of the ODF, $< c_i >$, is always zero because of antipodal symmetry. Therefore, A_{ij} is also the covariance matrix of the distribution, by definition of covariance as,

$$\mathrm{Cov}(c_i, c_j) =< (c_i - < c_i >)(c_j - < c_j >) > . \tag{5.1}$$

The diagonal elements A_{11}, A_{22}, and A_{33} give a measure of the c-axis concentration on the x, y, and z axes, respectively. Throughout this paper, the indices 1, 2, and 3 will be associated with the x-, y-, and z-directions, respectively. Similar to the second-order orientation tensor, the fourth-order tensor is the expected value $\mathbb{A}_{ijkl} =< c_i c_j c_k c_l >$. Since ODFs over the sphere are antipodally symmetric, odd-order tensors are zero. The second-order tensor may be eigendecomposed. The eigenvalues $\lambda_1 \leq \lambda_2 \leq \lambda_3$ sum to unity by construction. The eigenvectors, or fabric principal-directions, denote the directions of greatest density (corre-

Table 5.1: List of symbols

Symbol	**Definition**
q_i	Tensor quantity in index notation
$\mathbf{q}$	Same tensor in vector notation
c_i	ice-crystal c-axis for $i = 1, 2, 3$ in x, y, z directions
$\psi(\mathbf{c})$	Ice-crystal orientation dist. func.
$< q_i >$	Expected value of q_i under ψ
A_{ij}	Second-order orientation tensor $< c_i c_j > = < a_{ij} >$
$\mathbb{A}_{ijkl}$	Fourth-order orientation tensor $< c_i c_j c_k c_l >$
λ_i	Fabric eigenvalue of A_{ij}
J_{ij}	Jacobian matrix of the perturbed fabric system
ζ_i	Eigenvalues, or growth rates, of J_{ij}
V_{ij}	Vorticity, or spin, tensor
D_{ij}	Strain-rate tensor
ϕ	Angle of rotation about the y-axis
θ	Angle of rotation about the x-axis
δ_{ij}	Kronecker delta symbol
S_2	unit sphere
$\mathcal{R}_{ijkl}$	viscosity tensor
σ	A standard deviation
S_{ij}	Stress tensor
ϵ	A small parameter
κ_i	Three-dimensional wavevector
$\bar{y}$	An unperturbed quantity
$\hat{y}$	The Fourier coefficient of a perturbation to $\bar{y}$

sponding to the largest eigenvalue λ_3), smallest density (the smallest eigenvalue λ_1), and a direction orthogonal to the other two (corresponding to λ_2. An isotropic fabric has three equal eigenvalues. A girdle fabric (in which there is a band of high concentration along a great circle) has two nearly equal eigenvalues, and one small eigenvalue. A single-maximum fabric has one large eigenvalue, and two small ones.

If the evolution of the ODF is given by a PDE over the sphere, one may integrate A_{ij} to derive a ODE for the evolution of A_{ij}. Gillet-Chaulet et al. [38] used a Jeffery's-type equation for A_{ij} valid when the c-axes move by basal slip only. Their model works for arbitrary flow conditions. Gödert [40] developed a similar model incorporating spherical diffusion into the evolution equation for A_{ij}.

In general, linear anisotropic viscosity must be a fourth order, $3 \times 3 \times 3 \times 3$ tensor $\mathcal{R}_{ijkl}$. This is because it relates stress and strain rate, two second-order tensors. $\mathcal{R}_{ijkl}$ is a function of the ODF, and also the strain rate if it is a nonlinear constitutive relation. With no simplifications, this is too computationally and analytically difficult for most applications. However, numerous constitutive relations have been developed to account for anisotropy of ice in a more tractable way. The most popular and simple method is to use a scalar enhancement factor as a multiplier of fluidity in Glen's flow law, to adjust for anisotropy or other factors [53]. This method is mainly useful under flank flow using the shallow ice approximation. Since only horizontal shear stresses are significant, other stresses and their corresponding viscosity components may be ignored. The enhancement factor is usually chosen empirically. However, the enhancement factor method is not valid if the ODF does not have a vertical axis of symmetry. In this case, true anisotropic flow laws predict the development of larger normal stresses. This makes the assumption of a scalar enhancement factor invalid in these situations [66].

A number of anisotropic constitutive relations attempt to predict the flow response of a polycrystal from the properties and orientations of individual grains. This brings the problem of homogenization: it is necessary to relate the bulk stress and strain of the entire polycrystal to that experienced by individual grains in a consistent way. There are two possible end members. Homogeneous stress, or the Taylor-Bishop-Hill model [74], assumes that strain, but not stress, is identical in all grains. This has the advantage of maintaining spatial compatibility among grains. It is a good approximation for materials with several easily-activated slip systems. The homogeneous-strain assumption is an upper bound on the viscous dissipation of the polycrystal: For a given applied bulk strain, the hardest-oriented grains receive the same strain as the easiest-oriented grains. Hard-oriented grains produce more dissipation for the same strain compared to soft-oriented grains. At the other end, the homogeneous stress, or Sachs model [69], assumes that stress, but not strain, is identical between grains. This is the lower bound on dissipation. The key disadvantage of the Sachs bound is that spatial compatibility between grains is not maintained. Apart from these, the Visco-Plastic Self-Consistent (VPSC) homogenization scheme [52] attempts to more accurately treat homogenization by assuming that each individual grain is an ellipsoidal inclusion in a continuum that has the average properties of the polycrystal (rather than explicitly treating nearest-neighbor interactions). This scheme allows for consistent stress and strain homogenization intermediate between the homogeneous stress and homogeneous strain assumptions. However, the VPSC scheme does not have analytical solutions in general, requiring iterative numerical schemes.

In this paper, we use the homogeneous stress assumption for ice deformation, due to its simplicity. While strain compatibility is violated, the homogeneous stress assumption produces more accurate predictions of rheological properties than homogeneous strain in the case of ice [77]. This is due to basal slip being by far the most active slip system, with other slip systems accounting for far less strain. Materials with several active slip systems can be more accurately modeled with the homogeneous strain bound. The homogeneous stress assumption is a lower bound on the strength of anisotropy. Therefore, we can intuitively expect it to underestimate the strength of the coupling between fabric and flow.

5.2 Fabric Model

The most important process governing the development of crystal fabrics is deformation-induced grain rotation. If grain deformation is due solely to basal glide, the rate of change of the c-axis orientation is the sum of bulk rotation and viscoplastic spin. From Meyssonnier and Philip [58], the evolution of c-axis orientation in response to strain can be described by a modified Jeffery's equation [48]:

$$\dot{c_i} = V_{ij}c_j - D_{ij}c_j + c_i c_j c_k D_{jk}, \tag{5.2}$$

where c_i is the unit vector in the direction of the c-axis. The tensors V_{ij} and D_{ij} are the vorticity tensor, and local strain-rate tensor of the grain, respectively. The first term gives the rotation rate due to the bulk rotation of the polycrystal, while the second term gives the rotation rate due to viscoplastic spin. Thus, for example, the c-axis of a grain experiencing uniaxial compression will rotate towards the compressive direction. The last term of Jeffery's equation (5.2) ensures that the motion of grain orientation is tangent to the unit sphere at $\mathbf{c}$, which is necessary due to the convention that the c-axis vector is of unit length. This can be seen by noting that the $V_{ij}c_j$ term does not affect the magnitude of c_i, leaving only the $D_{ij}c_j$ term. Assume that at time $t = 0$, the c-axis is given by $\mathbf{c}_0$. After a short length of time δt, the magnitude of the new c-axis $\mathbf{c}_{\delta t}$ is (without the final term in Eq. 5.2),

$$\begin{aligned} ||\mathbf{c}_{\delta t}|| &= ||\mathbf{c}_0 - \delta_t \mathbf{D}\mathbf{c}|| && (5.3)\\ &\approx ||\mathbf{c}_0|| - \mathbf{c}_0^T \mathbf{D}\mathbf{c}_0 \delta t && (5.4)\\ &= 1 - \mathbf{c}_0^T \mathbf{D}\mathbf{c}_0 \delta t, && (5.5) \end{aligned}$$

to first order in δt. Thus, for the c-axis to maintain unit length, we must add the quantity $\mathbf{c}^T \mathbf{D}\mathbf{c}\delta t$ projected onto $\mathbf{c}$. This then gives the last term of (5.2).

The above equation gives the evolution of a single grain in response to the applied velocity gradient. It is not practical to integrate this equation for each grain in a polycrystal. Instead, we may instead derive an equation for the second-order orientation tensor $A_{ij} =< c_i c_j >$ by integrating the material derivative of the structure tensor $c_i c_j$ over the ODF:

$$\frac{dA_{ij}}{dt} = < \dot{c}_i c_j > + < c_i \dot{c}_j > . \tag{5.6}$$

Expressing the material derivative in spatial coordinates yields,

$$\frac{\partial A_{ij}}{\partial t} + u_k \frac{\partial A_{ij}}{\partial x_k} = V_{ik} A_{kj} - A_{ik} V_{kj} - D_{ik} A_{kj} - A_{ik} D_{kj} + 2\mathbb{A}_{ijkl} D_{kl}, \tag{5.7}$$

where D_{ij} is the strain-rate tensor, W_{ij} is the vorticity tensor, and A_{ijkl} is the fourth-order orientation tensor $< c_i c_j c_k c_l >$. Unfortunately, the presence of $\mathbb{A}_{ijkl}$ introduces the closure problem. The fourth-order orientation tensor cannot in general be determined from A_{ij}. An ODE for A_{ijkl} may be derived, however it in turn depends on the sixth-order orientation tensor, and so on. Therefore, some kind of an approximation of $\mathbb{A}_{ijkl}$ in terms of A_{ij} must be taken. Here, we use the popular and simple quadratic closure [3], where $\mathbb{A}_{ijkl} = A_{ij} A_{kl}$. This closure is accurate whenever the largest eigenvalue $\lambda_3 > 0.8$. It is exact for perfect single-maximum fabrics, where $\lambda_3 = 1$. Deeper layers of ice sheets typically have strong single-maximum fabrics, so this is a good approximation for our purposes.

5.3 Flow Model

We now outline the constitutive relation and physical equations of our flow model. We use the constitutive relation for an orthotropic material with linear transversely isotropic components from Gillet-Chaulet et al. [37]. Let η be the viscosity of shear in the basal plane. Also, let β be the ratio of viscosity for shear parallel to the basal plane to that in the basal plane, and γ be the viscosity in response to normal stress along the c-axis to that in the basal plane. We assume $\gamma \approx 1$, because ease of deformation by compression is approximately the same in the c-axis direction as along the basal plane. We set $\beta = 10^{-2}$, and $\eta = 1$. The inverse form of the constitutive relation is given by,

$$D_{ij} = \frac{\beta}{2\eta} \left[S_{ij} + \xi_1 \mathbb{A}_{ijkl} S_{kl} + \xi_2 (S_{ik} A_{kj} + A_{ik} S_{kj}) + \xi_3 A_{kl} S_{kl} \delta_{ij} \right], \tag{5.8}$$

where,

$$\xi_1 = 2\left(\frac{\gamma + 2}{4\gamma - 1} - \frac{1}{\beta} \right), \ \xi_2 = \left(\frac{1}{\beta} - 1 \right), \ \xi_3 = -\frac{1}{3}(\lambda_1 + 2\lambda_2). \tag{5.9}$$

The standard form of the constitutive relation, with stress as a function of strain rate, is then found by inverting this relation. The fluidity $\mathcal{R}^{-1}_{ijkl}$ of the consitutive relation given by Eq. (5.8) is a fourth-order tensor formed found from the coefficient of S_{ij}, from adding up the terms of Eq. (5.8) with appropriate representation of each term as a fourth-order tensor coefficient of S_{ij}. The viscosity in Eq. (5.8) is also a fourth-order tensor $\mathcal{R}_{ijkl}$, given by the inverse of $\mathcal{R}^{-1}_{ijkl}$.

It is often useful to write anisotropic constitutive relations in terms of Voigt notation [80], in which symmetric fourth-order tensors are represented as matrices, and symmetric second-order tensors are represented as vectors. The viscosity $\mathcal{R}_{ijkl}$ may be represented as a 6×6 symmetric matrix R_{ij}. Likewise, the symmetric stress tensor may be represented as a six-vector s_i, where $s_i = S_{ii}$ for $i = 1, 2, 3$, $s_4 = S_{23}$, $s_5 = S_{13}$, and $s_6 = S_{12}$. The case for D_{ij} is identical. Then, the constitutive relation is just $s_i = R_{ij} d_j$, where d_i is the Voigt form of D_{ij}.

Along with the constitutive relation, Stokes flow is governed by stress balance and incompressibility,

$$\frac{\partial S_{ij}}{\partial x_j} - \frac{\partial p}{\partial x_i} = 0, \tag{5.10}$$

$$\frac{\partial u_i}{\partial x_i} = 0. \tag{5.11}$$

The stress S_{ij} in (5.10) is given by the inverse of (5.8).

5.4 Perturbation approximation

Now we derive an analytical coupled first-order perturbation model from the equations, (5.7), (5.8), (5.10), (5.11). We seek seek to see how a small perturbation to background fabric can grow or disappear under this system.

First, assume a background velocity gradient of $\bar{\boldsymbol{U}}$, homogeneous in all three dimensional space. We may assume that the velocity vanishes at the origin. With this background velocity gradient, the unperturbed $\bar{\boldsymbol{A}}$ may be found from (5.7), given initial conditions. Likewise, the unperturbed stress $\bar{\boldsymbol{S}}$ may also be found.

Figure 5.1: Cartoon of the form of a sinusoidal perturbation in space with spatial wavevector $\boldsymbol{\kappa}$. The shading represents the sign and magnitude of $\cos(\boldsymbol{\kappa} \cdot \boldsymbol{x})$, for a perturbation of the form $\hat{\boldsymbol{v}} \cos(\boldsymbol{\kappa} \cdot \boldsymbol{x})$, where $\hat{\boldsymbol{v}}$ is the Fourier coefficient of the perturbation. The sinusoidal perturbation extends throughout three-dimensional space. The plane of the perturbation is given by the plane which is normal to the wavevector. In this diagram, the positive x-axis extends outwards from the page.

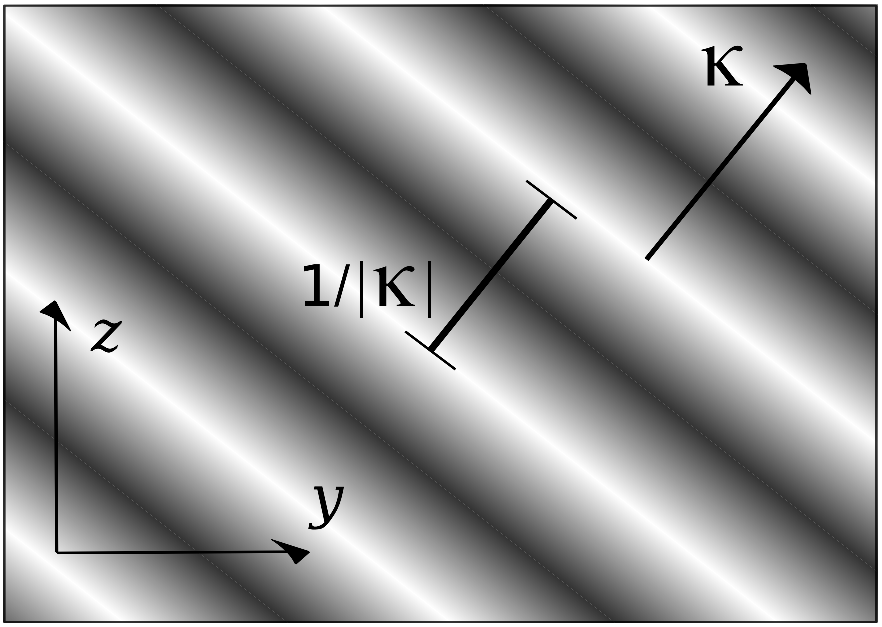

The unperturbed quantities above are all homogeneous throughout space. Suppose there is now a perturbation of fabric with a single Fourier wavevector $\boldsymbol{\kappa}$. The wavevector is a vector, rather than a wavenumber, because it is for three-dimensional space. This gives sinusoidal perturbations, where the normal to the plane of the perturbation is the wavevector. See Fig. (5.1) for a cartoon. The perturbation to the second-order orientation tensor is given by, $\boldsymbol{A} \to \bar{\boldsymbol{A}} + \epsilon\hat{\boldsymbol{A}}\cos(\boldsymbol{\kappa}\cdot\boldsymbol{x})$. The parameter ϵ is small enough that we may neglect ϵ^2 and higher powers. The tensor $\hat{\boldsymbol{A}}$ is the Fourier coefficient of the perturbation. Other quantities with hats and bars are defined similarly. We emphasize that the only spatial variability of this perturbation is due to the cosine term.

The perturbations themselves are deformed by flow over time, therefore $\boldsymbol{\kappa}$ is not constant in time. The quantity $\hat{\boldsymbol{A}}$ is a Fourier coefficient which is constant throughout space. From Montgomery-Smith [62], to satisfy Jeffery's equation $\boldsymbol{\kappa}$ must have the form,

$$\left(\frac{\partial}{\partial t} + \nabla\cdot\boldsymbol{u}\right)\left(\hat{\boldsymbol{A}}\cos(\boldsymbol{\kappa}\cdot\boldsymbol{x})\right) = \frac{\partial\hat{\boldsymbol{A}}}{\partial t}\cos(\boldsymbol{\kappa}\cdot\boldsymbol{x}) + \mathcal{O}(\epsilon^2). \tag{5.12}$$

Simplifying this equation and discarding terms of ϵ^2 and higher, the first-order equation for the evolution of the wavenumber is

$$\frac{\partial}{\partial t}\boldsymbol{\kappa} = -\bar{\boldsymbol{U}}^T\boldsymbol{\kappa}, \tag{5.13}$$

where again $\bar{\boldsymbol{U}}$ is the unperturbed velocity gradient. The solution for an initial wavevector $\boldsymbol{\kappa}(0)$ and a constant velocity gradient is $\boldsymbol{\kappa}(t) = \exp(-t\bar{\boldsymbol{U}}^T)\boldsymbol{\kappa}(0)$.

Now we seek to derive an approximate evolution equation for the fabric perturbation $\hat{\boldsymbol{A}}$ (under the assumption that $\epsilon^2 \approx 0$), to see how it grows or shrinks. Since fabric evolution is dependent on flow, we first see how the fabric perturbation affects the flow equations (5.8), (5.10), and (5.11). We will solve these flow equations to get perturbations of velocity and pressure, and from that substitute the perturbed velocity gradient back into Eq. (5.7) (while discarding higher-order terms).

To first order, there are no other spatial Fourier components to any of the other perturbed quantities other than that given by the wavevector $\boldsymbol{\kappa}$. This is because any interaction of different wavevectors would be $\mathcal{O}(\epsilon^2)$ or higher, which is negligibly small. Therefore, we make the following replacements,

$$\boldsymbol{u} \to \bar{\boldsymbol{u}} + \epsilon \hat{\boldsymbol{u}} \sin(\boldsymbol{\kappa} \cdot \boldsymbol{x}) \tag{5.14}$$

$$\boldsymbol{S} \to \bar{\boldsymbol{S}} + \epsilon \hat{\boldsymbol{S}} \cos(\boldsymbol{\kappa} \cdot \boldsymbol{x}) \tag{5.15}$$

$$\boldsymbol{D} \to \bar{\boldsymbol{D}} + \epsilon \hat{\boldsymbol{D}} \cos(\boldsymbol{\kappa} \cdot \boldsymbol{x}) \tag{5.16}$$

$$p \to \bar{p} + \epsilon \hat{p} \sin(\boldsymbol{\kappa} \cdot \boldsymbol{x}) \tag{5.17}$$

$$\boldsymbol{R} \to \bar{\boldsymbol{R}} + \epsilon \hat{\boldsymbol{R}} \cos(\boldsymbol{\kappa} \cdot \boldsymbol{x}) \tag{5.18}$$

$$\tag{5.19}$$

Now, we substitute these perturbed quantities into the flow equations, and neglect terms of $\mathcal{O}(\epsilon^2)$ and higher. The perturbed fluidity in Voigt notation, $\hat{\boldsymbol{R}}^{-1}$, is found by substituting $\bar{\boldsymbol{D}} + \epsilon \hat{\boldsymbol{D}} \cos(\boldsymbol{\kappa} \cdot \boldsymbol{x})$ into Eq. (5.8), then subtracting out the unperturbed fluidity, and removing terms of $\mathcal{O}(\epsilon^2)$ and higher. The spatially-variable $\cos(\boldsymbol{\kappa} \cdot \boldsymbol{x})$ appears in every term, and can be cancelled out. This removes any dependence on the spatial location $\boldsymbol{x}$. Then, it can be shown that to first order, the Fourier component of the perturbation of viscosity is given by $\hat{R}_{ij} = -\bar{R}_{ik} \hat{R}^{-1}_{kl} \bar{R}_{lj}$. We can then use this to find Fourier component of the stress perturbation, $\hat{S}_{ij}$, if one knows the pertubations to stress and strain:

$$\hat{\boldsymbol{U}} = \frac{\partial \boldsymbol{u}}{\partial \boldsymbol{x}} \frac{1}{\cos(\boldsymbol{\kappa} \cdot \boldsymbol{x})} = \hat{\boldsymbol{u}} \otimes \boldsymbol{\kappa}, \tag{5.20}$$

$$\hat{\boldsymbol{D}} = \frac{1}{2} \left(\hat{\boldsymbol{U}} + \hat{\boldsymbol{U}} \right), \tag{5.21}$$

$$\hat{\boldsymbol{W}} = \frac{1}{2} \left(\hat{\boldsymbol{U}} - \hat{\boldsymbol{U}}^T \right), \tag{5.22}$$

$$\hat{\boldsymbol{s}} = \hat{\boldsymbol{R}} \bar{\boldsymbol{d}} + \bar{\boldsymbol{R}} \hat{\boldsymbol{d}}, \tag{5.23}$$

where $\boldsymbol{s}$ and $\boldsymbol{d}$ are respectively the stress and strain tensors represented in Voigt notation. Force balance and incompressibility perturbations by substituting the perturbed stress ($\bar{\boldsymbol{S}} + \epsilon \cos(\boldsymbol{\kappa} \cdot \boldsymbol{x}) \hat{\boldsymbol{S}}$) and pressure ($\bar{p} + \epsilon \sin(\boldsymbol{\kappa} \cdot \boldsymbol{x}) \hat{p}$) into the flow equations (5.10) and (5.11). After cancelling out the spatially-variable $\sin(\boldsymbol{\kappa} \cdot \boldsymbol{x})$ from each equation, this yields,

$$\hat{\boldsymbol{S}}\boldsymbol{\kappa} + \boldsymbol{\kappa}\hat{p} = 0, \tag{5.24}$$

$$\boldsymbol{\kappa} \cdot \hat{\boldsymbol{u}} = 0. \tag{5.25}$$

Knowing the Fourier coefficient of the perturbed second-order orientation tensor, $\hat{\boldsymbol{A}}$, we can now use Eq. (5.24) and Eq. (5.25) to analytically solve for the perturbed $\hat{\boldsymbol{u}}$ and $\hat{p}$, and in turn $\hat{\boldsymbol{D}}$ and $\hat{\boldsymbol{W}}$. In both Eqs. (5.24) and (5.25), $\cos(\boldsymbol{\kappa} \cdot \boldsymbol{x})$ appears in each term as the only spatially variable component, and can thus be cancelled out. This produces a spatially-homogeneous algebraic system. We can now write our equation for the evolution of $\hat{\boldsymbol{A}}$ as,

$$\begin{aligned}\frac{d\hat{\boldsymbol{A}}}{dt} &= \boldsymbol{\mathcal{Q}}(\hat{\boldsymbol{A}}, \bar{\boldsymbol{A}}, \bar{\boldsymbol{D}}, \bar{\boldsymbol{W}}, \boldsymbol{\kappa}) \\ &= \hat{\boldsymbol{V}}\bar{\boldsymbol{A}} + \bar{\boldsymbol{V}}\hat{\boldsymbol{A}} - \hat{\boldsymbol{A}}\bar{\boldsymbol{V}} - \bar{\boldsymbol{A}}\hat{\boldsymbol{V}} - \hat{\boldsymbol{D}}\bar{\boldsymbol{A}} - \bar{\boldsymbol{D}}\hat{\boldsymbol{A}} - \hat{\boldsymbol{A}}\bar{\boldsymbol{D}} - \bar{\boldsymbol{A}}\hat{\boldsymbol{D}} \\ &+ 2\left(\hat{\boldsymbol{A}}\bar{\boldsymbol{A}}\bar{\boldsymbol{D}} + \bar{\boldsymbol{A}}\hat{\boldsymbol{A}}\bar{\boldsymbol{D}} + \bar{\boldsymbol{A}}\bar{\boldsymbol{A}}\hat{\boldsymbol{D}}\right)\end{aligned} \tag{5.26}$$

This is a linear system of ordinary differential equations. Note that the perturbed $\hat{\boldsymbol{D}}$ and $\hat{\boldsymbol{W}}$ depend on $\hat{\boldsymbol{A}}$ through the previous flow equations. Next, we linearize this equation in Voigt notation, with $\hat{\boldsymbol{A}}$ being represented by a six-vector $\hat{\boldsymbol{a}}$. This then gets us the Jacobian of the system, given by,

$$\boldsymbol{J} = \left.\frac{\partial \boldsymbol{q}}{\partial \hat{\boldsymbol{a}}}\right|_{\hat{\boldsymbol{a}}=0} \left(\boldsymbol{0}, \bar{\boldsymbol{A}}, \bar{\boldsymbol{D}}, \bar{\boldsymbol{W}}\right) \tag{5.27}$$

where $\boldsymbol{q}$ is $\boldsymbol{\mathcal{Q}}$ in Voigt notation. The eigenvalues ζ_i of $\boldsymbol{J}$ give the stability of the system as a function of the unperturbed fabric, velocity gradient, and wavevector of the perturbation. If there is an eigenvalue with a positive real part, the system is unstable about the equilibrium $\hat{\boldsymbol{A}} = 0$. A small nudge in the direction of the corresponding eigenvector will grow. Note that the eigenvectors of this system are characteristic perturbations of $\bar{\boldsymbol{a}}$ in Voigt notation, or $\bar{\boldsymbol{A}}$ in standard notation. The corresponding eigenvalues give the growth rates of the corresponding characteristic perturbation of $\bar{\boldsymbol{A}}$. Thus, they may be thought of as "eigenmatrices." In the next section, we examine the stability of this system for different flow regimes and perturbation wavevectors.

5.5 *Results*

We now present results for layered perturbations in pure shear and horizontal simple shear, at different angles to flow. To do this, we forced the perturbation model with wavevectors rotated about the x- and y-axes at different angles from vertical. This corresponds to having layered perturbations whose planes are rotated from horizontal by the same angles. We plot the real part of the largest eigenvalue of the linearized system for each flow scenario. This gives the perturbation of $\boldsymbol{A}$ with the fastest growth rate. Note that a perturbation eigenvalue may be interpreted as a growth rate of the paired perturbation "eigenvector" of $\boldsymbol{A}$. We examine only the real parts of the eigenvalues (which are complex in general) because the imaginary part corresponds to spinning about the fixed point of the perturbation (where $\hat{\boldsymbol{a}} = 0$), and is not as relevant to stability. In addition, the complex eigenvalues come in conjugate pairs, associated with complex conjugate-pair eigenvectors, which are not physical. A perturbation with a real growth rate, equal to the real part of the complex eigenvalues, can be formed by taking a linear combination of the complex-conjugate pair. Everywhere we take the unperturbed fabric to be a vertical single-maximum, where the two smallest eigenvalues are equal, and the largest eigenvalue λ_3 ranges from 0.8 to unity.

5.5.1 *Layered perturbations in simple shear*

First, we take the background flow to be simple shear, with the unperturbed component of the velocity-gradient tensor $\bar{U}_{12} = 1$, and other components set to zero. We examine layered perturbations where the plane of perturbation is rotated around by several angles about the x-axis and y-axis. For perturbations rotated about either axis, there is an axis of symmetry for the largest eigenvalue about the rotation angle of $\pi/4$. This means that, for example, a layer angled at $\pi/7$ will have the same growth rate as one angled at $7\pi/7$. This reduces the range of angles we must plot. This symmetry does not hold for general rotations.

Figure 5.2: The largest real part of the eigenvalues of the Jacobian matrix (5.27) under simple shear, as a function of the largest fabric eigenvalue λ_3. Each curve is a perturbation whose wavevector has been rotated by a different angle ϕ about the y-axis.

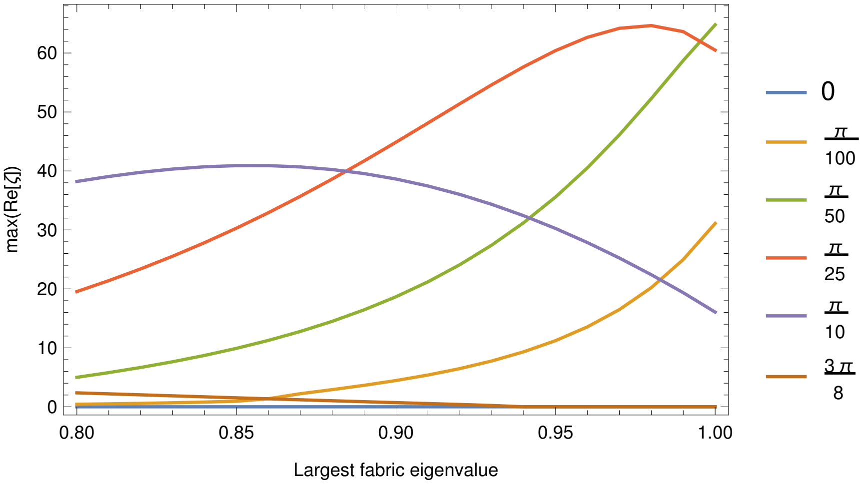

Figure 5.3: The largest real part of the eigenvalues of the Jacobian matrix (5.27) under pure shear, as a function of the largest fabric eigenvalue λ_3. Each curve is a perturbation whose wavevector has been rotated by a different angle θ about the x-axis.

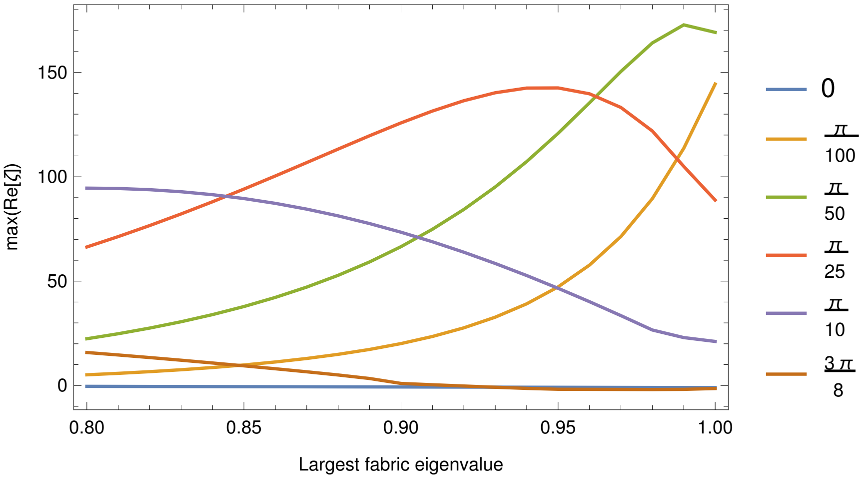

Figure 5.4: The largest real part of the eigenvalues of the Jacobian matrix (5.27) under pure shear, as a function of the largest fabric eigenvalue λ_3. Each curve is a perturbation whose wavevector has been rotated by a different angle ϕ about the y-axis.

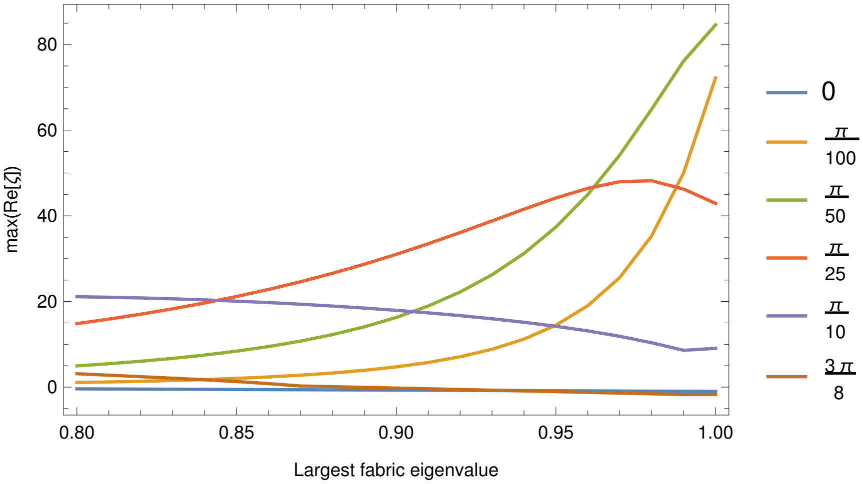

We first discuss the case where the wavevector is rotated about the y-axis by an angle θ, shown in Fig. 5.2. This corresponds to a layered perturbation whose plane which is tilted in the y-direction. When the plane of the perturbations is horizontal ($\theta = 0$), with a vertical wavevector, the fabric is stable. In this case, the real part of the largest eigenvalue is identically zero across the entire range of fabric eigenvalues plotted. However, instabilities occur when the wavenumber (and plane of perturbations) is rotated from vertical about the x-axis. For strong fabrics with $\lambda_3 > 0.9$, perturbation planes with shallow dips or dips near vertical have the highest growth rates. Perturbations with dip angles closer to $\pi/2$ become small or negative for strong fabrics whose largest fabric eigenvalues are more than about 0.9. In all cases, the velocity perturbation is confined to the y direction, as can be seen in Table 5.2. This is because the wavevector is orthogonal to this direction.

Interestingly, the growth rates of perturbations whose wavevectors are rotated about the y-axis are very close to those rotated about the x-axis. This can be seen in Table 2. For perturbations whose wavevectors are rotated about the y-axis, the velocity Fourier coefficient in the x direction, $\hat{u}_1$ is of equal and opposite sign to the velocity component in the y direction of the perturbation with the wavenumber tilted by the same angle about the y axis.

The situation is somewhat different if the wavenumber is rotated by about both the x-axis and the y-axis (see Table 5.2). In this case, nonzero velocity perturbations may occur in the x and z directions as well. This is important because stratigraphic folding requires a vertical velocity component to develop. Therefore, in the context of this model, stratigraphic disruption is a three-dimensional phenomenon in simple shear, and cannot be captured in two dimensions.

Table 5.2: Fourier coefficients $\hat{u}_i$ of the perturbed velocity, and the highest perturbation growth rate (max(Re(ζ))) for perturbations whose planes of perturbation are rotated from horizontal by a rotation of θ about the y-axis, and then a rotation of ϕ about the x-axis. The unperturbed background flow is simple shear. The largest fabric eigenvalue is 0.8.

θ	ϕ	max(Re(ζ))	$\hat{u}_1$	$\hat{u}_2$	$\hat{u}_3$
0	0	0	0	0	0
$\pi/100$	0	0.79	0	-1.84	0
$3\pi/8$	0	2.02	0	-5.96	0
0	$3\pi/8$	2.36	5.96	0	0
0	$\pi/100$	0.43	1.84	0	0
$\pi/8$	$3\pi/8$	6.69	-0.15	-4.37	-5.1

5.5.2 Layered perturbations in pure shear

We now examine the case of pure shear in the xz-plane, as commonly seen near ice divides. We first look at the case where the planes of perturbation are rotated about the y-axis, but with no rotation about the x-axis. The results are shown in Fig. 5.4. Horizontal layers are again completely stable; the growth rates of perturbations are negative. There is no associated velocity perturbation. However, again layers with shallow dips are unstable, with high growth rates. Growth rates are higher for strong single-maximum fabrics for perturbations with shallow dips. Layers with steeper dips have lower growth rates, and

Table 5.3: Fourier coefficients $\hat{u}_i$ of the perturbed velocity, and the highest perturbation growth rate (max(Re(ζ))) for perturbations whose planes of perturbation are rotated from horizontal by a rotation of θ about the x-axis, and then a rotation of ϕ about the x-axis. The unperturbed background flow is pure shear. The largest fabric eigenvalue is 0.8.

θ	ϕ	max(Re(ζ))	$\hat{u}_1$	$\hat{u}_2$	$\hat{u}_3$
0	0	-0.4	0	0	0
$\pi/100$	0	1.08	0	0.53	-0.17
$3\pi/8$	0	3.13	0	0.794	-1.92
0	$\pi/100$	5.13	-2.36	0	-0.07
0	$3\pi/8$	15.81	-3.53	0	-8.54
$\pi/8$	$3\pi/8$	13.82	-3.54	0.83	-7.66

become stable for strong single-maximum fabrics. When the wavenumber is rotated about the x-axis as well, fabrics become generally less stable.

The highest growth rates for perturbations whose wavevectors are rotated about the x-axis are shown in Fig. 5.3. The results are similar to the case where the wavevector is rotated about the x-axis (Figure 5.4), except the growth rates are generally higher. The growth rates for more steeply-dipped perturbations are near zero for strong fabrics, but do not become strongly negative.

In Table 5.3, the Fourier coefficients of velocity perturbations and maximum growth rates are listed for perturbations whose wavevectors are rotated from vertical by several combinations of angles ϕ (about the y-axis) and θ (about the x-axis). This table illustrates that the wavevector must have a nonzero component in both x- and y-directions in order to produce a nonzero velocity perturbation in all three directions.

5.5.3 *Discussion*

In the flow scenarios considered, dynamic instability seems to be the rule rather than the exception. An important constraint to the flow perturbations is that the perturbed velocity must be orthogonal to the wavevector, and parallel to the plane of the perturbations. This can be seen from the incompressibility constraint (5.25) in the perturbation model, $\hat{\boldsymbol{u}} \cdot \boldsymbol{\kappa} = 0$. Since the velocity perturbation is $\epsilon \hat{\boldsymbol{u}} \cos(\boldsymbol{\kappa} \cdot \boldsymbol{x})$, this means that the velocity perturbation must be orthogonal to the wavevector. Thus, if the wavevector is vertical, then there cannot be a vertical component to the velocity perturbation. The perturbed velocity gradient must consist solely of shear orthogonal to the wavevector.

To overturn stratigraphic layers in ice sheets, there must be a vertical velocity component. This means that perturbations of horizontal layers can never generate vertical movement, since the velocity perturbation is confined to the plane of perturbation. However, a layer needs to be tilted only a small amount to produce a vertical-velocity perturbation, and fabric perturbations on layers with shallow but nonzero dips tend to have higher growth rates. This corresponds to "buckling." Depending on the sign of $\cos(\boldsymbol{\kappa} \cdot \boldsymbol{x})$, this perturbation moves some ice upwards, and other ice downwards. In flank flow, the perturbation must have a tilt in both x and y to generate vertical motion.

Growth rates of perturbations in this model can be very high. However, it is important to keep in mind some of the limitations of this model. It is applicable only to perturbations with thicknesses sufficiently smaller than the ice sheet. For thick layers, the effects of the ice-sheet boundaries become more important, violating the assumptions of this model. The scale of perturbations must also be large enough that the ice can be treated as a continuum. In addition, it is a first-order model, valid for small perturbations. As perturbations become larger, higher-order effects (which this model does not capture) become important. However, the stability of perturbations in this model can show in which situations perturbations can develop in the first place.

Even with a high growth rate, a sufficiently-small initial perturbation could take quite some time to grow large. For this reason, we do not expect large perturbations to develop in upper layers of ice sheets. However, perturbations may have enough time to develop in the lower layers of ice sheets. This may be especially true for flank flow, where simple shear dominates. The high shear stress near the bed would accelerate the growth of the perturbations.

It is possible that the effects of coupled flow on perturbations, studied in this paper, may reinforce the development of perturbations from other sources. Disturbed layering is ubiquitous in deeper layers of ice sheets, and any flow disruption will also have a corresponding effect on fabric. Disturbances due to basal topography, spatially-variable recrystallization, or basal freeze-on may provide additional means of seeding fabric perturbations.

5.6 Conclusions

Due to the strong viscous anisotropy of ice as a function of c-axis orientation fabric, it is important to understand flow of anisotropic ice as a coupled system. To this end, we developed a first-order coupled perturbation model of fabric evolution and flow of anisotropic ice. We examined the stability of the system under various perturbations and flow scenarios. Under this model, coupled ice flow and fabric evolution is unstable across a wide range of flow and fabric conditions. Fabric perturbations are capable of causing vertical-velocity gradients for both simple shear and pure shear. This is a potential mechanism for stratigraphic disruption in ice. The instabilities would not occur in fabric that is uncoupled to flow. These types of perturbations may help explain the small-scale stratigraphic disturbances seen far above the bed in ice sheets. In addition, it provides a means of growth for fabric perturbations from other sources.

Further numerical simulations of macroscopic coupled flow and fabric would shed more light on the development of perturbations. The numerical model of coupled fabric and plane flow in Gillet-Chaulet et al. [38] seems to show large fabric perturbations developing in response to basal topography. Additional numerical simulations, especially three-dimensional ones, in different flow scenarios, and with different initial fabric perturbations, would be useful. The results from this analytical model suggest that two-dimensional flow models are not capable of capturing the growth of perturbations in simple shear. This reinforces the fact that flow of anisotropic ice and fabric development is a fundamentally three-dimensional problem which cannot be represented as plane flow.

Chapter 6

CONCLUSIONS

6.1 Summary

Chapter 2 develops novel analytical and bootstrap estimates of the sampling error of fabric eigenvalues and fabric eigenvectors. I showed that typically very uneven grain-size distributions produce much larger uncertainties in area-weighted estimates of fabric properties. I also applied bootstrapping to estimate the confidence intervals of the inferred strain enhancement factor in simple shear. Due to the power-law rheology of ice, I showed that the enhancement factor is very poorly constrained by thin sections. I also introduced a new parameterized orientation distribution function, the Bingham distribution, to glacioogy. I compared the performance of this distribution to the Dinh-Armstrong distribution and the Fisherian distribution proposed by Lliboutry. I showed that the Dinh-Armstrong distribution and the Bingham distribution produce much better fits than the Fisherian distribution. This underscores the shortcomings of axially-symmetric distributions for representing most realistic fabrics seen in ice cores.

Chapter 3 explores the use of sonic velocity measurements to infer ice fabric in boreholes, with application to P-wave data taken from NEEM. I developed a model which estimates eigenvalues in boreholes using both thin-section measurements and P, Sv, and Sh sonic velocities. This model helps combine the relative strengths of the two measurement methods, while reducing their relative weaknesses. Thin-section samples provide unbiased (although possibly dependent) measurements of thin-section samples, but they have typically large sampling error. Sonic velocity measurements, on the other hand, nearly eliminate sampling error due to the large amount of ice sampled by the sound waves. However, model error can be significant. In addition, poor tool centering was a problem at NEEM, which produced large but fairly smooth biases in the measured velocity. The method uses thin-section derived eigenvalues to correct for this bias, producing continuous, more accurate estimation of fabric eigenvalues.

The next two chapters move from examining error in measurement of fabric characteristics to looking at stability of ice crystal fabrics in response to flow or fabric perturbations. The fourth chapter examined the response of fabrics to small flow perturbations. I showed that under random velocity gradient perturbations, tilted-cone fabrics (where the largest concentration is not vertical) can develop in simple shear and pure shear. This can produce deformation in components other than the applied stress, and potentially induce stratigraphic disruption.

The fifth chapter develops a first-order coupled model of anisotropic ice-flow and fabric evolution. It is informative to treat fabric evolution and anisotropic flow as a coupled system, since fabric greatly affects flow, and vice-versa. I applied this model to examine the stability of spatially heterogeneous fabric perturbations in both simple shear and pure shear. I showed that single-maximum fabrics in this coupled system are unstable. This has important implications for the development of stratigraphic disruption in ice sheets. All unstable perturbations in this model cause vertical offset in layers, which can invert stratigraphic layers.

6.2 Implications

This thesis reinforces the utility of sonic measurements of fabric to avoid the severe sampling error and spatial discontinuities of thin-section fabric measurements. Future work incorporating S-waves will expand the usefulness of sonic method by allowing inference of information on azimuthal c-axis concentration. However, despite their inaccuracy, thin-section fabric measurements can be effectively used in combination with sonic measurements.

This work underscores the difficulty of predicting ice-core fabrics and anisotropic ice-flow. My work indicates that basal ice flow and fabric development may be nearly impossible to predict accurately on smaller length scales at high strains, due to the instabilities of coupled ice flow and fabric evolution. Further numerical investigations of coupled anisotropic ice-flow and fabric evolution would be useful to expand on the analytical treatment in Chapter 5. In particular, larger-scale perturbations which interact with the ice boundaries or temporal flow perturbations could be investigated.

This thesis also lends support to the idea that fabric anisotropy may aid the development of stratigraphic disturbances in basal ice. Stratigraphic disturbances are very commonly seen in ice cores (e.g. Fuchs and Leuenberger [31]) Alley et al. [7]). Steeply dipping disturbed basal layers are also a leading candidate for the cause of the abrupt loss of radar returns in echo-free zones in Greenland and Antarctica [22]. Irregular bed topography alone cannot explain stratigraphic disturbances. Temporal variations in flow over an irregular bed or significant basal freeze-on can cause stratigraphic disruption. However, I speculate that interactions of fabric with ice flow, sometimes in concert with temporal flow and bed topography, are a better explanation of the seeming ubiquitousness of disturbed basal ice. Unlike temporal flow or basal freeze-on, fabric exerts a strong influence on ice flow everywhere, which is not necessarily true of these other processes.

.1 Appendix A: Derivation of analytical estimates of sampling error

We now derive analytical estimates for sampling error from estimating the bulk second-order orientation tensor from ice core thin sections. First, we focus on the case of per-pixel EBSD or automatic fabric analyzer measurements, which typically yield many measurements per grain. We take into account correlations between different measurements. It is important to take depedendence between measurements into account in this case. Samples taken from the same grain will be highly correlated, since intragranular misorientations are typically no more than a few degrees.

In this section, upper indices represent spatial locations, and lower indices are indices for tensor quantities at one location. For example, c_i^k is the i component of the c-axis tensor at spatial location k. Let $\tilde{A}_{ij} = \sum_k a_{ij}^k / N$ be the sample estimate of A_{ij}, where $a_{ij}^k = c_i^k c_j^k$ (no sum in k) is a component of the structure tensor for an individual c-axis measurement, and N is the total number of measurements. We assume that each measurement is equally weighted, for simplicity of presentation. Extending these results to the case where measurements are not equally weighted is fairly simple.

Suppose that we can determine a covariance tensor giving the covariance between the ij component of the structure tensors at spatial locations k and l. This is given by,

$$C_{ij}^{kl} = \mathrm{Cov}(a_{ij}^k, a_{ij}^l). \tag{1}$$

Now, we wish to determine the variance of the sample estimate $\tilde{A}_{ij}$. First, note that $\mathrm{Var}(a_{ij}^k/N) = \mathrm{Var}(a_{ij}^k)/N^2$. Also, the variance of a sum of random variables $X_1, ..., X_n$ is,

$$\mathrm{Var}\left(\sum_i X_i\right) = \sum_{i,j} \mathrm{Cov}(X_i, X_j) \tag{2}$$

Since $\tilde{A}_{ij} = \sum_k a^k_{ij}/N$, we have,

$$\mathrm{Var}(\tilde{A}_{ij}) = \mathrm{Var}\left(\sum_k \frac{a^k_{ij}}{N}\right) \tag{3}$$

$$= \sum_{k,l} \frac{C^{kl}_{ij}}{N^2} \tag{4}$$

where C^{kl}_{ij} is the covariance between the structure tensor a^k_{ij} at site k and a^l_{ij} at site l, and N is the total number of measurements in the thin section. From the previous equation, we can see that if each structure-tensor measurement is strongly correlated with m other measurements, then the variance of $\tilde{A}_{ij}$ would be approximately m times larger than if it were uncorrelated. In a high-resolution per-pixel thin-section measurement, a single pixel can be expected to be highly correlated with many other pixels.

The structure tensor a^k_{ij} for measurement k can be written as the sum

$$a^k_{ij} = A_{ij} + g^k_{ij} + h^k_{ij}. \tag{5}$$

Here, g^k_{ij} is a random component accounting for intergrain variance in a^k_{ij}, constant across each grain. Let the site k be in grain M. Then, $g^k_{ij} = a^M_{ij} - A_{ij}$, where the mean a^M_{ij} is the expectation of a^l_{ij} taken over all measurements l in grain M. Likewise, h^k_{ij} is a random component which can be identified with intragrain variability. By rearranging terms, $h^k_{ij} = a^k_{ij} - A_{ij} - g^k_{ij}$. We assume that g^k_{ij} and h^k_{ij} are independent.

Note that we separate out the mean of A_{ij}, which is the mean of a^k_{ij} (for all k) taken over the ODF. Furthermore, we are also separating out the mean of each individual grain as well. This decomposition separates out the components of the structure tensor that vary on different length scales: global (A_{ij}), per grain (g^k_{ij}), and intragrain (h^k_{ij}). This will allow us look at the relative contributions of these components, and their effect on sampling error.

Suppose a^k_{ij} and a^l_{ij} were taken from the same grain. Let G^{kl}_{ij} be the covariance between g^k_{ij} and g^l_{ij}. From Equation (5), $g^k_{ij} = g^l_{ij}$. This also implies that every entry of the covariance tensor of g^k_{ij}, G^{kl}_{ij}, is equal to $\mathrm{Cov}(g^k_{ij}, g^l_{ij}) = \mathrm{Var}(g^k_{ij})$ (no sum), for all k, l taken from the same grain. Due to independence between g_{ij}^k and h_{ij}^k, we can write the covariance as the sum $C_{ij}^{kl} = H_{ij}^{kl} + G_{ij}^{kl}$, where H_{ij}^{kl} is the covariance between h_{ij}^k and h_{ij}^l.

Correlation between adjacent grains is usually small, unless there is active polygonization [26]. Correlation between distant grains is always small, even if two distant grains happen to have similar orientations. Therefore, we are justified in neglecting covariances between points in different grains. This means that we can take $G_{ij}^{kl} = 0$ and $H_{ij}^{kl} = 0$ whenever observations k and l are not from the same grain.

We now show that the intragrain variability, h_{ij}^k, may be ignored under some light assumptions. The covariance H_{ij}^{kl} is non-negligible only where points k and l lie not only within the same grain (otherwise it is zero by assumption), but sufficiently close together. This is because intragraular misorientations, for example due to the formation of subgrain boundaries, occur on lengths smaller than the grain. Because of this, H_{ij}^{kl} is negligible for may more combinations of k and l than G_{ij}^{kl} is. In addition, intragranular c-axis misorientations are usually not more than a few degrees, so the covariance (as opposed to correlation) H_{ij}^{kl} is likely small for even highly correlated nearby pairs of c-axis measurements k, l. Given this, we may approximate the total covariance $C_{ij}^{kl} \approx G_{ij}^{kl}$.

This implies that $C_{ij}^{kl} = C_{ij}^{pq} \approx G_{ij}^{kl} = \mathrm{Var}(g_{ij}^k) \approx \mathrm{Var}(c_i^k c_j^k)$, whenever k, l, p, q lie in the same grain, and zero otherwise. From this, we can write the variance of the *sum* of all a_{ij}^k taken from a grain m as $n^m \mathrm{Var}(c_i^m c_i^m)$, where n^m is the number of observations from the grain with index m. Finally, due to independence between different grains, $\mathrm{Var}(c_i^m c_j^m) = \mathrm{Var}(c_i c_j)$ is the same for all grains, since by these assumptions they are drawn independently from the same ODF.

Now we have an expression for the variance of individual grains in terms of $\mathrm{Var}(c_i c_j)$. Then, we can write $\mathrm{Var}(\tilde{A}_{ij})$ as a sum of the variances of individual grains, in turn. This is given by,

$$\mathrm{Var}(\tilde{A}_{ij}) \approx \sum_m (w^m)^2 \mathrm{Var}(c_i c_j) = s_n^2 \mathrm{Var}(c_i c_j) \qquad (6)$$

where $w^m = n^m/N$ is a weighting coefficient corresponding to the fraction of observations lying in grain m of a total number of observations N. The coefficient s_n^2 is the sum of the squared weights. If we have many observations per grain, Equation (6) substantially simplifies treatment of uncertainty compared to Equation (3). By only considering data on a per-grain basis and ignoring intragrain c-axis variability, we are also able to use the same analysis for thin-section data collected per-grain (as in the Rigsby Stage method), or per-pixel (as with EBSD or automatic fabric analyzers). Note that in the case of c-axis measurements given per-grain, rather than per-pixel, weighting the measurements by grain area is physically preferred to equal weighting [35]. Area weighting also yields similar variance estimates to per-pixel measurements, if the number of per-pixel measurements in each grain is proportional to the area.

We now derive analytical estimates of the distribution of the sample estimate $\tilde{A}_{ij}$, using Equation (6). For a large-enough sample, $\tilde{A}_{ij}$ will have principal directions and eigenvalues close to those of A_{ij}. For a large enough number of grains, we can apply the central limit theorem to estimate the sampling distribution of A_{ij}. As the number of sampled grains n becomes large, $\tilde{A}_{ij}$ converges in distribution to the normal distribution with mean A_{ij} and variance $\mathrm{Var}(c_i c_j) s_n^2$.

Variance is the mean of the square minus the square of the mean. From this, $\mathrm{Var}(c_i c_j) =< c_i c_j c_i c_j > - < c_i c_j >^2 = A_{ijij} - A_{ij} A_{ij}$. Then, the variance of the sample estimate of $\tilde{A}_{ij}$ is given by,

$$\mathrm{Var}(\tilde{A}_{ij}) \approx (\mathbb{A}_{ijij} - A_{ij} A_{ij})\, s_n^2 \tag{7}$$

$$\approx \left(\tilde{\mathbb{A}}_{ijij} - \tilde{A}_{ij} \tilde{A}_{ij}\right) s_n^2 \tag{8}$$

with no sum in i or j. The preceding gives us an expression for variance of the sample estimate $\tilde{A}_{ij}$ of A_{ij}. Note that s_n^2 is at a minimum when all area weights are equal, corresponding to equal grain weighting. In that case, the sum of squared weights is $s_n^2 = n^{-1}$. This is the minimum s_n^2 for any choice of positive weightings that sum to unity. Therefore, equal weighting of grains always underestimates sampling error.

For simplicity, we choose to work in the reference frame defined by the three true fabric eigenvectors. In this case, A_{ij} is a diagonal matrix of the fabric eigenvalues λ_i, and the components of c_i are uncorrelated. For a large enough number of grains, $\tilde{A}_{ij} = A_{ij} + \epsilon_{ij}$, where ϵ_{ij} is small. We can then estimate the sampled fabric eigenvalues and eigenvectors as a first-order perturbation of the original eigenvalues and eigenvectors. In this case, let A_{ij} have eigenvalues $\lambda_i = A_{ii}$ (no sum). Also, let the fabric sample have eigenvalues $\tilde{\lambda}_i = \lambda_i + \delta\lambda_i$. Then, to first order, $\delta\lambda_i = \epsilon_{ii}$ (no sum) [78].

It follows that the variance of sample eigenvalues $\tilde{\lambda}_i$ is then given by $\mathrm{Var}(\tilde{A}_{ii})$ (no sum), since $\tilde{A}_{ii} = \tilde{\lambda}_i$ (no sum). This is most easily found by calculating $\mathrm{Var}(c_i^2)$, where c_i is expressed in the reference frame defined by the principal directions, and has zero empirical mean. In the case of analytical orientation distribution functions, the second- and fourth-order orientation tensors, which correspond to the second and fourth moments of the distribution, can be used directly. From this, it can be seen that samples from more diffuse orientation distribution functions will have larger variance of sample eigenvalues, and concentrated fabrics will have less variance.

Now that we have an estimate for the sample variance of eigenvalue estimates from thin sections, we examine sampling error of the fabric eigenvectors, or principal directions. Similarly to the eigenvalues, we use a first-order approximation of the eigenvalue perturbations [78]. If we are in the reference frame defined by the true fabric eigenvectors, then the sample estimate $\tilde{\mathbf{A}}$ will be be close to being diagonal, with small off-diagonal elements. The eigenvalues $\tilde{\mathbf{V}}$ of the $\tilde{\mathbf{A}}$ are then,

$$\tilde{\mathbf{V}} = \begin{pmatrix} 1 & \frac{\tilde{A}_{12}}{\lambda_2-\lambda_1} & \frac{\tilde{A}_{13}}{\lambda_3-\lambda_1} \\ \frac{\tilde{A}_{21}}{\lambda_1-\lambda_2} & 1 & \frac{\tilde{A}_{23}}{\lambda_3-\lambda_2} \\ \frac{\tilde{A}_{31}}{\lambda_1-\lambda_3} & \frac{\tilde{A}_{12}}{\lambda_2-\lambda_3} & 1 \end{pmatrix}, \tag{9}$$

to first-order accuracy in $\tilde{A}_{ij}$. The perturbed eigenvalue matrix $\tilde{\mathbf{V}}$ is then also an infinitesimal rotation matrix, which is a first-order approximation for rotation matrices valid for small rotation angles. This defines the approximate reference frame formed by the perturbed eigenvectors. The three elements above the diagonal are the Euler angles of this infinitesimal rotation, with $\alpha = \tilde{V}_{23}$, $\beta = \tilde{V}_{13}$, and $\gamma = \tilde{V}_{12}$ being the rotation angles around the z-axis, y-axis, and x-axis, respectively. As before, the sample-based estimate $\tilde{A}_{ij}$ of the component of the second-order orientation tensor A_{ij} is approximately normally distributed for a large enough sample of grains, with variance $(A_{ijij} - A_{ij}A_{ij})s_n^2$ (no sum). Thus, α is approximately normally distributed with variance $(\lambda_2 - \lambda_1)^{-2}\mathrm{Var}(\tilde{A}_{12})$, and a mean of zero. The cases for β and γ are similar.

From this, variance of the Euler angle about an axis is inversely proportional to the difference in the fabric eigenvalues associated with the other two axes. This means that the variance becomes large if the other two eigenvalues are very close together. It is not defined if the eigenvalues are identical. This is because if there are two identical eigenvalues, then there are two corresponding orthogonal eigenvectors, and any vector in the plane formed by those eigenvectors is an eigenvector. Therefore, there is not a unique reference frame which makes **A** diagonal in this case.

Grain-size distribution also has an important influence on sampling error of eigenvalue and eigenvector estimates. Uneven distributions, in which a small number of large grains account for most of the volume, induce greater sampling uncertainty than a grain-size distribution of more evenly-sized grains. As an extreme example, if a fabric thin section contains one large grain, and a thousand infinitesimally small grains, the sample size is effectively one grain, because the small grains have weightings close to zero. The variance of $\tilde{A}_{ij}$ is proportional to the sum of squared weights, s_n^2. This attains a minimum value for equal weights. Grain-size distributions found in ice cores often have a few large grains and many small grains. Equal weighting can therefore lead to a significant underestimate of sampling error.

BIBLIOGRAPHY

[1] M. Abadi, A. Agarwal, P. Barham, E. Brevdo, Z. Chen, C. Citro, G.S. Corrado, A. Davis, J. Dean, M. Devin, et al. Tensorflow: Large-scale machine learning on heterogeneous distributed systems. *arXiv preprint arXiv:1603.04467*, 2016.

[2] S.G. Advani and C.L. Tucker. The use of tensors to describe and predict fiber orientation in short fiber composites. *Journal of Rheology (1978-present)*, 31(8):751–784, 1987.

[3] S.G. Advani and C.L Tucker. Closure approximations for three-dimensional structure tensors. *Journal of Rheology*, 34(3):367–386, 1990.

[4] K. Aki and P.G. Richards. *Quantitative Seismology: Theory and Methods*. WH Freeman and Company, San Francisco, 1980.

[5] R.B. Alley. Fabrics in polar ice sheets: development and prediction. *Science*, 240(4851): 493, 1988.

[6] R.B. Alley. Flow-law hypotheses for ice-sheet modeling. *J. Glaciol*, 38(129):245–256, 1992.

[7] R.B. Alley, A.J. Gow, D.A. Meese, J.J. Fitzpatrick, E.D. Waddington, and J.F. Bolzan. Grain-scale processes, folding, and stratigraphic disturbance in the GISP2 ice core. *Journal of Geophysical Research*, 102(C12):26819–26, 1997.

[8] N. Azuma. A flow law for anisotropic ice and its application to ice sheets. *Earth and Planetary Science Letters*, 128(3-4):601–614, 1994.

[9] N Azuma. A flow law for anisotropic polycrystalline ice under uniaxial compressive deformation. *Cold regions science and technology*, 23(2):137–147, 1995.

[10] N. Azuma and K. Goto-Azuma. An anisotropic flow law for ice-sheet ice and its implications. *Annals of Glaciology*, 23:202–208, 1996.

[11] R.E. Bell, K. Tinto, I. Das, M. Wolovick, W. Chu, T.T. Creyts, N. Frearson, A. Abdi, and J.D. Paden. Deformation, warming and softening of greenland's ice by refreezing meltwater. *Nature Geoscience*, 7(7):497–502, 2014.

[12] C.R. Bentley. Seismic-wave velocities in anisotropic ice: A comparison of measured and calculated values in and around the deep drill hole at Byrd Station, Antarctica. *Journal of Geophysical Research*, 77(23):4406–4420, 1972.

[13] C. Bingham. An antipodally symmetric distribution on the sphere. *The Annals of Statistics*, pages 1201–1225, 1974.

[14] G. Bouchard. Efficient bounds for the softmax function and applications to approximate inference in hybrid models. In *NIPS 2007 workshop for approximate Bayesian inference in continuous/hybrid systems*, 2007.

[15] O. Castelnau, G.R. Canova, R.A. Lebensohn, and P. Duval. Modelling viscoplastic behavior of anisotropic polycrystalline ice with a self-consistent approach. *Acta materialia*, 45(11):4823–4834, 1997.

[16] D.H. Chung and T.H. Kwon. Invariant-based optimal fitting closure approximation for the numerical prediction of flow-induced fiber orientation. *Journal of rheology*, 46(1): 169–194, 2002.

[17] N. Cressie. Statistics for spatial data: Wiley series in probability and statistics. *Wiley-Interscience New York*, 15:16, 1993.

[18] K.M. Cuffey, Th. Thorsteinsson, and E.D. Waddington. A renewed argument for crystal size control of ice sheet strain rates. *Journal of Geophysical Research: Solid Earth*, 105 (B12):27889–27894, 2000.

[19] A. Diez and O. Eisen. Seismic wave propagation in anisotropic ice-part 1: Elasticity tensor and derived quantities from ice-core properties. *The Cryosphere*, 9(1):367–384, 2015.

[20] S. Dinh and R. Armstrong. A rheological equation of state for semiconcentrated fiber suspensions. *Journal of Rheology (1978-present)*, 28(3):207–227, 1984.

[21] C.L. DiPrinzio, L.A. Wilen, R.B. Alley, J.J. Fitzpatrick, M.K. Spencer, and A.J. Gow. Fabric and texture at Siple Dome, Antarctica. *Journal of Glaciology*, 51(173):281–290, 2005.

[22] R. Drews, O. Eisen, I. Weikusat, S. Kipfstuhl, A. Lambrecht, D. Steinhage, F. Wilhelms, and H. Miller. Layer disturbances and the radio-echo free zone in ice sheets. *The Cryosphere*, 3(2):195–203, 2009.

[23] J. Duchi and Y. Hazan, E.and Singer. Adaptive subgradient methods for online learning and stochastic optimization. *Journal of Machine Learning Research*, 12(Jul):2121–2159, 2011.

[24] G. Durand, O. Gagliardini, T. Thorsteinsson, A. Svensson, S. Kipfstuhl, and D. Dahl-Jensen. Ice microstructure and fabric: an up-to-date approach for measuring textures. *Journal of Glaciology*, 52(179):619–630, 2006.

[25] G. Durand, F. Gillet-Chaulet, A. Svensson, O. Gagliardini, S. Kipfstuhl, J. Meyssonnier, F. Parrenin, P. Duval, D. Dahl-Jensen, et al. Change in ice rheology during climate variations–implications for ice flow modelling and dating of the EPICA Dome C core. *Climate of the Past*, 3(1):155–167, 2007.

[26] G. Durand, A. Persson, D. Samyn, and A. Svensson. Relation between neighbouring grains in the upper part of the northgrip ice core - implications for rotation recrystallization. *Earth and planetary science letters*, 265(3):666–671, 2008.

[27] G. Durand, A. Svensson, A. Persson, O. Gagliardini, F. Gillet-Chaulet, J. Sjolte, M. Montagnat, and D. Dahl-Jensen. Evolution of the texture along the EPICA Dome C ice core. *Low Temperature Science*, 68(Supplement):91–105, 2009.

[28] P. Duval, MF Ashby, and I. Anderman. Rate-controlling processes in the creep of polycrystalline ice. *The Journal of Physical Chemistry*, 87(21):4066–4074, 1983.

[29] B. Efron. *Bootstrap methods: another look at the jackknife*. Springer, 1992.

[30] J. Fitzpatrick, D. Voigt, J. Fegyveresi, N. Stevens, M. Spencer, J. Cole-Dai, R. Alley, G. Jardine, E. Cravens, L. Wilen, et al. Physical properties of the WAIS Divide ice core. *Journal of Glaciology*, 60(224):1181, 2014.

[31] A. Fuchs and M.C. Leuenberger. δ18o of atmospheric oxygen measured on the grip ice core document stratigraphic disturbances in the lowest 10% of the core. *Geophysical Research Letters*, 23(9):1049–1052, 1996.

[32] T.J. Fudge, K.C. Taylor, E.D. Waddington, J.J. Fitzpatrick, and H. Conway. Electrical stratigraphy of the WAIS Divide ice core: Identification of centimeter-scale irregular layering. *Journal of Geophysical Research: Earth Surface*, 121(7):1218–1229, 2016.

[33] O. Gagliardini and J. Meyssonnier. Plane flow of an ice sheet exhibiting strain-induced anisotropy. In *Advances in cold-region thermal engineering and sciences*, pages 171–182. Springer, 1999.

[34] O. Gagliardini, G. Durand, and Y. Wang. Grain area as a statistical weight for polycrystal constituents. *Journal of Glaciology*, 50(168):87–95, 2004.

[35] O. Gagliardini, G. Durand, and Y. Wang. Grain area as a statistical weight for polycrystal constituents. *Journal of Glaciology*, 50(168):87–95, 2004.

[36] O. Gagliardini, F. Gillet-Chaulet, and M. Montagnat. A review of anisotropic polar ice models: from crystal to ice-sheet flow models. *Low Temperature Science*, 68 (Supplement):149–166, 2009.

[37] F. Gillet-Chaulet, O. Gagliardini, J. Meyssonnier, M. Montagnat, and O. Castelnau. A user-friendly anisotropic flow law for ice-sheet modelling. *Journal of glaciology*, 51(172): 3–14, 2005.

[38] F. Gillet-Chaulet, O. Gagliardini, J. Meyssonnier, T. Zwinger, and J. Ruokolainen. Flow-induced anisotropy in polar ice and related ice-sheet flow modelling. *Journal of Non-Newtonian Fluid Mechanics*, 134(1):33–43, 2006.

[39] John W Glen. The creep of polycrystalline ice. In *Proceedings of the Royal Society of London A: Mathematical, Physical and Engineering Sciences*, volume 228, pages 519–538. The Royal Society, 1955.

[40] G. Gödert. A mesoscopic approach for modelling texture evolution of polar ice including recrystallization phenomena. *Annals of Glaciology*, 37(1):23–28, 2003.

[41] G. Gödert and K. Hutter. Induced anisotropy in large ice shields: theory and its homogenization. *Continuum Mechanics and Thermodynamics*, 10(5):293–318, 1998.

[42] A. Gusmeroli, E.C. Pettit, J.H. Kennedy, and C. Ritz. The crystal fabric of ice from full-waveform borehole sonic logging. *Journal of Geophysical Research: Earth Surface*, 117(F3), 2012.

[43] P. Hall, J. Horowitz, and B. Jing. On blocking rules for the bootstrap with dependent data. *Biometrika*, 82(3):561–574, 1995.

[44] M.B. Helgerud, W.F. Waite, S.H. Kirby, and A. Nur. Elastic wave speeds and moduli in polycrystalline ice ih, si methane hydrate, and sii methane-ethane hydrate. *Journal of Geophysical Research: Solid Earth*, 114(B2), 2009.

[45] R. Hill. The elastic behaviour of a crystalline aggregate. *Proceedings of the Physical Society. Section A*, 65(5):349, 1952.

[46] D. Iliescu, I. Baker, and H. Chang. Determining the orientations of ice crystals using electron backscatter patterns. *Microscopy research and technique*, 63(4):183–187, 2004.

[47] D. Jansen, M. Llorens, J. Westhoff, F. Steinbach, S. Kipfstuhl, P.D. Bons, A. Griera, and I. Weikusat. Small-scale disturbances in the stratigraphy of the NEEM ice core: observations and numerical model simulations. *The Cryosphere*, 10:359–370, 2016.

[48] G.B. Jeffery. The motion of ellipsoidal particles immersed in a viscous fluid. *Proceedings of the Royal Society of London. Series A, Containing papers of a mathematical and physical character*, pages 161–179, 1922.

[49] J. Kennedy, E. Pettit, and C. Di Prinzio. The evolution of crystal fabric in ice sheets and its link to climate history. *Journal of Glaciology*, 59(214):357–373, 2013.

[50] D. Kluskiewicz, E.D. Waddington, S. Anandakrishnan, D.E. Voigt, K. Matsuoka, and M.P. McCarthy. Sonic methods for measuring crystal orientation fabric in ice, and results from the west antarctica ice sheet divide. 2017.

[51] C. Langway. *Ice fabrics and the universal stage*. Department of Defense, Department of the Army, Corps of Engineers, Snow Ice and Permafrost Research Establishment, 1959.

[52] R.A. Lebensohn and C.N. Tomé. A self-consistent anisotropic approach for the simulation of plastic deformation and texture development of polycrystals: application to zirconium alloys. *Acta Metallurgica et Materialia*, 41(9):2611–2624, 1993.

[53] R.C. Lile. The effect of anisotropy on the creep of polycrystalline ice. *Journal of Glaciology*, 21(85):475–483, 1978.

[54] L. Lliboutry. Anisotropic, transversely isotropic nonlinear viscosity of rock ice and

rheological parameters inferred from homogenization. *International journal of plasticity*, 9(5):619–632, 1993.

[55] K. Mardia. Characterizations of directional distributions. In *A Modern Course on Statistical Distributions in Scientific Work*, pages 365–385. Springer, 1975.

[56] A. Maurel, F. Lund, and M. Montagnat. Propagation of elastic waves through textured polycrystals: application to ice. In *Proc. R. Soc. A*, volume 471, page 20140988. The Royal Society, 2015.

[57] A. Maurel, J. Mercier, and M. Montagnat. Critical investigation of calculation methods for the elastic velocities in anisotropic ice polycrystals. *The Cryosphere*, 10(6):3063–3070, 2016.

[58] J. Meyssonnier and A. Philip. A model for the tangent viscous behaviour of anisotropic polar ice. *Annals of Glaciology*, 23:253–261, 1996.

[59] M. Montagnat and P. Duval. Rate controlling processes in the creep of polar ice, influence of grain boundary migration associated with recrystallization. *Earth and Planetary Science Letters*, 183(1):179–186, 2000.

[60] M. Montagnat, N. Azuma, D. Dahl-Jensen, J. Eichler, S. Fujita, F. Gillet-Chaulet, S. Kipfstuhl, D. Samyn, A. Svensson, and I. Weikusat. Fabric along the NEEM ice core, Greenland, and its comparison with GRIP and NGRIP ice cores. 2014.

[61] M. Montagnat, N. Azuma, D. Dahl-Jensen, J. Eichler, S. Fujita, F. Gillet-Chaulet, S. Kipfstuhl, D. Samyn, A. Svensson, and I. Weikusat. Fabric along the NEEM ice core, Greenland, and its comparison with GRIP and NGRIP ice cores. 2014.

[62] S. Montgomery-Smith. Perturbations of the coupled Jeffery-Stokes equations. *Journal of Fluid Mechanics*, 681:622–638, 2011.

[63] S. Montgomery-Smith, W. He, D.A. Jack, and D.E. Smith. Exact tensor closures for the three-dimensional Jeffery's equation. *Journal of Fluid Mechanics*, 680:321–335, 2011.

[64] T. C. Onstott. Application of the Bingham distribution function in paleomagnetic studies. *Journal of Geophysical Research: Solid Earth*, 85(B3):1500–1510, 1980.

[65] V.F. Petrenko and R.W. Whitworth. *Physics of ice.* OUP Oxford, 1999.

[66] A. Philip and J. Meyssonnier. Anisotropic isothermal ice-cap flow with the shallow ice approximation. In *Advances in Cold-Region Thermal Engineering and Sciences*, pages 237–248. Springer, 1999.

[67] L. Placidi, R. Greve, H. Seddik, and S.H. Faria. Continuum-mechanical, anisotropic flow model for polar ice masses, based on an anisotropic flow enhancement factor. *Continuum Mechanics and Thermodynamics*, 22(3):221–237, 2010.

[68] C.E. Rasmussen. Gaussian processes for machine learning. 2006.

[69] G. Sachs. Zur ableitung einer fliebedingung. *Z. Vereins Dtsch. Ing.*, 12(8):734–736, 1928.

[70] I.H. Sloan and R.S. Womersley. Extremal systems of points and numerical integration on the sphere. *Advances in Computational Mathematics*, 21(1-2):107–125, 2004.

[71] E.C. Smith, A.F. Baird, J.M. Kendall, C. Martín, R.S. White, A.M. Brisbourne, and A.M. Smith. Ice fabric in an antarctic ice stream interpreted from seismic anisotropy. *Geophysical Research Letters*, 2017.

[72] R. Staroszczyk and O. Gagliardini. Two orthotropic models for strain-induced anisotropy of polar ice. *Journal of Glaciology*, 45(151):485–494, 1999.

[73] B. Svendsem and K. Hutter. A continuum approach for modelling induced anisotropy in glaciers and ice sheets. *Annals of Glaciology*, 23(1):262–269, 1996.

[74] G.I. Taylor. Analysis of plastic strain in a cubic crystal. *Stephen Timoshenko 60th Anniversary Volume*, pages 218–224, 1938.

[75] T. Thorsteinsson. Fabric development with nearest-neighbor interaction and dynamic recrystallization. *J. Geophys. Res*, 107(2014):10–1019, 2002.

[76] T. Thorsteinsson and E.D. Waddington. Folding in strongly anisotropic layers near ice-sheet centers. *Annals of Glaciology*, 35(1):480–486, 2002.

[77] Throstur Thorsteinsson. *Anisotropy of ice Ih: Development of fabric and effects of anisotropy on deformation.* PhD thesis, University of Washington, 2000.

[78] L. N. Trefethen and D. Bau III. *Numerical linear algebra*, volume 50. Siam, 1997.

[79] C. Vogt, K. Laihem, and C. Wiebusch. Speed of sound in bubble-free ice. *The Journal of the Acoustical Society of America*, 124(6):3613–3618, 2008.

[80] R. Von Mises. Mechanics of plastic deformation of crystals. *Applied Mathematics and Mechanics*, 592:8, 1928.

[81] J. Weertman. Creep deformation of ice. *Annual Review of Earth and Planetary Sciences*, 11(1):215–240, 1983.

[82] L Wilen. Ice Fabric Characteristics: Siple Dome, A Core. Boulder, CO: National Snow and Ice Data Center, 2002. URL `https://nsidc.org/data/nsidc-0255`.

[83] L. A. Wilen, C. L. Diprinzio, R. B. Alley, and N. Azuma. Development, principles, and applications of automated ice fabric analyzers. *Microscopy research and technique*, 62 (1):2–18, 2003.

[84] Q. Zheng and W. Zou. Orientation distribution functions for microstructures of heterogeneous materials (i) directional distribution functions and irreducible tensors. *Applied Mathematics and Mechanics*, 22(8):865–884, 2001.